Small-Body and Heliophysics Missions using Hybrid Low-Thrust Propulsion

by

Daniel Miller

B.S., University at Buffalo (2017)
S.M., Massachusetts Institute of Technology (2020)

Submitted to the Department of Aeronautics and Astronautics
in partial fulfillment of the requirements for the degree of

DOCTOR OF PHILOSOPHY IN AERONAUTICS AND ASTRONAUTICS

at the

MASSACHUSETTS INSTITUTE OF TECHNOLOGY

June 2024

Authored by: Daniel Miller
Department of Aeronautics and Astronautics
May 17, 2024

Certified by: Richard Linares
Rockwell International Career Development Professor, Thesis Supervisor

Paulo Lozano
Miguel Alemán Velasco Prof. of Aero. and Astro., Committee Member

Jacob A. Englander
Mission Design Engineer, Applied Physics Lab., Committee Member

Olivier L. de Weck
Apollo Program Prof. of Astro. and Eng. Systems, Committee Member

Accepted by: Jonathan P. How
Richard Cockburn Maclaurin Professor in Aeronautics and Astronautics
Chair, Graduate Committee

Small-Body and Heliophysics Missions using Hybrid Low-Thrust Propulsion

by

Daniel Miller

Submitted to the Department of Aeronautics and Astronautics
on May 17, 2024 in partial fulfillment of the requirements for the degree of

DOCTOR OF PHILOSOPHY IN AERONAUTICS AND ASTRONAUTICS

ABSTRACT

Throughout the history of spaceflight, new missions and capabilities have been enabled by the development of increasingly efficient and powerful propulsion systems. However, all of these systems, from the earliest chemical engines to modern electric thrusters, require propellant, thereby reducing the mass budget available for a payload. By harnessing the momentum of reflected photons of sunlight, solar sails offer a propellant-free alternative but are limited by attitude restrictions and their low thrust. Their improvement has also been inhibited by current knowledge of both materials science and structural engineering. In this dissertation, an assessment of a hybrid propulsion system is presented that maximizes the positive traits of its two constituent subsystems. By augmenting solar electric propulsion (SEP) with a solar sail, a spacecraft may be created with lower propellant consumption than SEP alone and greater thrust than a pure sailcraft, while not necessitating the technical development of the most ambitious proposed solar sails.

To conduct this study, trajectories are generated to potential heliophysics and small-body targets: high-inclination, heliocentric orbits and interstellar objects (ISOs). For the former, detailed mass budgets are created and a trade study of subsystem size versus mass is conducted to identify the performance necessary to produce a net positive change in launch mass. For the latter, six spacecraft propulsion systems and four launch vehicles are considered in a broad study of mission viability using two separate databases of synthetic target ISOs. The ability of the hybrid low-thrust propulsion configuration to produce lower mean arrival velocities than more conventional alternatives is then determined. In both cases, nonidealized power and propulsion models are used to improve upon the preexisting literature and make a more accurate assessment of the technology.

Thesis supervisor: Richard Linares
Title: Rockwell International Career Development Professor

Acknowledgments

This dissertation would not have been possible without the assistance of numerous individuals. I would like to start by thanking all of those who have assisted me in navigating the stormy seas of research. First and foremost, this work would not have been possible without my research advisor, Prof. Richard Linares, who provided me with seven years and two graduate degrees worth of guidance and support. Next, I must thank Dr. Jacob Englander, who read a proposal written by a first semester graduate student and dared him to beat the entire field of trajectory design. More importantly, when that student was unable to do so, he taught him the tricks of the trajectory design trade that enabled him to steer his work onto a more promising tack. I would like to thank my remaining committee members, Prof. Paulo Lozano, for his insights into spacecraft propulsion, and Prof. Oli de Weck, who volunteered his time in the final days of my graduate school career to help ensure that I would sail smoothly across the finish line. I must also thank my readers, collaborators, and coauthors, all of whom helped me crew this voyage of discovery: Mr. Zach Folcik, Dr. Toni Engelhardt, Mr. Devin Hoover, and Dr. Nicholas LaFarge. A special thank you to Dr. Damon Landau, for sharing his knowledge of mission design, and to Dr. Paul Gilmore, for pushing me off from the dock at the start of this voyage.

They say that graduate school is a marathon and not a sprint, and I could not have hoped for better running partners. First, an enormous thank you to my labmates and friends across the department for their camaraderie over the rolling hills of this race course. Next, I would like to give my appreciation to my friends at MIT Graduate Hillel and the MIT Conservative Minyan for providing me with an on-campus community away from my work. To the members of my weekly social Zoom of old college friends, thank you for encouraging me to pick up the pace. To the staff of the MIT Sailing Pavilion, thank you for introducing me to a wonderful new hobby. Finally, I must also thank my actual running partners – the members and coaching staff of Community Running – as well as those who have kept me on my feet: my orthopedist and physical therapists.

To my parents, thank you for nearly three decades of love and encouragement. You are my true advisors.

This work was supported by a NASA Space Technology Research Fellowship and a JPL Strategic University Research Partnership. I would also like to acknowledge the MIT SuperCloud and Lincoln Laboratory Supercomputing Center for providing HPC and consultation resources that have contributed to the research results reported within this dissertation.

Biographical Sketch

Since writing one's own biographical sketch feels self-serving, I leave this in the trustworthy hands of a good friend: Daniel Miller is a pretty awesome guy who did some pretty awesome stuff. He did a few different research projects and one of them turned out to be excellent. In his spare time he enjoys running and exercising his dry but tasteful sense of humor. His dream in life is to make outstanding technical contributions and have a window in his office. At some point he would like to compete for the Best Astrodynamics Beard award.

Contents

List of Figures

List of Tables

Chapter 1

Introduction

In 1962, the Venus-bound Mariner 2 corrected its initial trajectory by $45\,\mathrm{mi\,h^{-1}}$ with a 28 s burn, lowering its closest approach to 21 598 mi and becoming the first successful interplanetary mission in the process [15]. The history of interplanetary exploration has ever since been marked by the development of more capable and efficient means of changing the orbital energy of spacecraft, most frequently measured in terms of change in velocity, or ΔV. The earliest missions, such as Mariner 2, were direct flybys using spacecraft with, at most, a limited capability for conducting deep space maneuvers (DSMs). In 1971, following a $1600.5\,\mathrm{m\,s^{-1}}$ retrograde burn, Mariner 9 would become the first spacecraft to orbit another planet, marking an order of magnitude increase in propulsive capability in nine years [15, 16]. As it came to a close in 1973, the Mariner program's final mission would set two more firsts. While passing Venus, Mariner 10 completed a gravity assist, thereby altering its trajectory in order to conduct a subsequent flyby of Mercury. These maneuvers would become commonplace in the future, most notably with the "grand tour" of Jupiter, Saturn, Uranus, and Neptune conducted by the Voyager spacecraft during the 1980s [15]. It would also be the first to take advantage of solar radiation pressure (SRP). Following unexpectedly high demands on its attitude control system, the high-gain antenna and solar panels were positioned in such a manner to produce torques using SRP that minimized further consumption of the limited remaining propellant [17].

The development of low-thrust electric propulsion (EP) has been one of the most consequential developments in spacecraft propulsion since these early days of spaceflight. First tested in the early 1960s and now in widespread use onboard Earth-orbiting satellites, highly-efficient EP has significantly increased the ΔV available to mission planners, and at substantially less cost in terms of vehicle mass. As a result, beginning with Deep Space 1 in 1998, eight deep space missions have been flown using electric propulsion as of 2019, six of which used ion engines. Hall effect thrusters, already commonplace in low-earth orbit, made their debut beyond cis-lunar space as part of the ongoing Psyche mission [18, 19].

While electric propulsion requires far less propellant mass than the equivalent ΔV provided by chemical propulsion (CP), any propellant mass reduces the payload allowance for scientific equipment. This is of particular concern for small CubeSat missions due to their tight mass and volume constraints [20]. Gravity assists offer an alternative, passive means of providing ΔV, but come with limitations in terms of orbital phasing and by their nature can only modify a trajectory at the location of a planet. An active, propellantless propulsion sys-

Table 1.1: History of Proposed and Flown Solar Sails

Year	Mission	Sail Size (m^2)	Vehicle Mass (kg)	Outcome	Ref.
2005	Cosmos 1	600	100	Launch Failure	[30]
2008	NanoSail-D	10	4	Launch Failure	[31]
2010	IKAROS	200	307	Successful	[32, 22]
2010	NanoSail-D2	10	4	Successful	[31]
2015	Sunjammer	1200	45	Canceled	[33, 34]
2015	LightSail 1	32	5	Successful	[30]
2019	LightSail 2	32	5	Successful	[26, 35]
2022	NEA Scout	85	14	Unknown Failure	[36]
2025	Solar Cruiser	1653	100	Canceled	[28]

tem is therefore naturally of great interest. This seeming impossibility can be made a reality using a solar sail. Due to the conservation of momentum of reflected photons, these highly reflective surfaces are able to generate acceleration using nothing but sunlight. The idea actually predates practical spaceflight. According to McInnes, the first writings on achievable solar sailing date back to the early 1920s with the Soviet engineers Konstantin Tsiolkovsky and Fridrickh Tsander [21]. While the Mariner 10 mission provided an unexpected, practical demonstration of the underlying principles of solar sailing, no attempt would be made to use a solar sail as a primary means of propulsion until the 21st century.

Beginning with The Planetary Society's failed attempt in 2005, nine solar sail missions have been proposed or flown. These are summarized in Table 1.1. While early attempts were victims of launch failures, JAXA's IKAROS mission made the first successful demonstration of a solar sail as a primary, interplanetary propulsion system in 2010 [22]. Other key milestones have included NASA's first sail deployment with NanoSail-D2 and the first operations in low Earth orbit by The Planetary Society's LightSail 2 [23]. The Near-Earth Asteroid (NEA) Scout launched as a secondary payload on the first Artemis launch in November 2022, following a multi-year wait due to launch vehicle delays [24, 25]. The most ambitious solar sailing mission yet attempted, this spacecraft was to demonstrate a low-cost exploration capability in the inner Solar System [26]. Unfortunately, the spacecraft failed to make contact after deployment due to an unknown fault [27]. Building upon the experience of designing and constructing this spacecraft, the Solar Cruiser heliophysics mission was then expected to validate an order of magnitude increase in sail size in the mid-2020s [28]. Unfortunately, the mission was canceled due to technical problems and insufficient time to correct these issues [29].

Solar sails must, however, contend with significant limits on their performance. The maximum acceleration generated by a solar sail is far less than that of electric propulsion; it is a function of both distance from the Sun and the desired thrust direction. As a result, solar sail transfer times are generally longer than those of EP or CP and are primarily suited to missions in the inner solar system [37]. The overall performance of a solar sail is also sensitive to vehicle weight, with substantial increases in performance necessitating the development of materials with significantly less mass per unit of area, otherwise known as areal mass. In spite of the flurry of missions over the last two decades, it has proven difficult to advance

the technology readiness level of solar sails [38].

The combination of a solar sail and solar-powered electric propulsion has been proposed as a means of combining the best attributes of the two systems. Cited by Mengali and Quarta [39] as originating in a report by Leipold and Götz [40] in 2002, hybrid low-thrust propulsion (HLTP) augments a solar electric propulsion (SEP) system with a solar sail in order to reduce a spacecraft's propellant mass fraction. This creates a multi-objective trade space between greater SEP utilization with shorter flight times and greater solar sail usage with reduced propellant requirements. The addition of SEP to a solar sail partially mitigates concerns regarding the limitations on the thrust magnitude and direction of a solar sail [37], while also using a more proven technology to lower the risk of further advancements in the technology readiness of solar sails [38].

1.1 Literature Review

The literature on interplanetary HLTP is relatively limited, with Menagli and Quarta being responsible for much of the earliest notable work. Looking at Earth-Mars and Earth-Venus circle-to-circle planar transfers, they first considered a spacecraft in which a normal, SEP-propelled spacecraft is supplemented with a sail that produces acceleration radially outward from the Sun, thus reducing the effective standard gravitational parameter of the solar system. They demonstrated that doing so could reduce the propellant mass fraction by 10% and 5% and reduce transfer times by approximately 100 and 40 days for Mars and Venus, respectively [39]. This same problem was then studied a second time with both the SEP and sail thrust vectors free to orient themselves in any direction. Using a nondimensional parameter to smoothly vary the objective function between mass and time optimality, they demonstrated that a desired balance between the two could easily be selected for a mission [41].

Gong, Li, and Jiang considered a similar Earth-Venus transfer and a rendezvous with the asteroid Apophis. They demonstrated that transfer time and fuel consumption are inversely related, with the trajectory becoming that of a pure solar sail without SEP utilization in the mass-optimal case with a sufficiently long transfer time [37]. More recently, Li, Wang, and Zhang also considered an HLTP mission to Apophis, as well as one to 2000SG344. Using a multi-objective optimization method, trajectories were found in which a small increase in propellant consumption significantly reduced flight times [42].

In 2021, Miller, Englander, and Linares studied a flyby mission to comet 45P using a 1000 kg spacecraft with a 1650 m^2 sail and an SEP system capable of producing 0.23 N of thrust at 1 au. With an inclined, eccentric orbit, a low perihelion of 0.53 au, and a high aphelion of 5.52 au, 45P is a challenging target. The authors found that HLTP could deliver more mass than SEP alone, but at a high cost in flight time. It was also shown that the SEP system was primarily employed for orbit raising, while the solar sail was used for inclination changes [43]. This suggests that HLTP may be most advantageous for missions to highly inclined targets.

Planetary observation from non-keplerian orbits enabled using low-thrust propulsion is a common use case discussed in the literature. Baig and McInnes introduced the concept of HLTP for polar observations from artificial equilibrium points (AEP) in the Sun-Earth

system. They demonstrated that hybrid systems required a smaller sail than a pure sailcraft and had reduced power requirements than competing SEP alternatives. HLTP provided a greater payload mass fraction than alternatives with either of the individual propulsion system alone and was able to access regions inaccessible with a solar sail alone [44].

Ceriotti and McInnes conducted extensive research into the concept of pole-sitters: spacecraft that maintain a position exactly over, or in the general vicinity of, a planetary pole using continuous thrust. HLTP was shown to enable longer Earth-observation missions and reduce initial masses compared to exclusively SEP options [45], with the propellant savings outweighing the additional dry mass of the sail for missions longer than seven years [46]. The combination of the two propulsion systems was also shown to improve the resiliency of the spacecraft; the thruster compensated for long-term sail degradation in the on-orbit environment, while the sail partially countered temporary losses of thrust, thus providing a valuable, multi-week window in which to recover from such an event [47]. This concept would be further developed by Ceriotti, Heiligers, and McInnes [48]. More recently, Heiligers, van den Oever, Ceriotti, Mulligan, and McInnes built on their previous work to extend the concept to pole-sitters over Venus and Mars [49].

Heiligers, Ceriotti, McInnes, and Biggs demonstrated the application of HLTP to another non-keplerian orbit for Earth observation: the displaced geostationary orbit (GEO). With the GEO belt increasingly full, the use of continuous thrust allows for new, artificial geostationary orbits to be created in the vicinity of the natural geostationary orbit (e.g., thrust radially outward to displace further out or thrust normal to the plane to displace above). Solar sails alone were found to be unable to consistently provide the necessary thrust to maintain such an orbit, while SEP would have an unreasonably short lifetime due to rapid fuel depletion. Only HLTP was able to maintain a displaced GEO orbit for a period of time comparable to the lifetime of a traditional GEO satellite [50, 51]. Liu, Heiligers, and Ceriotti would later extend this work by defining displaced geostationary orbit slots. By loosening the position constraint to a region, further propellant savings were achieved [52].

For HLTP to justify the additional complexity that it entails, it must provide a net benefit over either of the alternative single propulsion system alternatives. For example, in a mass-limited mission with a SEP-only baseline, the sail must produce a net benefit by reducing the propellant mass by more than its own subsystem mass. In the case of an acceleration-limited mission, the combined acceleration of the SEP thruster and solar sail must be greater than the equivalent of either system alone. Unfortunately, all HLTP designs are subject to the same performance limitations that solar sails are, namely sail and vehicle weight. As a result of the rocket equation and the additional dry mass of an auxiliary solar sail, it is possible for an HLTP spacecraft to have higher propellant consumption than SEP-alone. Similarly, the additional mass of a sail may reduce the overall acceleration of the spacecraft, even if the total thrust has increased.

Due to their sensitivity to mass, solar sail research has often focused on developing ever lighter, thinner materials with desirable reflective, absorptive, and emmisive characteristics [53]. Solar sail spacecraft performance is most commonly measured by its lightness number β, a nondimensional parameter defined as the ratio of acceleration due to SRP to acceleration due to gravity. This may be calculated as

Table 1.2: Performance parameters of proposed and flown sails.

Year	Mission	Sail Loading σ ($\mathrm{g\,m^{-2}}$)	Lightness Num. β (n.d.)	Sail Areal Density σ_{sail} ($\mathrm{g\,m^{-2}}$)
2005	Cosmos 1	166.7	0.0245	
2008	NanoSail-D	400.0	0.0038	
2010	IKAROS	200.0	0.0001	77
2010	NanoSail-D2	400.0	0.0038	135
2015	Sunjammer	37.5	0.0408	
2015	LightSail 1	156.3	0.0098	15
2019	LightSail 2	156.3	0.0098	15
2022	NEA Scout	164.7	0.0093	43
2025	Solar Cruiser	62.5	0.0245	28

$$\beta = \frac{\sigma^*}{\sigma} = \frac{\sigma^*}{m_{\mathrm{sail}}/A_{\mathrm{sail}}} \tag{1.1}$$

where σ is the sail loading, or mass per unit of area, of the spacecraft and σ^* is the loading necessary for the sail's acceleration to match that of the Sun's gravity. This is commonly defined as $\sigma^* = 1.53\,\mathrm{g\,m^{-2}}$ [21]. For the performance of a sail subsystem specifically, the areal density σ_{sail}, or mass per unit of sail area, is used. Confusingly, σ_{sail} is at other times used to refer only to the sail material itself, excluding the supporting structures and deployment mechanisms. Care must therefore be taken based on context. In this dissertation, σ_{sail} will always refer to the entire subsystem, while σ will refer to the entire spacecraft.

All traditional solar sails can be divided into three main components: a reflective sail "cloth," a supporting structure, and the ancillary systems, which includes the deployment mechanism. Current sail cloth is composed of 50 nm to 100 nm thick aluminum applied to a thin polymer base material, with common materials including CP1, Mylar, and Kapton. The current state of the art for a CP1-based sail cloth is an areal density of $3.3\,\mathrm{g\,m^{-2}}$. Importantly, this is different than σ_{sail} and does not account for structure or mechanism mass. While a long-term goal of $1\,\mathrm{g\,m^{-2}}$ has been suggested, such sails remain theoretical and may necessitate a switch to an entirely different design concept that eliminates the aluminum layer [53].

While reflective sail cloth is the most visible part of a sailcraft, it must be supported by a strong and lightweight support structure. These have thus far taken the form of four deployable booms which emanate from a mechanism contained within, or attached to, the spacecraft bus. An illustrative example of NEA Scout has been provided in Fig. 1.1. Four Triangular Rollable and Collapsible (TRAC) booms [54] may be seen to be unrolling from a central spindle in Fig. 1.1a, followed by the deployment of the sail cloth in Fig. 1.1b. To ensure that the performance of a sailcraft is as close to an idealized sail – a perfectly flat, perfectly smooth reflecting surface – these beams must be able to hold the sail cloth taut without ripples while also resisting sagging under load in a zero-g environment. As described in greater detail in Subsection 2.3.4, a reasonable estimate of a current sail design allocates a breakdown of approximately 14%, 24%, and 61% of the subsystem mass for the cloth,

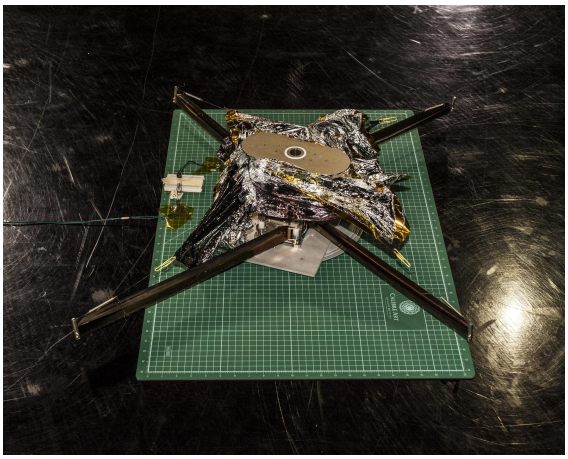

(a) NEA Scout with booms partially deployed [55]

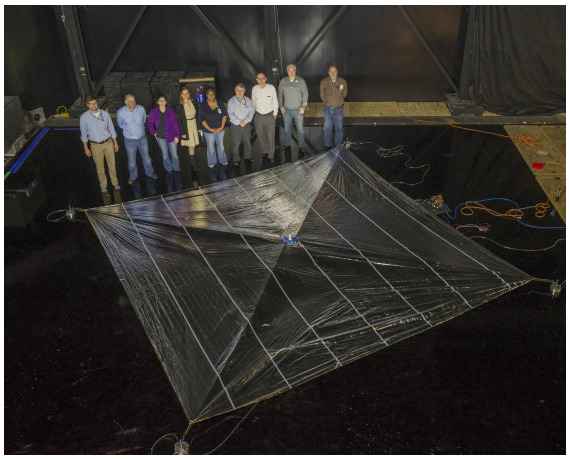

(b) NEA Scout fully deployed [56]

Figure 1.1: The deployment of a NEA Scout development unit that illustrates the supporting structure and final shape of sail

structure, and deployment/ancillary systems mass, respectively.

To provide context of the present performance of flight-ready designs, sail loadings σ and lightness numbers β calculated using the data included in Table 1.1 and sail areal densities available in the literature [57] have been provided in Table 1.2. In 2007, Mengali and Quarta suggested $25\,\mathrm{g\,m^{-2}}$ to $30\,\mathrm{g\,m^{-2}}$ as realistic in the near-term, with mid-term technologies permitting $5\,\mathrm{g\,m^{-2}}$ to $10\,\mathrm{g\,m^{-2}}$. Based on Table 2, such predictions may have been slightly optimistic, though not entirely unreasonable.

In their early work on hybrid low-thrust interplanetary transfers, Mengali and Quarta reported that $\sigma_{\mathrm{sail}} \leq 6\,\mathrm{g\,m^{-2}}$ with $\beta \approx 0.02$ was necessary for HLTP to be superior to pure SEP. In terms of delivered payload mass, improvements of up to 6%-14% were achievable with sail densities between $\sigma_{\mathrm{sail}} \approx 3\,\mathrm{g\,m^{-2}}$ and $\sigma_{\mathrm{sail}} \approx 1\,\mathrm{g\,m^{-2}}$. The relationship of β with delivered mass performance was shown to be complex, with the largest performance increases surprisingly not corresponding to the largest lightness numbers for a given initial mass [41]. Since lightness number increases with sail area, this indicates that the largest possible sail may not be the optimal design choice.

In their study of asteroid missions, Li et al. found HLTP to be superior to pure SEP for an Earth-2000SG344 rendezvous, while inferior to a pure solar sail for a mission to Apophis. This was conducted using spacecraft with an assumed lightness number of $\beta = 0.02$ and $\beta = 0.03$, respectively [42]. Miller et al. defined a spacecraft with a less ambitious $\beta = 0.003$ and found that HLTP could be superior to SEP for a comet rendezvous, but at the cost of significantly longer flight time [43].

In the realm of observation missions, Heiligers et al. assumed $5\,\mathrm{g\,m^{-2}}$ to achieve their positive results [50, 51]. Liu et al. evaluated a mass budget at 7.5, 5, and $2\,\mathrm{g\,m^{-2}}$, which they defined as achievable in the near-term, far-term, and future, respectively. HLTP was inferior to SEP at $7.5\,\mathrm{g\,m^{-2}}$, but successfully produced a net mass advantage at the lower values [52]. These are all significantly lower than the values in Table 1.2. It may therefore be concluded that HLTP will require further developments in solar sail material properties,

with the degree of advancement varying based on the particular mission. A thorough mass budget analysis is therefore advisable in any HLTP study.

1.2 Thesis Objectives and Expected Contributions

HLTP has been shown to be a promising means of reducing the propellant mass fraction of an SEP spacecraft, but one that is mission specific and subject to underlying assumptions regarding the state of solar sail technology. Furthermore, as a small field, the range of HLTP applications studied thus far remains modest. The objective of this thesis is therefore to expand the list of potential mission types while addressing certain shortcomings in the field to be outlined here.

1.2.1 Application 1: Heliophysics Missions

Heliophysics missions have historically been an attractive subject for solar sailing concepts. These include sending spacecraft to the L_4 and L_5 Sun-Earth Lagrange points [58, 59], solar pole sitters [48], and high inclination orbiters [60]. The canceled Solar Cruiser mission, much like the canceled Sunjammer mission before it, would have traveled to the sub-L_1 region to provide advanced warning of solar storms [33, 28]. Despite this rich body of literature, no HLTP paper has yet covered this mission category. Based on the results of Miller et al. that suggested that HLTP may be especially beneficial for large inclination changes [43], polar observation missions would likely be of the most benefit and are worth exploring further.

1.2.2 Application 2: Interstellar Objects

Interstellar objects (ISOs) offer a unique scientific opportunity to answer fundamental scientific questions about the origin of solar system volatiles, the composition of exo-solar systems, and the transfer rates of materials between solar systems. The first of these objects, 1I/'Oumuamua, was discovered in 2017 [61]. A second object, the comet 2I/Borisov, was identified in 2019, and many more are expected to be found with the upcoming introduction of the Vera C. Rubin Observatory (previously the Large Synoptic Survey Telescope) [62, 63]. To reap the maximum scientific benefit that the study of these objects offer, it will be necessary to examine them up close with either a flyby or rendezvous mission. Unfortunately, ISOs are challenging targets. 1I/'Oumuamua was first observed after, and 2I/Borisov only a few months before, reaching their respective perihelia [61, 64]. As a result, spacecraft are likely to reach their targets as they leave the outer solar system. Furthermore, as with any object on a hyperbolic trajectory, ISOs possess high characteristic energies C_3 that will need to be matched to achieve a rendezvous.

Several authors have already considered how missions to these objects could be accomplished, although not with solar sails or HLTP. Styled after NASA's Deep Impact, Seligman and Laughlin considered a mission to 'Oumuamua to conduct a spectroscopic analysis of a debris plume generated by colliding an impactor vehicle with an ISO. Such a mission is possible with near-term technology, for it would not be necessary to match the velocity of the asteroid. It would, however, have required a spacecraft to have been built and ready

for launch upon the early detection of the ISO, and strains the navigation feasibility of fast intercepts [65, 66]. In response to this, Hibberd, Hein, and Eubanks identified trajectories that used a series of gravity assists to reach 'Oumuamua before 2050 from an assumed launch date in the early 2030s, thus allowing for sufficient time to construct the spacecraft [67].

1.2.3 Improvements to Systems Modeling

Reality is immeasurably complex and any attempt to accurately represent all of its intricacies in simulation is folly. In the final stages of mission design, a full flight-fidelity simulation model can be impractical to implement and computationally expensive. However, overly simple models lack the necessary accuracy to draw meaningful conclusions. It is therefore surprising that the investigations found in the literature have largely employed only basic models. Three areas of concern have been identified and shall be addressed: the sail model, the SEP/power model, and the SEP thrust vector direction. These are summarized in Table 1.3.

In an ideal sail model, parallel rays of light from the Sun maintain their parallel nature after undergoing "mirror like" specular reflection. Real solar sails, however, are imperfect. They may wrinkle. They may have a slight concave or convex shape. They may have tears. These result in some degree of imperfect, diffuse reflections which reduce peak performance by up to 8.7% (see Appendix B.1). It will also result in a small, tangential thrust force in addition to the main thrust in the direction anti-normal to the solar sail. In summary, compared to the well-known McInnes non-ideal sail model, an ideal sail will produce more thrust [21] and its use risks overestimating the benefit of adding a solar sail to a more traditional, SEP-only spacecraft.

In the literature, an ideal SEP model has frequently been used with a constant maximum available thrust and a mass flow rate based on Tsiolkovsky's rocket equation [50, 37, 42, 52]. This requires the assumption that the electrical power necessary to drive the thruster at its maximum thrust will always be available. For an Earth-orbiting spacecraft, this may not be a terrible assumption; while eclipses are a concern, the distance to the Sun remains approximately constant over the course of a year. More generally, however, power decreases with the inverse square of the distance to the Sun (see Eq. 2.22) and active propulsion in the outer solar system is often limited. A constant thrust or power assumption is therefore unsuitable for deep-space mission planning and will exaggerate the performance of SEP with respect to solar sails.

Another common assumption in the HLTP literature has been that the solar sail and SEP thrust vectors can operate entirely independently of each other. Solar sails, being constructed of an aluminized thin film designed to reflect light on one side and emit heat on the other, are always constrained to keep the reflective side facing the Sun. This is true in all sail models in the literature. In contrast, the SEP thrust vector has commonly been left unconstrained [50, 37, 42, 52]. If one assumes a conventional spacecraft construction, such an arrangement would be impossible.

To avoid undesired attitude changes, SEP thrusters are typically mounted at the end of the spacecraft bus such that their thrust vector is approximately aligned with the longitudinal axis of the spacecraft and passes through the center of mass. An illustrative example has been provided in Fig. 1.2 of the Hayabusa2 spacecraft. While some thruster gimballing is

Figure 1.2: Hayabusa2 firing its solar-powered gridded ion thruster

generally possible, this has historically been frequently limited to ±5 deg [68]. More recent spacecraft have increased this though, with the Dawn's gridded ion thruster assembly having a maximum range of 12 deg [69] and the upcoming Gateway Power and Propulsion Element offering 30 deg of deflection [70]. Solar sails have historically been mounted at the end of the longitudinal axis of the spacecraft such that the vast majority of the sail thrust – which is primarily in the sail anti-normal direction – similarly passes through the center of mass. In Fig. 1.1b, this would be through the "X" of the structural booms and into the floor. From an attitude control perspective, it is therefore logical that the SEP system would continue to be mounted at the end of the spacecraft such that the sail and SEP thrust vectors are approximately colinear.

Due to the limited gimbal range, multiple thrusters would need to be mounted on the spacecraft at a significant mass penalty to enable a fully independent thrust vector. Even then, their placement would not be easy. They cannot be on the sides of the spacecraft bus, for the SEP exhaust would impinge on the solar sail and may damage it. Nor can they be mounted on the ends of the solar sail booms; the booms are designed to be at lightweight as possible and could not be reasonably expected to support the forces of an EP thruster. Finally, even if a traditionally located SEP thruster could gimbal 90 deg and avoid impinging on the sail, one cannot fire through the sail. Another thruster on the opposite end of the longitudinal axis of the spacecraft would thus be required. To avoid the attitude control problems and mass penalty needed to realistically obtain a fully independent SEP vector, the propulsion model in this dissertation assumes a single, active thruster that is colinear with the sail normal direction.

1.2.4 Expected Contributions

In conclusion, the expected contributions to the body of literature are as follows.

1. An assessment of the ability of hybrid low-thrust propulsion to provide a net advantage in terms of (1) launch and delivered mass for a high-inclination heliocentric orbiter and (2) reduced relative flyby velocity of known and theoretical interstellar objects.

Table 1.3: Systems Modeling in the HLTP Literature

Paper	Sail Model	SEP Model	SEP Vector
Mengali and Quarta (2007)	McInnes Non-ideal	Power-based	Independent
Heiligers et al. (2011)	Ideal	Rocket Eq.	Independent
Gong et al. (2015)	Ideal	Rocket Eq.	Independent
Li et al. (2018)	Ideal	Rocket Eq.	Independent
Liu et al. (2018)	Ideal	Rocket Eq.	Independent
Miller et al. (2021)	McInnes Non-ideal	Power-based	Unified

2. An estimate of the sail performance necessary to achieve parity with solar electric propulsion and to provide context for this value with respect to the current state-of-the-art.

3. The development of a complete propulsion model that includes (1) a non-ideal sail model, (2) a power-based SEP model, (3) a power generation model that accounts for solar distance, and (4) a SEP thrust vector constrained to that sail anti-normal direction.[1]

[1]While the first three are commonplace on their own in the broader trajectory design literature, they have not yet been assembled together in the HLTP literature.

Chapter 2

Methodology

The following methodology may be split into two broad categories: the generalized optimization technique used to conduct the experiments and the problem modeling specific to this assessment of hybrid low-thrust propulsion. The former is addressed using a custom implementation of direct forwards-backwards multiple shooting, which is outlined in Section 2.1. The latter is composed of a combination of spacecraft systems modeling, mass estimates, and orbital mechanics. These are addressed in Sections 2.2, 2.3, and 2.4, respectively.

2.1 Optimization

The nature of a trajectory is not one that is frequently considered in day-to-day life. Formally, a trajectory is "the curve that a body describes in space" [71], which implies a continuous path. Less formally, and often more helpfully, it is instead a description of the steps that one must take to complete a journey: "turn left at the store" or "proceed until the light." In numerical methods of optimal control, this conversion of a continuous path and control law into a discrete sequence of states and actions is accomplished using a transcription method. Through the use of such a technique, the open-loop optimal control problem that defines a trajectory is converted into a nonlinear program (NLP), which may be solved with any number of common methods. The family of algorithms that utilize this conversion of an infinite-dimensional problem into a finite-dimensional one in order to create an NLP problem are known as direct methods. The alternative is to use an indirect method based on the calculus of variations. In an indirect method, a multiple-point boundary-value problem (BVP) is created and solved as a system of differential equations constrained by endpoint and/or interior point conditions [72].

In this work, a forward-backward multiple shooting (FBS) transcription is used, which has previously been included in other optimizers such as the Computer Algorithm for Trajectory Optimization (CATO), the Mission Analysis Low-Thrust Optimizer (MALTO), and the Evolutionary Mission Trajectory Generator (EMTG) [73]. The Automated Low THrust Evaluation and Analysis (ALTHEA)[1] optimization package used here takes the form of a wrapper that implements this transcription method around a commercial-off-the-shelf NLP

[1] "I told Althea I was feeling lost, lacking in some direction..." –Garcia/Hunter

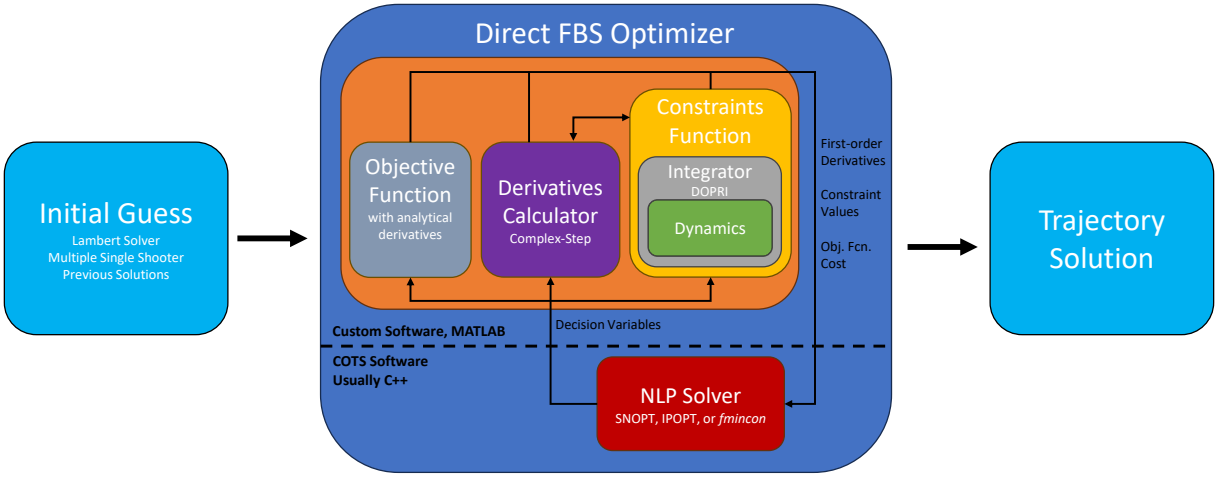

Figure 2.1: Optimization Overview

solver. On each iteration of the solver, the wrapper calculates the current cost of the objective function, the value of all constraints, and the first-order derivatives of both of these with respect to each variable defined by the transcription. The nonlinear programming solver – the Sparse Nonlinear OPTimizer (SNOPT) – then optimizes the decision variables $\mathbf{x}$ used to define the trajectory. A visual representation of this has been provided as Fig. 2.1. In the following sections, each of the major components outlined in this figure will be discussed. However, before doing so, it is necessary to explain the overarching concept of direct FBS in greater detail.

2.1.1 Forward-Backward Multiple Shooting Transcription

The quintessential example of the shooting transcription is the optimization of a cannonball's trajectory. Fired from a cannon with a fixed location to strike a downrange target, the cannonball's initial velocity vector – defined either as vertical and horizontal velocity components or a velocity magnitude and angle with respect to the horizon – is to be minimized. These two values to be optimized are known as decision variables and the resulting trajectory of the cannonball may easily be determined by integrating the ordinary differential equations of the dynamics. In other words, by "shooting" the cannon. By specifying a constraint that requires the cannonball's trajectory to hit the target, the solver may now optimize the decision variables to solve the problem. This method of transcription, with a single shooting arc originating from, and defined by, a set of decision variables located at the beginning of the arc is known as single forward shooting and is illustrated in Fig. 2.2a.

Two modifications to this basic method are now introduced. First, the trajectory is broken into N_{seg} smaller, discrete subtrajectories known as shooting segments, rather than a single shooting arc that spans the length of the problem. This creates a multiple shooting transcription in which the trajectory of each individual segment is defined by its own set of decision variables. By reducing the length of the shooting segments, the relationship between the decision variables, the objective function, and the constraints becomes more linear [74]

and the impact of any initial guess error is reduced [72]. It also allows for more complex problems to be solved in which the control input needs to vary over time. Forward-backward multiple shooting (FBS) further improves upon this transcription by defining the decision variables not at the beginning of each shooting segment, as with the original single forward shooting example, but at the center. This reduces the sensitivity to initial guess errors even further [75]. The states at the end of each segment, as determined by "shooting" the trajectory outwards half of a segment length from the center of the segment, are known as match points. By constraining the match points at the end of each segment to by equal to the match point at the start of the subsequent segment, a continuous final trajectory is produced. See Figs. 2.2b and 2.2c.

In the optimizer created for this work, a given trajectory problem is first split into a sequence of trajectory phases that begin and end at planets, with the exception of the final state, which may be located at a planet, a small-body, or a desired orbit. For example, the Jupiter-Earth-Earth gravity assist sequence used in Chapt. 3 has four phases: Earth-to-Jupiter, Jupiter-to-Earth, Earth-to-Earth, and Earth-to-Final Orbit. For a direct transfer, as in Chapt. 4, only a single phase is specified. To define the temporal length of these phases, $(N_{\text{phase}} + 1)$ decision variables are defined to specify the time of the beginning $t_{\text{i-1}}$ and the end t_{i} of each phase $i = 1, 2, ...N_{\text{phase}}$ of an N_{phase}-phase trajectory.

Within each phase, N_{seg} shooting segments are defined, each of an equal length of time, with a control point placed at the temporal center of each segment. The length of each of these segments is set to the overall temporal length of the phase divided by $(N_{\text{seg}} - 1)$. For the i^{th} trajectory phase, the length of each segment is therefore $(t_{\text{i}} - t_{\text{i-1}}) / (N_{\text{seg}} - 1)$. An exception is made, however, at the first and last segments of a given phase. These segments only contain the half of the segment that shoots towards the interior of the trajectory phase to connect with the match point of the adjacent segment within that phase.

To calculate the match point states at the ends of each segment, the spacecraft state consisting of mass, position, and velocity is propagated based on the underlying orbital mechanics with a zero-order hold on the control variables. For control points in the interior of a given phase, the full state representation and the control vector are both determined directly by the decision variables optimized at that point. However, for the control points at the phase boundaries, this would create an over constrained optimization problem. For these control points, the time, mass, velocity vector relative to the planet $\mathbf{v}_\infty$, and control vector are defined. During the trajectory propagation step, the full state is recovered using the position of the appropriate planet based at the specified time and by adding the planet's velocity to the relative velocity and thereby calculating the heliocentric velocity. A summary of the decision variables defined at different control points throughout a trajectory is provided in Table 2.1.

A continuous, feasible trajectory is made by enforcing a nonlinear constraint that the match points at the segment boundaries must be equal to one another. Consider the generic 2 phase trajectory illustrated by Fig. 2.3. This trajectory puts together all of the ideas introduced thus far. Each forward match point $\mathbf{s}_i^F$ must match the backward match point $\mathbf{s}_{i+1}^B$. The difference between them, the defect $\mathbf{d}_{i,i+1}$, is driven to zero by the NLP solver to ensure a continuous trajectory.

The NLP solver may take any combination of nonlinear inequality $\mathbf{c}_{\text{ineq}}(\mathbf{x}) \leq \mathbf{0}$, nonlinear equality $\mathbf{c}_{\text{eq}}(\mathbf{x}) = \mathbf{0}$, linear inequality $\mathbf{A} \cdot \mathbf{x} \leq \mathbf{b}$, and linear equality $\mathbf{A}_{\text{eq}} \cdot \mathbf{x} = \mathbf{b}_{\text{eq}}$ constraints.

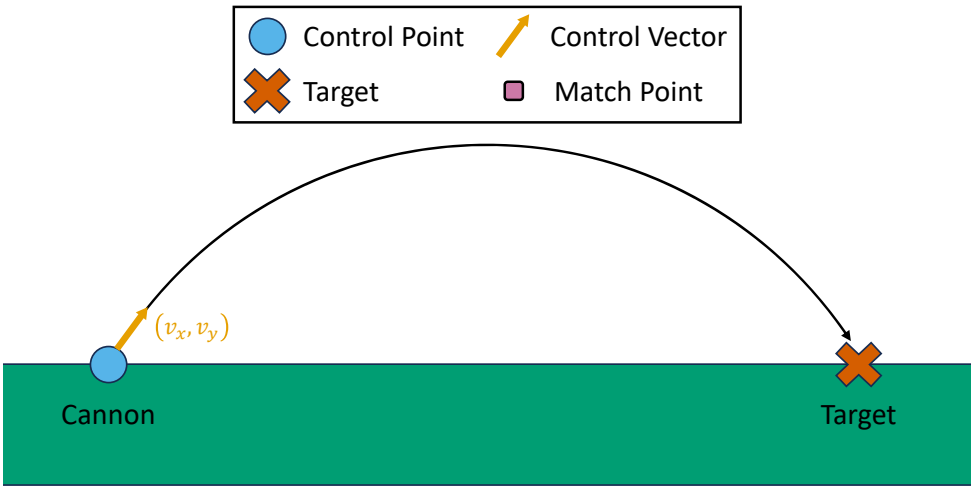

(a) Single Shooting

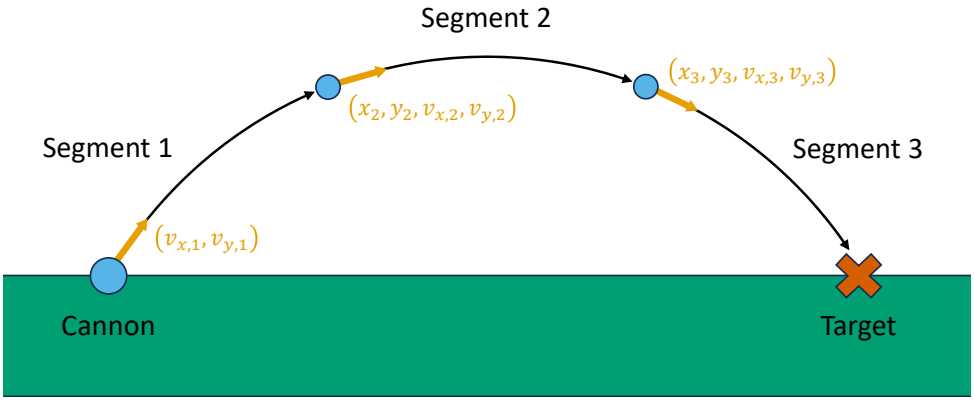

(b) Forward Multiple Shooting

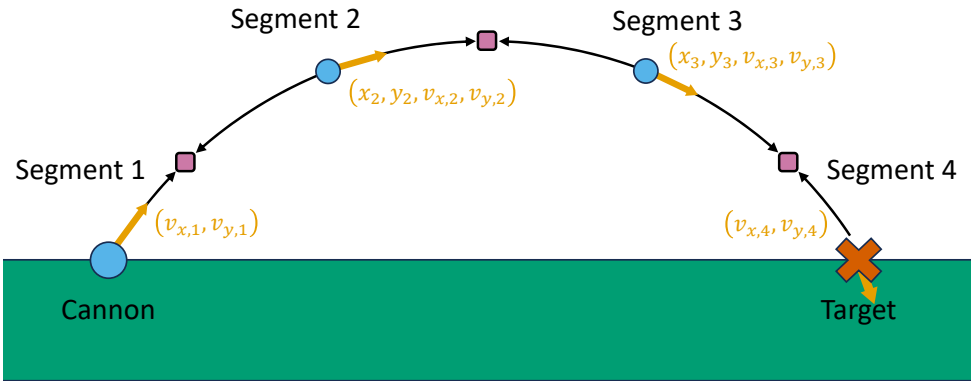

(c) Forward-Backward Multiple Shooting

Figure 2.2: A comparison of transcription methods on the classic cannonball trajectory problem

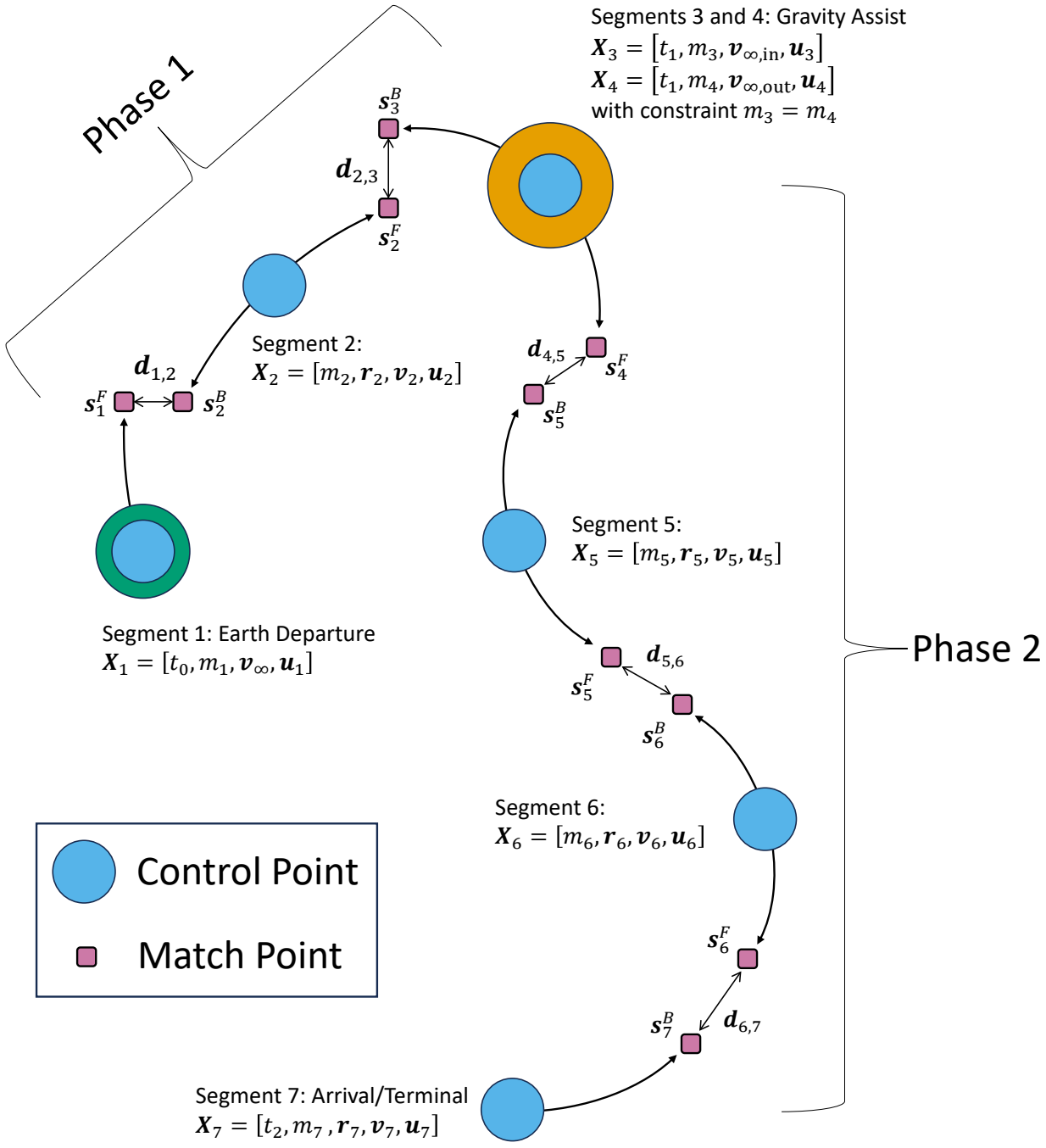

Figure 2.3: Direct Forward-Backward Multiple Shooting with 2 phases, 7 segments, and a gravity assist

Control Pt.	Required Variables	Optional Variables
Launch	$t_0, \mathbf{v}_\infty, \mathbf{u}_1$	m_1
Normal	$m_i, \mathbf{r}_i, \mathbf{v}_i, \mathbf{u}_i$	
Gravity Assist	$t_\mathrm{j} : 1 < j \leq N_\mathrm{phase}, m_i, \mathbf{v}_\infty, \mathbf{u}_i$	
Terminal	$t_\mathrm{N}, m_{N_\mathrm{seg}}, \mathbf{r}_{N_\mathrm{seg}}, \mathbf{v}_{N_\mathrm{seg}}, \mathbf{u}_{N_\mathrm{seg}}$	

Table 2.1: Decision Variables Variables Defined at Different Control Points. The launch mass may be set to a specific value or left free for the optimizer.

It also accepts both lower and upper bounds on the decision variables such that $\mathbf{lb} \leq \mathbf{x} \leq \mathbf{ub}$. The optimization problem may thus be written as:

$$\begin{aligned} \text{minimize} \quad & f(\mathbf{x}) \\ \text{s.t.} \quad & \mathbf{c}_\mathrm{ineq}(\mathbf{x}) \leq \mathbf{0} \\ & \mathbf{c}_\mathrm{eq}(\mathbf{x}) = \mathbf{0} \\ & \mathbf{A} \cdot \mathbf{x} \leq \mathbf{b} \\ & \mathbf{A}_\mathrm{eq} \cdot \mathbf{x} = \mathbf{b}_\mathrm{eq} \\ & \mathbf{lb} \leq \mathbf{x} \leq \mathbf{ub} \end{aligned} \tag{2.1}$$

The commercially available NLP solver SNOPT [76] is used to solve Eq. 2.1. For best performance, all of the decision variables are scaled to a similar magnitude.

One important consideration is that, as functions of the decision variables, the constraints are generally only satisfied at the control points; it is possible for a constraint violation to occur in the portion of the trajectory between them. For example, if a path constraint requires a minimum distance to the Sun to be maintained, this could only be guaranteed at the control points because those are the only states that are known to the NLP solver due to the nature of this discretized transcription. If constraint violation between control points is a serious issue, a higher density of control points may be specified for that particular trajectory phase.

2.1.2 Sequential Quadratic Programming

Since the SQP solver used here is a commercial-off-the-shelf product, only a brief description will be provided. A more thorough overview is available in Betts [77] and a complete description of the implementation contained within SNOPT may be found in Gill, Murray, and Saunders [76]. For a more practical guide to its implementation, see Nocedal and Wright [78]. All three of these were used in assembling the following subsection.

Consider a nonlinear programming (NLP) problem of the standard form

$$\begin{aligned} \text{minimize} \quad & f(\mathbf{x}) \\ \text{s.t.} \quad & h_j(\mathbf{x}) \geq 0 \quad \forall j \in \{1, \ldots, p\} \\ & g_i(\mathbf{x}) = 0 \quad \forall i \in \{1, \ldots, m\} \end{aligned} \tag{2.2}$$

that minimizes some objective function $f(\mathbf{x})$ and satisfies the constraints $h_i(\mathbf{x}) \geq 0$ and $g_j(\mathbf{x}) = 0$. These three requirements may be combined in a single Lagrangian with multipliers $\boldsymbol{\lambda}$ and $\boldsymbol{\mu}$ to be minimized [79].

$$\begin{aligned}\mathcal{L}(\mathbf{x}, \boldsymbol{\lambda}, \boldsymbol{\mu}) &= f(\mathbf{x}) + \sum_{i=1}^{m} \lambda_i g_i(\mathbf{x}) + \sum_{j=1}^{p} \mu_j h_j(\mathbf{x}) \\ &= f(\mathbf{x}) + \boldsymbol{\lambda}^{\mathrm{T}} \boldsymbol{g}(\mathbf{x}) + \boldsymbol{\mu}^{\mathrm{T}} \boldsymbol{h}(\mathbf{x})\end{aligned} \tag{2.3}$$

At the optimal solution, the four Karush-Kuhn-Tucker (KKT) conditions shall be satisfied. The first of these is stationarity, which states that gradient of this Lagrangian will be zero at the locally optimal solution $\mathbf{x}^*$.

$$\nabla_{\mathbf{x}} f(\mathbf{x}^*) + \boldsymbol{\lambda}^{\mathrm{T}} \nabla_{\mathbf{x}} \boldsymbol{g}(\mathbf{x}^*) + \boldsymbol{\mu}^{\mathrm{T}} \nabla_{\mathbf{x}} \boldsymbol{h}(\mathbf{x}^*) = \mathbf{0} \tag{2.4}$$

The second condition, primal feasibility, requires that all constraints have been satisfied.

$$\begin{aligned} h_j(\mathbf{x}^*) &\geq 0 \quad \forall j \in \{1, \ldots, p\} \\ g_i(\mathbf{x}^*) &= 0 \quad \forall i \in \{1, \ldots, m\} \end{aligned} \tag{2.5}$$

The third condition, dual feasibility, states that all of the nonlinear KKT multipliers are greater than or equal to zero.

$$\mu_j \geq 0 \quad \forall j \in \{1, \ldots, p\} \tag{2.6}$$

From a practical point of view, this condition ensures that that the nonlinear constraints term $\sum_{j=1}^{p} \mu_j h_j(\mathbf{x})$ is positive so that the minimization of Eq. 2.3 drives constraints towards zero, rather than blowing up the constraints. The final requirement is complementary slackness.

$$\sum_{j=1}^{p} \mu_j h_j(\mathbf{x}^*) = 0 \tag{2.7}$$

This ensures that strong duality holds, i.e. the locally optimal solution of the primal problem is also the solution to the dual problem and that the duality gap is zero. A proper explanation of what that means would unfortunately necessitate a deeper discussion of convex optimization and duality that is well outside the scope of this brief subsection. Its practical implication, however, is that at the locally optimal point $\mathbf{x}^*$ that satisfies these constraints, the KKT multiplier μ of an inactive nonlinear constraint $h(\mathbf{x}^*) > 0$ is zero. $\mu > 0$ only when $h(\mathbf{x}^*) = 0$.

To solve the problem posed in Eq. 2.2, SQP repeatedly solves a quadratic programming (QP) approximation that features linearized constraints about the current solution $\mathbf{x}_k$. At each iteration k of the algorithm, a new QP is defined at the current point $\mathbf{x}_k$ which itself is solved using another iterative process that will not be covered here. Before linearization, however, the inequality constraints in Eq. 2.2 are converted to equality constraints through the introduction of slack variables $\boldsymbol{s} = [\boldsymbol{s_N}, \boldsymbol{s_L}]^{\mathrm{T}}$, where $\boldsymbol{s_N}$ and $\boldsymbol{s_L}$ refer to those for nonlinear and linear constraints, respectively. For example, if the first nonlinear constraint was

previously $\sin(\mathbf{x}_1) \leq 8$, the new form would be be $\sin(\mathbf{x}_1) - s_1 = 0$. For simplicity, the set of all nonlinear constraints will now simply be referred to as $\boldsymbol{c}(\mathbf{x})$. The aforementioned constraint would thus now be $c_1(\mathbf{x}) - s_1 = 0$. These changes result in the following NLP problem.

$$\begin{aligned}
&\text{minimize} && f(\mathbf{x}) && (2.8)\\
&\text{s.t.} && \boldsymbol{c}(\mathbf{x}) - \boldsymbol{s_N} = \mathbf{0} && (2.9)\\
& && A_{\mathrm{L}}\mathbf{x} - \boldsymbol{s_L} = \mathbf{0} && (2.10)\\
& && \mathbf{lb} \leq \begin{pmatrix} \mathbf{x} \\ \boldsymbol{s_N} \\ \boldsymbol{s_L} \end{pmatrix} \leq \mathbf{ub} && (2.11)
\end{aligned}$$

Note that the linear constraints from Eq. 2.1 have now been added where $A_{\mathrm{L}} = [\mathbf{A}; \mathbf{A}_{\mathrm{eq}}]$. As with with the nonlinear inequality constraints, the linear inequality constraints are also converted to equalities through the use of slack variables.

Next, a basic tangent-line linearization is applied to all nonlinear constraints. At the current solution point $\mathbf{x}_k$, the nonlinear constraints are approximated as

$$\boldsymbol{c}(\mathbf{x_k}) + \nabla_{\mathbf{x}}\boldsymbol{c}(\mathbf{x})(\mathbf{x} - \mathbf{x_k}) - \boldsymbol{s_N} = 0 \tag{2.12}$$

while the equality restraints remain the same as in Eq. 2.10. This allows the new quadratic approximation to be written as

$$\begin{aligned}
&\text{minimize} && q_k(\mathbf{x}, \mathbf{x}_k) = \nabla_{\mathbf{x}}\boldsymbol{c}(\mathbf{x})^{\mathrm{T}}(\mathbf{x} - \mathbf{x_k}) + \frac{1}{2}(\mathbf{x} - \mathbf{x}_k)^{\mathrm{T}} H_{\mathrm{k}}(\mathbf{x} - \mathbf{x}_k) && (2.13)\\
&\text{s.t.} && A\mathbf{x} - \boldsymbol{s} = 0 && (2.14)\\
& && \mathbf{lb} \leq \begin{pmatrix} \mathbf{x} \\ \boldsymbol{s_N} \\ \boldsymbol{s_L} \end{pmatrix} \leq \mathbf{ub} && (2.15)
\end{aligned}$$

where H_{k} is a quasi-Newton approximation of the Hessian $\nabla^2_{\mathbf{x}}\mathcal{L}$ of the Lagrangian

$$\mathcal{L}(\mathbf{x}, \mathbf{x_k}, \boldsymbol{\lambda}, \boldsymbol{\mu}) = f(\mathbf{x}) - \begin{bmatrix} \boldsymbol{\lambda_k} \\ \boldsymbol{\mu_k} \end{bmatrix} (\boldsymbol{c}(\mathbf{x}) - \boldsymbol{c}(\mathbf{x_k}) - \nabla_{\mathbf{x}}\boldsymbol{c}(\mathbf{x})(\mathbf{x} - \mathbf{x_k})) \tag{2.16}$$

in which the final term after the Lagrange and KKT multipliers measures the difference between the true and linearized constraints.

Finally, having minimized the current quadratic approximation $q_k(\mathbf{x}, \mathbf{x}_k)$, a line search is conducted to determine the next iterate $(\mathbf{x_{k+1}}, \boldsymbol{s_{k+1}}, \boldsymbol{\lambda_{k+1}}, \boldsymbol{\mu_{k+1}})$. This is conducted using a merit function that combines the cost function $f(\mathbf{x})$, constraints $\boldsymbol{c}(\mathbf{x})$, and nonlinear slack variables $\boldsymbol{s_N}$ with a penalty matrix D. For a new iterate to be permissible, the merit function must decrease.

$$\phi(\mathbf{x}, \mu, s) = f(\mathbf{x}) - \boldsymbol{\mu}^{\mathrm{T}}(\boldsymbol{c}(\mathbf{x}) - \boldsymbol{s_N}) + \frac{1}{2}(\boldsymbol{c}(\mathbf{x}) - s)^{\mathrm{T}} D(\boldsymbol{c}(\mathbf{x}) - \boldsymbol{s_N}) \tag{2.17}$$

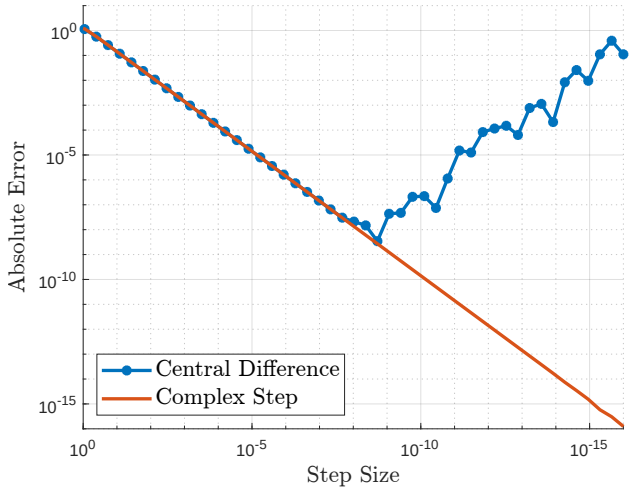

Figure 2.4: Comparison of Central Difference and Complex Step derivative of the function $\sin(x) + \cos(x)$ at $x = \frac{\sqrt{2}}{2}$.

2.1.3 Complex Step Differentiation

To enable the line search step of SQP, derivatives of the objective function and of all constraints with respect to all variables must be provided. Analytical derivatives would therefore ideally be used to maximize accuracy and minimize run time. Unfortunately, determining these derivatives for all possible combinations of constraints in a general purpose trajectory tool would be difficult and time consuming. A numerical method is thus preferable. A finite differencing method, such as a central difference, may be used. For example, for some function f at point x, the derivative may be approximated as

$$f(x)' \approx \frac{f(x+h) - f(x-h)}{2h} \tag{2.18}$$

when the step size h is small. Unfortunately, the accuracy of these methods are limited, as shown in Fig. 2.4. A better means of approximating these derivatives is complex step differentiation, which was first described by Squire and Trapp [80].

Starting with the same generic function as Eq. 2.18, consider the Taylor expansion about some complex variable $z = x + ih$.

$$f(x+ih) = f(x) + ihf'(x) - \frac{h^2 f''(x)}{2} - \frac{ih^3 f'''(x)}{3} + \dots \tag{2.19}$$

Next, isolate the imaginary parts and divide by the step size h.

$$Im\left[\frac{f(x+ih)}{h}\right] = f'(x) - \frac{h^2 f'''(x)}{3} + \dots \tag{2.20}$$

Finally, the higher-order terms are dropped and a new approximation is uncovered.

$$f'(x) \approx Im\left[\frac{f(x+ih)}{h}\right] \tag{2.21}$$

Algorithm 1 Monotonic Basin Hopping

procedure MBH($\mathcal{S}_{\text{IG}}, n_{\text{hops}}$)
  $[\mathcal{S}', \mathcal{C}', \mathcal{V}'] \leftarrow \text{solve}(\mathcal{S}_{\text{IG}})$ ▷ Run optimizer with initial guess
  $\mathcal{S} \leftarrow \mathcal{S}'$ ▷ Set new solution to current solution
  $\mathcal{C} \leftarrow \mathcal{C}'$ ▷ Set new cost to current cost
  $\mathcal{V} \leftarrow \mathcal{V}'$ ▷ Set new constraint violation to current violation
  for $i = 1 : n_{\text{hops}}$ **do**
    $\zeta = \text{pareto}(\mathcal{S})$ ▷ Generate perturbation
    $[\mathcal{S}', \mathcal{C}', \mathcal{V}'] = \text{solve}(\mathcal{S} + \zeta)$ ▷ Run optimizer using perturbed solution
    if $\mathcal{V}' \leq \mathcal{V}_{\text{req}}$ and $\mathcal{C}' < \mathcal{C}$ **then** ▷ New solution is feasible and cost improves
      $\mathcal{S} \leftarrow \mathcal{S}'$
      $\mathcal{C} \leftarrow \mathcal{C}'$
      $\mathcal{V} \leftarrow \mathcal{V}'$
    else if $\mathcal{V}' > \mathcal{V}_{\text{req}}$ and $\mathcal{V}' < \mathcal{V}$ **then** ▷ More feasible than current least infeasible
      $\mathcal{S} \leftarrow \mathcal{S}'$
      $\mathcal{V} \leftarrow \mathcal{V}'$
    end if
  end for
  return $\mathcal{S}$ ▷ Return best solution
end procedure

2.1.4 Monotonic Basin Hopping

Upon satisfying the first-order KKT conditions, the SQP solver will have found a locally optimal solution. However, it is possible for a more optimal solution to still exist elsewhere in the solution space. Various strategies have therefore been designed to enable the optimizer to better search for this globally optimal solution. One of these, Monotonic Basin Hopping (MBH), is employed here. In Chapter 3, the trajectory geometry is locked in by the gravity assist sequence, while the direct transfer of Chapter 4 is simple enough that the optimizer is able to make fairly large changes on its own. As a result, MBH is used in this investigation to assist in finding the optimal solution near to the original solution, rather that for searching distant portions of the solution space.

Originally developed to solve molecular conformation problems [81], MBH was brought to trajectory optimization by Addis, Cassioli, and Locatelli [82], Vasile, Minisci, and Locatelli [83] and Yam, di Lorenzo, and Izzo [84]. It was later included in the Evolutionary Mission Trajectory Generator (EMTG) and is thus associated with the work of its primary author, Jacob Englander, among other coauthors [85, 86, 75].

The implementation in this optimizer closely follows that of the publicly available source code of EMTG.[2] and is summarized in Algorithm 1. It starts by solving the optimization problem using a provided initial guess $\mathcal{S}'$. From this, the current solution $\mathcal{S}$, objective function cost $\mathcal{C}$, and constraint violation $\mathcal{V}$ are saved. The process of "hopping" then begins and will be repeated for a user-specified number of hops n_{hops}.

Each hop begins by sampling a pareto distribution to create a 1-by-m perturbation array

[2]https://github.com/nasa/EMTG

Algorithm 2 Pareto Distribution

procedure PARETO($\mathcal{S}$)
  $\epsilon \leftarrow 1 \times 10^{-13}$
  $\mathbb{S} \leftarrow 0.5$ ▷ Step size scaling factor
  $\alpha \leftarrow 1.4$ ▷ Pareto shape parameter
  $m \leftarrow \text{size}(\mathcal{S})$ ▷ Num. of variables to perturb
  $\mathcal{R} \leftarrow \text{rand}(1, m)$ ▷ A 1-by-m array sampled from uniform distribution $(0, 1)$
  $\mathcal{P} \leftarrow \frac{\alpha-1}{\epsilon} / \left(\frac{\epsilon}{\epsilon+\mathcal{R}}\right)^{-\alpha}$ ▷ Sample Pareto distribution
  $\mathcal{N} \leftarrow \text{rand}(1, m)$ ▷ Create an array to randomly set positive or negative
  $\mathcal{N}(\mathcal{N} \geq 0.5) \leftarrow 1$
  $\mathcal{N}(\mathcal{N} < 0.5) \leftarrow -1$
  $\zeta \leftarrow \mathcal{N}\mathcal{P}\mathbb{S}$ ▷ Calculate perturbation
  return ζ
end procedure

where m is equal to the number of decision variables, excluding those related to the time of events (e.g. launch date) and optional Sundman transformation variables.[3] The shape of this pareto distribution is defined by a tuning parameter α and is scaled according to a scaling factor $\mathbb{S}$. Each individual entry in the perturbation array is also randomly assigned a positive or negative sign. The process of calculating this array is summarized as Algorithm 2.

Having sampled the pareto distribution, the decision variables from the previous solution are perturbed and the optimizer is run once more. If the new solution $\mathcal{S}'$ is feasible – as defined by the constraint violation $\mathcal{V}'$ being less than or equal to the upper violation limit $\mathcal{V}_{\text{req}}$ – and the cost $\mathcal{C}'$ has improved, then the new solution is saved as the current solution. The current cost $\mathcal{C}$ and violation $\mathcal{V}$ are also updated. If all previous solutions have been infeasible, then the solution and violation will be updated solely by checking if the new solution is less infeasible than the current solution. Finally, after n_{hops} hops are completed, the MBH algorithm returns the best solution.

2.1.5 High-Performance Computing Parallelization

To minimzize run time, extensive parallelization was implemented to take advantage on high-performance computing (HPC) resources provided by the MIT Supercloud [88]. Two layers of parallelization were used. The first was at the individual trajectory level, where the calculation of the Jacobian was shared among up to 20 cores on a single node using a *parfor* loop. The second was at the job level for trade study tasks, such as that conducted in Chapter 3. In these cases, worker-leader parallelization was implemented to intelligently manage resources across multiple HPC nodes.

In a worker-leader parallelization scheme, a single "leader" HPC node keeps track of all of the individual subtasks necessary to complete the larger task and decides how to allocate the resources of the various "worker" HPC nodes with which it has been provided. In this case, its

[3]The option of using a generalized Sundman transformation.[87] is not used in this dissertation.

role is to efficiently solve a trade study of two variables which, for the sake of generalization and simplicity, will be referred to as TSx and TSy. This is in reference to their position on the x and y axes of the trade study mesh. The leader determines which tasks to assign to each worker, keeps track of ongoing and completed jobs, and decides which previously solved tasks it should use an initial guess for subsequent, similar tasks. Meanwhile, each worker node solves their assigned trajectory problem, saves the solution, and finally reports back to the leader with a summary of the solution. It will then await the next assigned task.

Consider a trade study over two variables that have been incremented in five values as shown in Fig. 2.5. In this example, four worker nodes are shown to be available to the leader in Fig. 2.5a. For the actual experiments, seven workers were normally available. Before starting the trade study, the solution to the $(1, 1)$ location on the job mesh of Fig. 2.5b is solved for and used to seed the trade study. The general strategy will be to work from the bottom left to the top right of the mesh. Underlying this decision is the knowledge that there will only be one family of solutions because, in the case of the actual experiment in Chapter 3, the geometry of the trajectory is largely locked in by the selection of planetary flybys. Should more than one family of solutions have been found, it would have been necessary to seed the trade study from multiple locations and use a more complex arrangement.

Upon beginning the trade study, the leader node assesses which jobs have not been attempted and which of these have adjacent, successfully solved solutions. For any given unsolved mesh location, the leader will use a clockwise search from the bottom position to find a solution that can be used as an initial guess. For example, for a job in position $(3, 3)$, the leader will check if a solution is available following the search pattern $(3, 2)$, $(2, 3)$, $(3, 4)$, and $(4, 3)$. This was done partially for simplicity and partially because problems are expected to become more difficult as they deviate from the bottom left corner of the trade study. After the job initialization of Fig. 2.5, the solution to the job at position $(1, 1)$ is used to seed those at $(2, 1)$ and $(1, 2)$ and these tasks are given to worker nodes 1 and 2, respectively. This results in the status shown in Fig. 2.6.

Over time, the leader continues to assign tasks and work its way through the trade study mesh. As the leader explores the boundaries of the feasible region, it is possible that jobs will begin to fail. Such a situation is shown in Fig. 2.7. Having successfully completed the tasks at positions $(1, 3)$ and $(2, 3)$, the jobs at $(1, 4)$ and $(2, 4)$ were both attempted. Unfortunately, only $(2, 4)$ was successful, which in turn only allowed for task $(2, 5)$ to be attempted. Job $(1, 5)$ would have to wait for the completion of $(2, 5)$ in order to have a valid initial guess. Since job $(2, 5)$ then also failed, the job at $(1, 5)$ became inaccessible.

This situation has also resulted in a waste of resources because worker node 4 now has no task to solve. In general, if one assumes a diagonal front of in-progress tasks sweeping across the mesh (as shown in 2.7b), the maximum number worker nodes that may be utilized is equal to the maximum diagonal length of the mesh. While it is possible to exceed this if the front takes a form that is not a straight line, in general fewer resources will always be used than this length, not more. This is because the diagonal from the y-axis to the x-axis will be shorter than the maximum at any other point in the completion of the trade study. It is important to balance both the density of the mesh and the requested number of nodes both to ensure a manageable run time and to avoid wasting public HPC resources.

After some period of time, the worker nodes will have attempted all of the accessible jobs. In the situation illustrated by Fig. 2.8, one additional job failed at $(4, 4)$, in addition

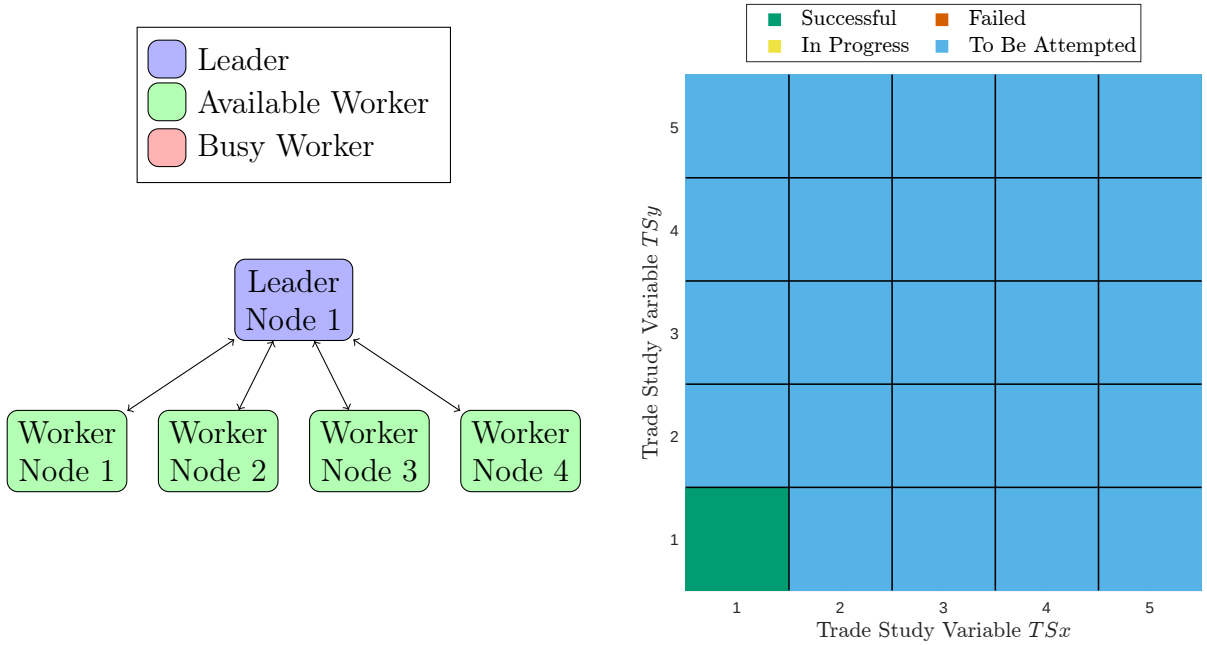

(a) HPC Node Status

(b) Trade Study Grid Status

Figure 2.5: Worker-leader status at job initialization. In this example, one leader node controls four worker nodes. The $(1, 1)$ grid job has been provided to seed the trade study.

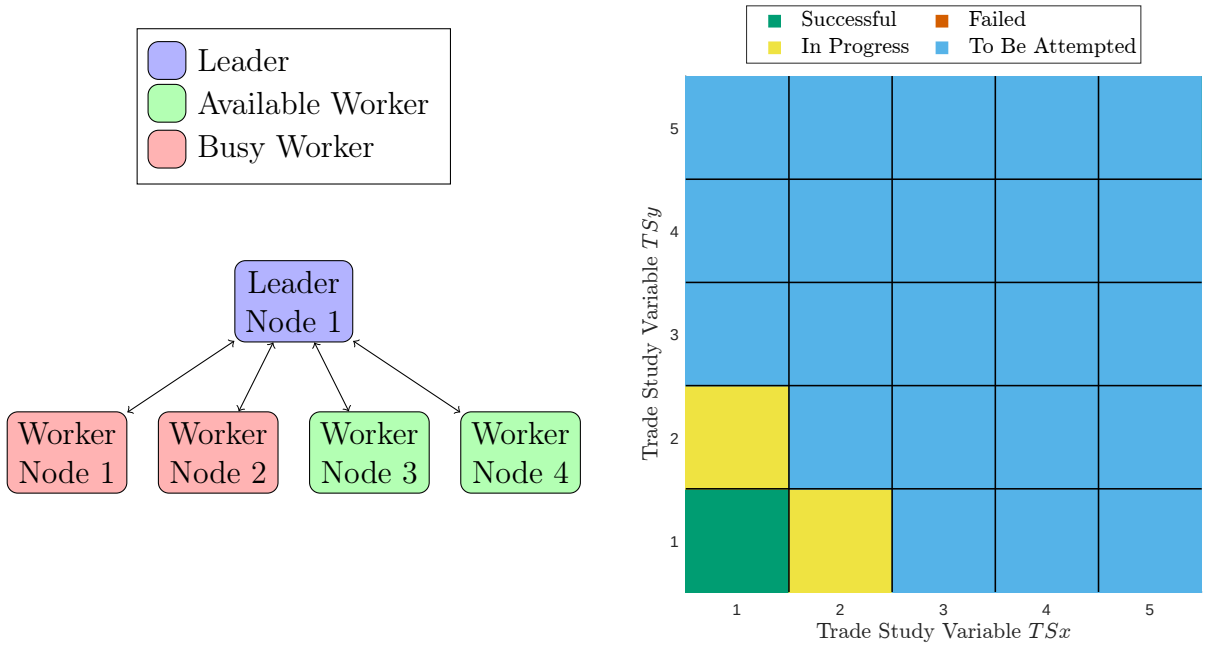

(a) HPC Node Status

(b) Trade Study Grid Status

Figure 2.6: Worker-leader after trade study begins. The seeded solution at position $(1, 1)$ has been used to start jobs $(2, 1)$ and $(1, 2)$. Two workers are now busy, while the remaining two remain available.

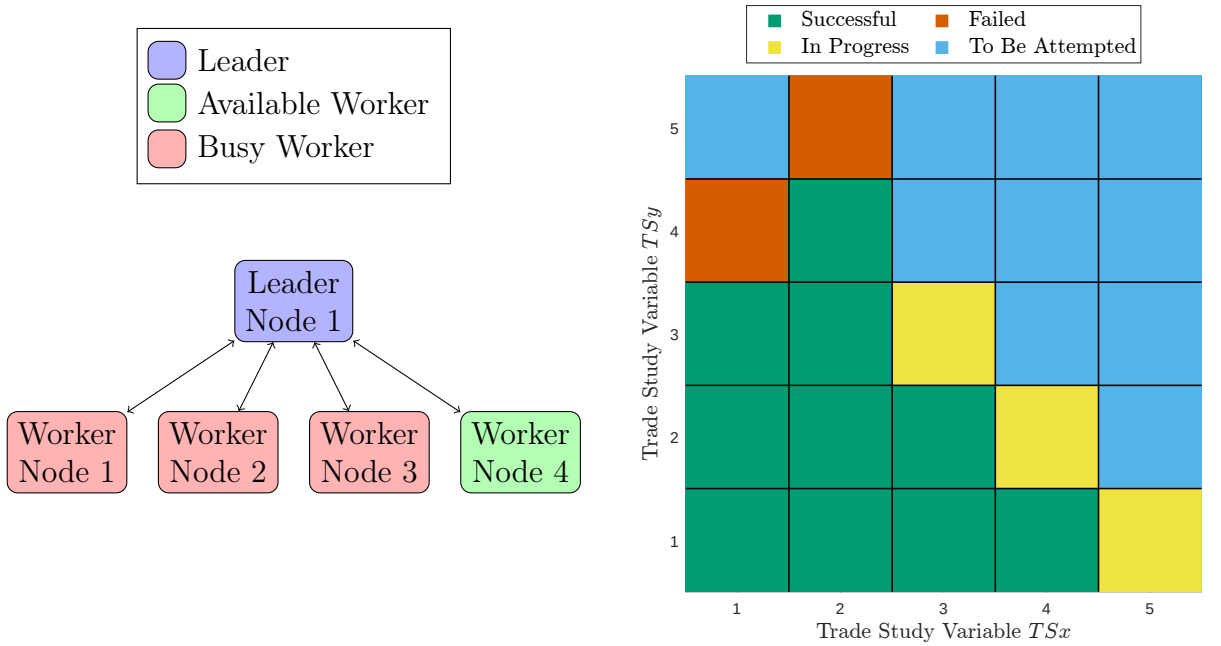

(a) HPC Node Status

(b) Trade Study Grid Status

Figure 2.7: Worker-leader status midway through trade study. The job at position $(1, 5)$ is unreachable because both adjacent jobs have failed. At present, there are not enough jobs available with valid guesses, so worker node 4 remains available.

to the previously discussed failed jobs at the top left and the resulting inaccessible job at $(1, 5)$. A cleanup routine was designed for such a situation that would improve the success rate and ensure that all jobs were actually attempted. Initiated by the dual requirements of (1) no accessible jobs remaining and (2) all worker nodes being available, the leader will now retry any failed or unattempted jobs. However, it will now use a counter-clockwise search pattern from the right-hand position. For example, in the case of the grid status shown in Fig. 2.8b, the initial guess for position $(4, 4)$ would be the solution to $(5, 4)$. Additionally, after attempting all jobs that are accessible with adjacent solutions, the leader will widen the search to a distance of two grid slots if necessary. Therefore, if the jobs at $(1, 4)$ and $(2, 5)$ fail to converge a second time, the solution to either $(3, 5)$ or $(1, 3)$ will be used.

A common final grid status is shown in Fig. 2.9. It is not uncommon for one portion of the trade space to fail to converge due to it exceeding feasible region of the underlying problem. For example, if TSy is weight, the spacecraft may have become too heavy for the trajectory to be flyable. This will be discussed further when analyzing the results of Chapter 3.

2.2 Spacecraft Power and Propulsion Modeling

To address the shortcomings in the modeling identified in the previous chapter, nonidealized sail models are now defined for the solar sail, the solar arrays, and the SEP system. A basic, idealized bipropellant system is also introduced for a limited use case in Chapt. 4.

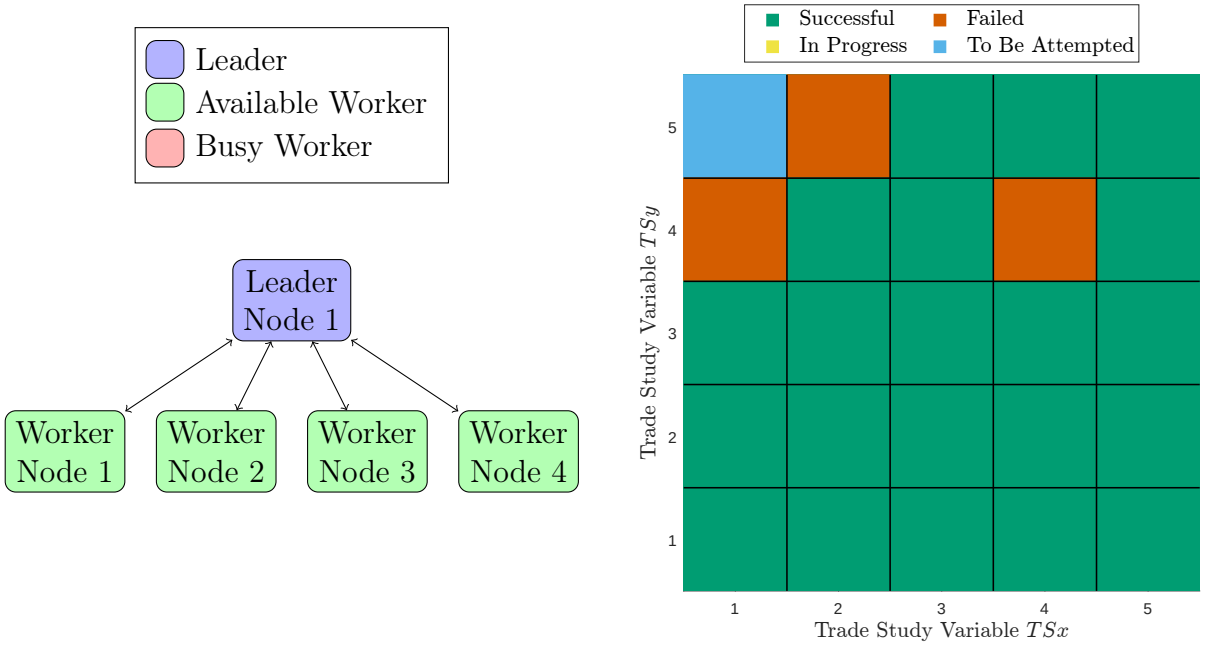

(a) HPC Node Status

(b) Trade Study Grid Status

Figure 2.8: Worker-leader status after attempting all jobs. In addition to the inaccessible region at the top left, one additional job failed as position $(4, 4)$. With no accessible jobs remaining and all worker nodes free, the cleanup mode will be activated.

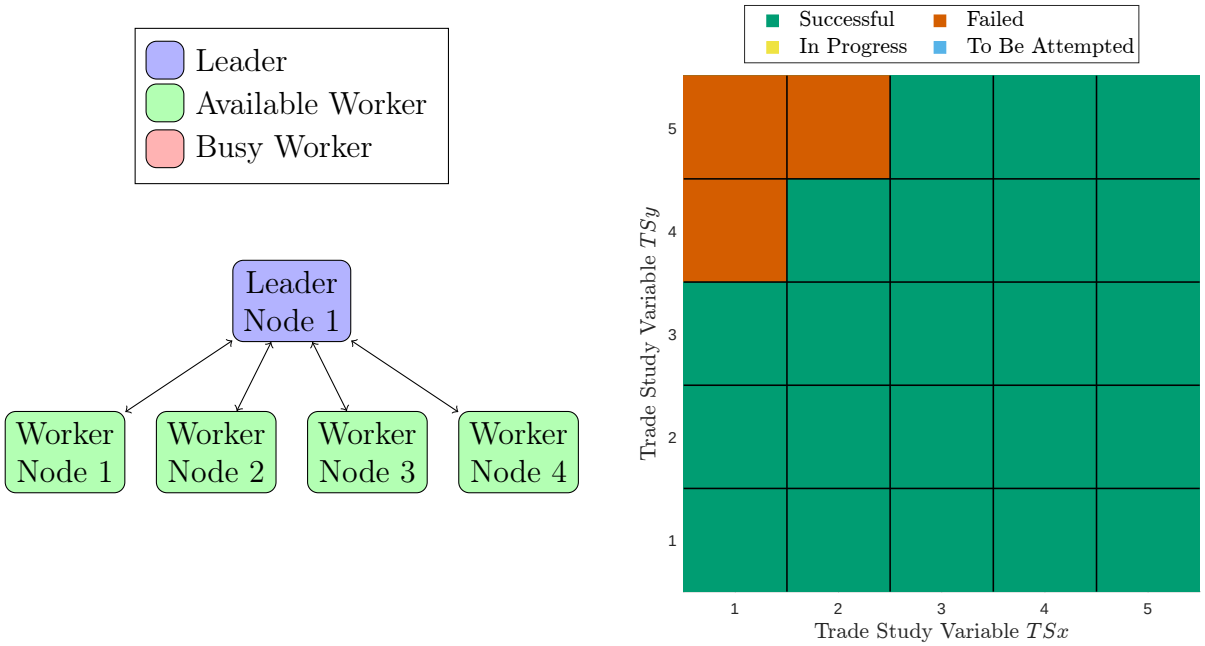

(a) HPC Node Status

(b) Trade Study Grid Status

Figure 2.9: Worker-leader status after cleanup and at shut down. While the top left portion of the trade study grid failed to converge due to the underlying problem physics, all jobs were attempted.

2.2.1 McInnes Nonideal Optical Sail Model

At its simplest, a solar sail accelerates as a result of a change in momentum imparted by the reflection of photons from the Sun. Fundamental to this is solar radiation pressure, or the force applied to a surface as a result of this effect. This is approximately $4.56\,\mu\mathrm{N\,m^{-2}}$ at 1 au and varies with the inverse of distance $r_{\mathrm{S,s/c}}$ squared.

$$P_{\mathrm{SRP}} = 4.56\,\mu\mathrm{N\,m^{-2}} \left(\frac{1\,\mathrm{au}}{r_{\mathrm{S,s/c}}}\right)^2 \tag{2.22}$$

In the idealized sail model, rays of incident light from the Sun are assumed to reflect specularly; parallel rays of inbound light remain parallel after striking the sail. The thermal and absorptive properties of the sail are not considered. With these assumptions, inbound incident light and outbound reflected light produce two force vectors that are mirrored across the sail normal vector, as shown in Figure 2.10a. As a result of this symmetry, they sum to a single force vector normal to the sail and away from the Sun. Varying with the squared cosine of the Sun-Sail incidence angle θ, the force imparted by an ideal sail with area A_{sail} may be written as

$$F_{\mathrm{ideal}} = 2P_{\mathrm{SRP}} A_{\mathrm{sail}} \cos^2\theta \tag{2.23}$$

To represent the aforementioned neglected properties, the optical solar sail model described by McInnes [21] is employed with updated coefficients developed for the NEA Scout mission [14]. These coefficients have been provided in the Appendix as Table A.1. To account for the absorption of a portion of incident photons, $\tilde{r} \in [0, 1]$ is defined to specify the fraction of light that is reflected. Some further fraction of this reflected light $s \in [0, 1]$ of the light will be experience specular reflection. The remaining light will undergo diffuse reflection, which results in the symmetry of the idealized model being lost and a tangential force being introduced. This is shown in Fig. 2.10b. Note that if both $\tilde{r}$ and s are set to 1, the optical model of Eqs. 2.24 and 2.25 reverts back to the ideal model of Eq. 2.23.

Diffuse reflections take two forms in the optical sail model. One portion of the diffusely reflected light will undergo uniform scattering. This maintains a degree of symmetry and therefore produces a force in the sail normal direction. This second term in Eq. 2.24 is a function of the sail's deviation B_{f} from a Lambertian surface: one that appears equally bright from all viewing angles. The other form of diffuse reflections are those that scatter non-uniformly. This makes up the entirety of the tangential force defined by Eq. 2.25.

As a large structure in constant sunlight, solar sails must be designed with thermal balance in mind. The final, non-reflected portion of light is that of absorbed photons. This results in a thermal input that is then radiated outwards by the front and back surfaces of the sail. The apportionment of this power output between the front and back surfaces is based on the emissivity and Lambertian coefficients of the front and rear surfaces ϵ_{f}, ϵ_{b}, B_{f}, and B_{b}. Should $\epsilon_{\mathrm{f}} B_{\mathrm{f}} > \epsilon_{\mathrm{b}} B_{\mathrm{b}}$, the majority of the thermal output will be radiated from the front of the sail, thus resulting in a force in the direction of the sail normal. Using the coefficients in Table A.1, $\epsilon_{\mathrm{f}} B_{\mathrm{f}} \approx 0.02$ and $\epsilon_{\mathrm{b}} B_{\mathrm{b}} \approx 0.18$, resulting in thrust in the anti-normal direction. Thankfully, this is offset by first and second terms, which collectively are approximately 37 times and 1.6 times greater, respectively, when the incidence angle is zero.

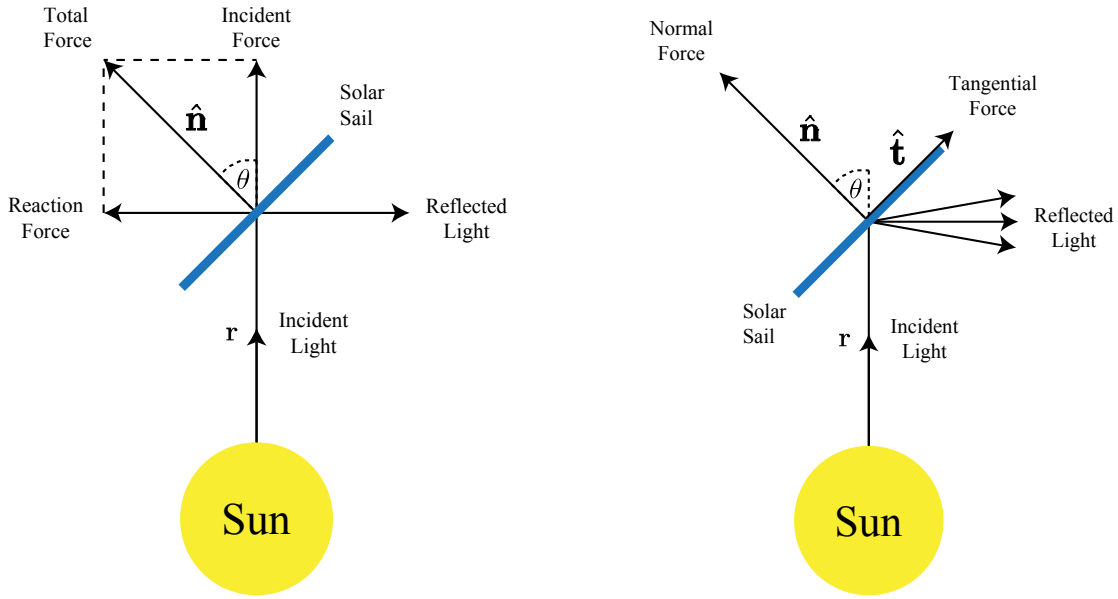

(a) Ideal (b) Optical

Figure 2.10: Sail Models

$$F_{\mathrm{n}} = P_{\mathrm{SRP}} A_{\mathrm{sail}} \left\{ (1 + \tilde{r}s) \cos^2 \theta + B_{\mathrm{f}} (1 - s) \tilde{r} \cos \theta + (1 - \tilde{r}) \frac{\epsilon_{\mathrm{f}} B_{\mathrm{f}} - \epsilon_{\mathrm{b}} B_{\mathrm{b}}}{\epsilon_{\mathrm{f}} + \epsilon_{\mathrm{b}}} \cos \theta \right\} \tag{2.24}$$

$$F_{\mathrm{t}} = P_{\mathrm{SRP}} A_{\mathrm{sail}} (1 - \tilde{r}s) \cos \theta \sin \theta \tag{2.25}$$

2.2.2 Power Generation Model

The missing step between solar energy and the production of thrust is that of power generation. SEP systems are only operational between minimum and maximum operating power levels. Should power drop below some P_{min}, the thruster must be turned off, even if some small amount of power is still available. Similarly, above some P_{max}, the input power must be capped. The power generated by the solar array $P_{\mathrm{generated}}$ varies primarily with the inverse of distance squared $r_{\mathrm{S,s/c}}^{-2}$, along with some additional higher order terms that better characterize the properties of a specific solar array. The full set of coefficients may be found in Table A.2.

$$P_{\mathrm{generated}} = \frac{P_0}{r_{\mathrm{S,s/c}}^2} \left(\frac{\gamma_0 + \frac{\gamma_1}{r_{\mathrm{S,s/c}}} + \frac{\gamma_2}{r_{\mathrm{S,s/c}}^2}}{1 + \gamma_3 r_{\mathrm{S,s/c}} + \gamma_4 r_{\mathrm{S,s/c}}^2} \right) \tag{2.26}$$

In Eq. 2.26, the standard power available at 1 au P_0 is assumed to be consistently available. This may be achievable if the solar panels are mounted in such a way that they can consistently orient themselves towards the Sun. Due to the constraint upon the hybrid spacecraft to always face the Sun, it is reasonable that such a requirement could be met.

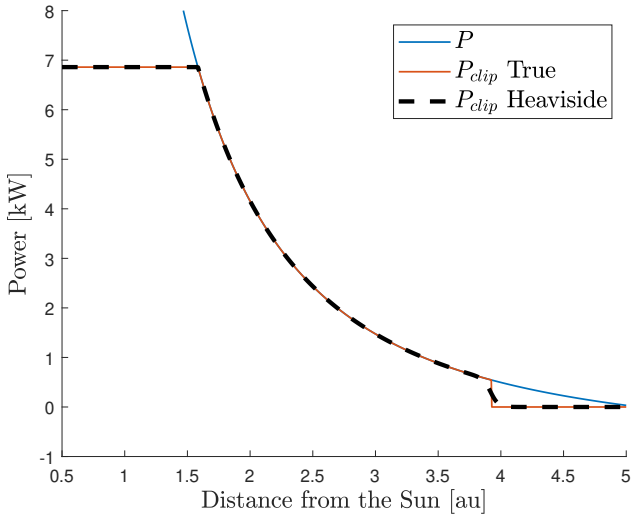

Figure 2.11: Power Model

Next, the power required for the spacecraft's electrical bus P_{bus} – that is, for its non-propulsion systems – is subtracted and a power margin δ_{power} is applied. The resulting value P is the power available at any time for the thruster.

$$P = (1 - \delta_{\text{power}}) (P_{\text{generated}} - P_{\text{bus}}) \tag{2.27}$$

To ensure that this value stays within the permitted range between P_{min} and P_{max}, three Heaviside approximation functions

$$H_i (P) = \frac{1}{1 + \exp(-2\alpha (P - P_i^*))} \tag{2.28}$$

are used as switches. These functions return zero when below a switching value P_i^* and return one above it, with the sharpness of the transition controlled by α. The true behavior

$$P_{\text{clip}} = \begin{cases} 0 & \text{if } P < P_{\text{min}} \\ P & \text{if } P_{\text{min}} \leq P \leq P_{\text{max}} \\ P_{\text{max}} & \text{if } P_{\text{max}} < P \end{cases} \tag{2.29}$$

is approximated as

$$P_{\text{clip}} = H_1 (P) * (1 - H_2 (P)) * P + H_2 (P) * P_{\text{max}} \tag{2.30}$$

where H_1 goes to one when power rises above $P_1^* = P_{\text{min}}$ and $(1 - H_2 (P))$ goes to zero when $P_2^* = P_{\text{max}}$. Using a sharpness of $\alpha = 25$, this results in a close approximation of the desired behavior, as shown in Fig. 2.11.

2.2.3 Power-based SEP Model

Real electric propulsion systems do not produce thrust in a continuously variable manner. Rather, they have discrete throttle points that each correspond to a specific thrust and mass

flow rate at a given input power. Furthermore, a range of thrust magnitudes and flow rates may be available at different specific impulses at the same input power, thus creating a sequence of settings that vary from high-thrust to high-efficiency. In this work, however, a continuous and smooth model is required to be compatible with the underlying gradient-based optimization methodology. Therefore, high-order polynomials are used to represent the thrust and mass flow rate as functions of power [89]. These are each curve fits of a particular subset of the throttle points for the associated thruster.

First, to determine the propulsion model's input power, a control decision variable u_T is introduced.

$$P_{\text{en}} = P_{\text{clip}} u_T \tag{2.31}$$

where P_{en} is the power sent to the propulsion system (i.e., engine power). The resulting thrust and mass flow rate are then calculated as

$$F_{\text{SEP}}\left(P_{\text{en}}\right) = a_{\text{T}} P_{\text{en}}^4 + b_{\text{T}} P_{\text{en}}^3 + c_{\text{T}} P_{\text{en}}^2 + d_{\text{T}} P_{\text{en}} + e_{\text{T}} \tag{2.32}$$

$$\dot{m}\left(P_{\text{en}}\right) = a_{\text{m}} P_{\text{en}}^4 + b_{\text{m}} P_{\text{en}}^3 + c_{\text{m}} P_{\text{en}}^2 + d_{\text{m}} P_{\text{en}} + e_{\text{m}} \tag{2.33}$$

using the coefficients provided in Table A.3.

2.2.4 Bipropellant Chemical Propulsion

A bipropellant (biprop) propulsion option is included in Chapt. 4 as an alternative to low-thrust options for interstellar object flyby missions. Modeled as an impulse applied at the moment of the flyby, the biprop trajectories are otherwise assumed to be ballistic. Using the rocket equation, the change in velocity ΔV is determined by

$$\Delta V = I_{\text{sp}} g_0 \ln \frac{m_0}{m_{\text{f}}} \tag{2.34}$$

with an assumed specific impulse of 320 sec. The exact ΔV is determined by the optimizer by controlling the launch mass of the spacecraft. This is explained further in a broader discussion of mass modeling and systems sizing within Section 2.3.

2.2.5 Reaction Control System

For all of the spacecraft defined in Chapt. 3 and for the hall-effect, gridded ion, bipropellant, and hybrid low-thrust cases of Chapt. 4, a reaction control system (RCS) is specified for attitude control. While the optimization problem treats the spacecraft as a point mass, RCS propellant is assumed to be consumed at a constant rate such that 80% of the allocation is used over the course of any given trajectory.

2.2.6 Launch Vehicle Modeling

All of the trajectory optimization contained within this work is conducted in the heliocentric two-body problem with a spacecraft of negligible mass. The launch phase of the mission is accordingly not modeled. Instead, the initial velocity at Earth departure is constrained by the excess velocity of the spacecraft at Earth escape $\mathbf{v}_\infty$. As per standard practice, this is measured in terms of characteristic energy $C_3 = \mathbf{v}_\infty^2$ which must be less than the limiting value defined by the maximum performance of the launch vehicle $C_{3,\max}(m_0)$ at the spacecraft's initial mass m_0. These values are calculated using polynomial curve fits of data provided by the NASA Launch Vehicle Performance Website.[4]

2.3 Spacecraft Mass Budgeting

With one of the most important success criteria being a positive change in the payload mass fraction, accurate mass budgeting is critical to the assessment of HLTP. In this section, the method by which spacecraft mass has historically been estimated in the literature will first be explained. By applying these equations to a known spacecraft, their deficiency will then be demonstrated. This will be followed by a discussion of current best practices that are to be followed in this dissertation. Finally, a deeper explanation into the current state of solar sail development will be provided to motivate the chosen method of estimating sail mass.

2.3.1 Pre-existing Literature Methodology

From Li et al. [42] and Heiligers et al. [50], the initial spacecraft mass m_0 may be modeled as

$$m_0 = m_{\text{prop}} + m_{\text{tank}} + n_{\text{thruster}}\left(m_{\text{SEP}} + m_{\text{gimbal}}\right) + m_{\text{solar}} + m_{\text{sail}} + m_{\text{rad}} + m_{\text{payload}} \tag{2.35}$$

with propellant mass m_{prop}, propellant tank mass m_{tank}, number of thrusters n_{thruster}, SEP thruster and gimbal assembly masses m_{SEP} and m_{gimbal}, solar array mass m_{solar}, sail mass m_{sail}, radiators mass m_{rad}, and payload mass m_{payload}. While variations upon this equation exist in the literature, they all represent a summation of estimates of subsystem masses. The literature most commonly uses a set of proportional equations, defined as follows.

From Gershamn and Seybold [90], the propellant tank mass may be estimated as

$$m_{\text{tank}} = 0.1 m_{\text{prop}} \tag{2.36}$$

while the mass of the thruster is calculated as a function of its performance thrust F_{SEP}, specific impulse I_{sp}, electrical efficiency η, and a mass per kilowatt coefficient that Ceriotti and McInnes defines as $k_{\text{SEP}} = 20\,\text{kg}\,\text{kW}^{-1}$ [47, 45, 46].

$$m_{\text{SEP}} = k_{\text{SEP}} \frac{F_{\text{SEP}} I_{\text{sp}} g_0}{2\eta} \tag{2.37}$$

[4] https://elvperf.ksc.nasa.gov/Pages/Default.aspx

The mass of the gimbal assembly is estimated based on a dimensionless coefficient that is commonly defined as $k_{\text{gimbal}} = 0.3$ for HLTP and $k_{\text{gimbal}} = 0.1$ for SEP-only [90, 42].

$$m_{\text{gimbal}} = k_{\text{gimbal}} m_{\text{SEP}} \tag{2.38}$$

The choice of a conventional solar array or a solar power sail determines the mass of both the solar cells and the (propulsive) sail. For a spacecraft with traditional solar panels, the sail area may be calculated as the areal density of the sail σ_{sail} multiplied by the area of the sail A_{sail}.

$$m_{\text{sail}} = \sigma_{\text{sail}} A_{\text{sail}} \tag{2.39}$$

The solar panel mass may then be determined based on COTS specifications. Alternatively, thin-film solar panels may be specified instead. Developed by JAXA and demonstrated on the IKAROS mission [91], solar cells are embedded in the solar sail to create a hybrid solar power sail. Since the propulsive and power generating portions of the hybrid sail will have different properties, their masses are defined separately. Heiligers et al. [50] calculate the required solar cell portion of the overall hybrid sail area as

$$A_{\text{TF}} = \frac{P_{\max}}{W \eta_{\text{solar}}} \cos \theta_{\max} \tag{2.40}$$

with maximum spacecraft power $P_{\max}$, solar flux $W = 1367\,\text{W m}^{-2}$, solar cell efficiency η_{solar}, and maximum incidence angle $\theta_{\max}$. The propulsive area of the hybrid sail is then calculated based on the desired performance. Using the sail lightness number, the combined solar and power sail area is then

$$A_{\text{sail}} = \frac{\beta m_0}{\sigma^*} + A_{\text{TF}} \tag{2.41}$$

and the sail mass calculated according to Eq. 2.39 with an appropriate value of σ_{sail} for a hybrid sail.

Radiator mass varies in the literature. Li, Wang, and Zhang define it as zero $m_{\text{rad}} = 0$ as per the work of Li [42] and Ceriotti and McInnes [47, 45, 46] define it as

$$m_{\text{rad}} = 0.0086\,\text{kg W}^{-1} P_{\text{ex}} \tag{2.42}$$

where P_{ex} is the maximum, unused excess power produced by the solar arrays. This model assumes the use of a shared radiator-hybrid power sail structure.

2.3.2 Limitations of the Current Methodology

While the mass model defined in the previous section are easily scalable and generalizable, its accuracy is questionable. Consider the SMART-1 spacecraft, whose mass budget was outlined in detail by Racca [2]. Using a mixture of the aforementioned mass model and published values where appropriate, a theoretical mass budget is calculated and provided in Table 2.2. Comparing this budget against the true mass budget shown in Table 2.2, the methods in the literature are seen to underestimate the real-world value by nearly 46%. This deficiency is primarily caused by an insufficiently granular mass model; the theoretical model

is missing too many systems. In particular, at 13.8% of the real-world wet mass, the lack of structural mass stands out as a significant omission.

In addition to underestimating the mass, the current procedures fail to follow current best practices for mass modeling and, in doing so, tend towards overly optimistic values. These estimates all represent "basic mass" values, without any budget for actual systems being delivered at higher-than-anticipated masses. To produce a more conservative mass estimate, mass growth allowances (MGAs) and margins will be introduced in the next section. This will have the added benefit of more rigorously proving the benefits of HLTP, should they be found to exist. If HLTP can be proven to provide an advantage at higher vehicle masses, then it will also be shown to beneficial at lower, more optimistic masses.

2.3.3 Margins and Growth Allowances

With the goal of creating a realistic baseline from which to evaluate the hybrid low-thrust concept, Master Equipment Lists (MELs) were defined for each spacecraft. Each of these MELs combines subsystem-level basic mass estimates with mass growth allowances, an overall mass margin, and propellant margins to reach a conservative "predicted mass." To start, MGAs are selected according to the most conservative category in ANSI/AIAA S-120A-2015 *Mass Properties Control for Space Systems* [3]. The relevant categories and the selected values have been summarized in Table 2.4. In certain cases, the categories published in the ANSI/AIAA guide and those in the MEL do not perfectly match, in which case the the most relevant category is used. For example, the "Electrical/Electronic Components" category is used for "Command Data Handling" and "Telecom," while "Propulsion" is used for both "PPU" and "Thrusters and Tank." The total basic mass (the sum of all subsystem masses without MGA) did not itself receive a growth allowance because the ANSI/AIAA guide did not specify one.

Overall mass margin is set at 30% and calculated based on the basic mass: the sum of the subsystem masses without margin. This was selected simply as a conservative number that is somewhat greater than values seen in the literature [92]. In Chapter 3, propellant margin is set at 5%. An RCS margin of 20% is used for any spacecraft equipped with such a system, which results in the 80% usage described in Subsection 2.2.5.

2.3.4 Solar Sail Mass Estimate

As a still immature technology, mass estimates for solar sails of various sizes are challenging to calculate with any certainty. As a result, an approach that does not require a specific value to be defined is taken wherever possible. However, it is nevertheless beneficial to provide context based on the a reasonable estimate of current sail technology. While rough mass estimates were provided in the literature review, this section will attempt to extrapolate from the current state-of-the-art solar sail—Solar Cruiser—to sails of different sizes.

Solar Cruiser was a $1653\,\mathrm{m}^2$ sailcraft designed for a heliophysics mission [93]. While it was not selected for further funding and thus will not be flown, significant engineering and manufacturing work was already completed and it may be treated as a reasonable baseline. As with all solar sails, the subsystem mass may be broken down into three large categories: the sail "cloth," the structure, and the ancillary systems, such as the deployment mechanism.

Table 2.2: SMART-1 using Published Methodology of Subsection 2.3.1

Subsystem	Mass (kg)	Notes
Tank	8.2	As per Eq. 2.36
Thruster/SEP	20.7	As per Eq. 2.37. Assume 0.09 N of thrust, a specific impulse of 1640 sec, and an electric efficiency of 70%
Thruster/Gimbal	2.1	As per Eq. 2.38
Solar Array	50.7	Flight value from [2]
Solar Sail	0.0	Not equipped
Radiators	15.9	Assumes maximum power generation as excess
Payload	18.9	Flight value from [2]
Dry Mass	116.4	
Propellant	82.0	Flight value from [2]
Total Wet Mass	198.4	

Table 2.3: SMART-1 Mass Budget [2]

Subsystem	Flight Mass (kg)
Attitude and Orbital Control System (AOCS)	19.3
System Unit	15.0
Mechanisms	19.9
Power	45.6
Solar Array	50.7
Hydrazine System	12.5
Telemetry, Tracking, and Command (TT&C)	7.9
Structure	49.1
Thermal Control	12.2
EP S/S (PPS-1350)	29.2
Payload	18.9
Dry Mass	280.3
Hydrazine Propellant	4.6
Xenon Propellant	82.0
Total Wet Mass	366.9

Table 2.4: E1 "Estimated" Level Maturity Growth Allowances [3]. Note that irrelevant categories have been excluded and that certain categories shown here encompass multiple subsystems included in the MELs.

Subsystem	Recommended Mass Growth Allowance (%)	Selected Allowance (%)
Structure	18-25	20
Solar Array	20-35	25
Electrical/Electronic Components	10-35	20
Batteries	20-25	20
Thermal Control	30-50	30
Wire Harness	50-100	60
Propulsion	15-25	20
Instrumentation	25-75	40

Based on basic structural analysis and known information of the materials used, it is possible to scale the first two categories to any size. The final category is treated as a constant due to a lack of necessary information from which to extrapolate. Current sails are proprietary designs owned by the companies contracted to develop them and the mass of specific components is, unfortunately, not available.

The most straightforward subcomponent to estimate is the sail cloth. Composed of a 2.5×10^{-6} m thick CP-1 film with a vapor deposited aluminum (VDA) coating [94], the mass of a sail cloth of an arbitrary size is scaled simply based on the areal densities of these two materials and the desired sail dimensions. Based on a density of $1540\,\mathrm{kg\,m^{-3}}$ for CP-1 [95], the areal density is $3.85 \times 10^{-3}\,\mathrm{kg\,m^{-2}}$. With a thickness of 1000 Å [1], or 1×10^{-7} m, and a density of $2700\,\mathrm{kg\,m^{-3}}$ [21], the VDA layer has an areal density of $2.7 \times 10^{-4}\,\mathrm{kg\,m^{-2}}$. This results in an overall sail cloth areal density of $4.12 \times 10^{-3}\,\mathrm{kg\,m^{-2}}$.

Solar Cruiser, as well as all flown solar sails before it, with the exception of IKAROS, employed Triangular Rollable and Collapsible (TRAC) booms to provide structural support to its sail [1]. Launched as a flat ribbon spooled around a central spindle, these composite booms deploy into a triangular shape in order to withstand compressive and/or bending loads. See Fig. 2.12. To conduct a complete analysis on the strength of these booms, complex finite-element analysis (FEA), detailed schematics, and a full understanding of the loading on the sail would be required. Such details are, unfortunately, largely proprietary and the required analysis is well outside the scope of this dissertation. Fortunately, alternative methods are available. While a gross simplification, the global compression loading is similar to Euler column loading [96]. For a beam supported only at one end, the formula for the critical load P_{cr} at which the beam will buckle is

$$P_{\mathrm{cr}} = \frac{\pi^2 EI}{(2L)^2} \tag{2.43}$$

where E is the Young's Modulus of the beam material, I is the smaller of the cross-section's two area moments of inertia (I_{xx} and I_{yy}), and L is the length of the beam [97].

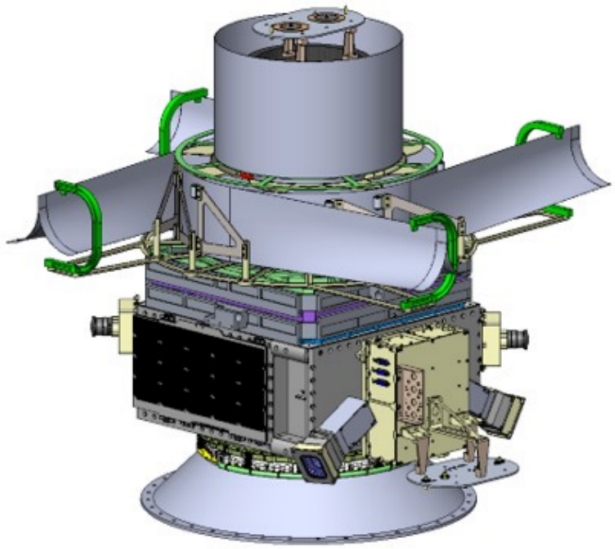

Figure 2.12: Mechanical drawing of the Solar Cruiser sail system showing the central spindle and the unfurling of the TRAC booms [1]

To determine the structural mass of an arbitrarily sized sail, a number of assumptions must be made. First, it is assumed that the loading on the booms scales linearly with increasing sail area A_{sail}. For example, the critical load on a sail twice the size of Solar Cruiser's would need to be twice as large. Second, the overall sail design is that of a square sail supported by four TRAC booms with a length $L = \frac{\sqrt{2}}{2} A_{\text{sail}}$. Finally, the laminate material, and thus the Young's Modulus, is to remain the same as on Solar Cruiser. This only leaves the area moment of inertia to be varied.

While many different TRAC Boom cross-sections have been examined in the literature, it would be impractical to do a multi-variable optimization over all of the various dimensions. Therefore, much as one might vary the gauge of a pipe, only the thickness will be varied in this analysis. The remaining dimensions of the current Solar Cruiser cross section, as shown in Fig. 2.13, will be held constant. In summary, the sail structure will be scaled by solving for the laminate thickness t that satisfies the equation

$$\frac{A_{\text{sail}}}{A_{\text{sail},0}} P_{\text{cr},0} = \frac{\pi^2 E I(t)}{2 A_{\text{sail}}^2} \tag{2.44}$$

where $A_{\text{sail},0}$ and $P_{\text{cr},0}$ are the sail area and loading of Solar Cruiser, respectively.

For the cross-section defined in Fig. 2.13, the lessor of the two area moments of inertia I_{xx} and I_{yy} is always I_{xx} in the range of sail areas and thicknesses being considred here. This is equal to

$$I_{xx} = \frac{2}{3}\left(h_2^3 - h_1^3\right) t + 2\left(\frac{1}{2} h_1^2 \Theta \left(r_2^2 - r_1^2\right) + \frac{2}{3} h_1 \left(r_2^3 - r_1^3\right)(\cos(\Theta) - 1) + \ldots \right. \tag{2.45}$$
$$\left. \frac{1}{8}\left(r_2^4 - r_1^4\right)(\Theta - \sin(\Theta)\cos(\Theta))\right)$$

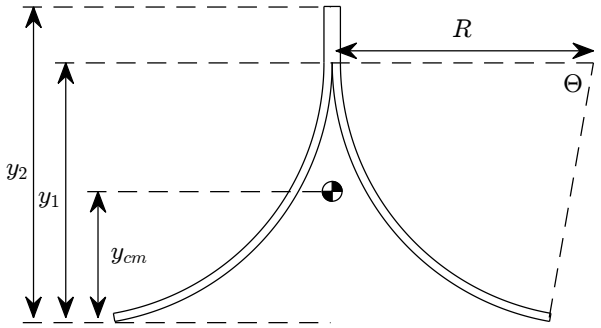

Dimension	Value
y_1	0.0775 m
y_2	0.0945 m
Θ	80 deg
R	0.0787 m
t	0.0025 m

Figure 2.13: TRAC Boom Cross Section and Dimensions

where

$$r_1 = R - \frac{t}{2} \tag{2.46}$$

$$r_2 = R + \frac{t}{2} \tag{2.47}$$

$$h_1 = y_1 - y_{cm} \tag{2.48}$$

$$h_2 = y_2 - y_{cm} \tag{2.49}$$

A full derivation of the equations for I_{xx}, I_{yy}, and the calculation of the location of the centroid y_{cm} may be found in Appendix B.2.

Once a thickness t is solved for a given sail size A_{sail}, the area of the cross-section may be calculated as the sum of a rectangular flange and an arc with a constant thickness. After accounting for symmetry, this is

$$A_{\text{cs}}(t) = 2\left((y_2 - y_1) + R\Theta\right)t \tag{2.50}$$

For a spacecraft with four booms of length L and a laminate material density of ρ, the total structural mass is

$$m_{\text{struct}} = 4A_{\text{cs}}L\rho \tag{2.51}$$

The final part of the solar sail to address is the deployment mechanism and other ancillary systems. Unfortunately, estimating the mass of these systems for an arbitrarily sized sail is all but impossible. As a complex system with numerous components, it can not be simply modeled from first-principles based on known material properties. Further, there is not a large dataset of previous deployer mechanisms from which to base a trend line—be it by sail size or year of development—partially because of the lack of previous sails and partially due to the proprietary nature of the technology. Therefore, it was decided to assume to hold the value for Solar Cruiser as a constant. In reality, it would undoubtedly increase with

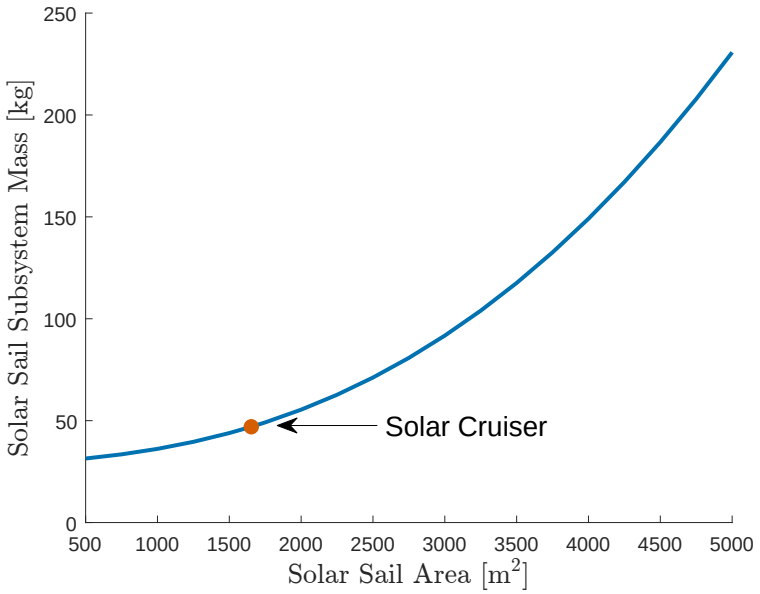

Figure 2.14: Sail Subsystem Mass extrapolated from Solar Cruiser

increasing sail size, but whether it would follow a linear, quadratic, or higher-order trend is unknown.

To find the value for Solar Cruiser, estimates of the structural and sail cloth masses were subtracted from the total subsystem mass. The total subsystem mass is known to be 47 kg [98]. Based on the calculated areal density of $4.12 \times 10^{-3}\,\mathrm{kg\,m^{-2}}$ and an area of $1653\,\mathrm{m^2}$, the sail cloth mass is 6.81 kg. Finally, the with a calculated cross-sectional area of $6.40 \times 10^{-5}\,\mathrm{m^2}$, an individual boom length of 28.75 m, and a laminate material density of $1550\,\mathrm{kg\,m^{-3}}$, the mass of a single boom is estimated to be 2.85 kg. With four booms on a single spacecraft, the total structural mass for the sail becomes 11.41 kg. Subtracting these values from the total mass, the deployer and ancillary systems mass is estimated to be 28.79 kg. This represents over half of the total and is a value whose scaling should therefore be explored further in the future.

Using the described model, area is swept between $500\,\mathrm{m^2}$ and $5000\,\mathrm{m^2}$. The resulting mass estimates are plotted in Fig. 2.14. It is immediately clear that mass increases quadratically with linearly increasing area. Since thrust level directly corresponds to area, this would result in sail acceleration falling due to Newton's Third Law as the subsystem is scaled up. With the deployment mechanism mass being held constant and the sail cloth mass increasingly linearly, it may be determined that this trend is due to the structural mass. There is some evidence for this in the literature. For the proposed $7000\,\mathrm{m^2}$ High Inclination Solar Mission, Koabayashi et al. suggests a 1 rpm spin rate to "allow centrifugal force to augment the stiffness" of the solar sail structure [99]. This is claimed to permit a subsystem mass of 52 kg – hundreds less than the Critical Load estimate would suggest. However, it is also recognized that this would create difficulties for both maintaining attitude control and collecting scientific observations. Significant work will therefore be needed in the future if solar sails are to reach the large sizes and low masses that are desired.

2.4 Orbital Mechanics

Due to the lack of complex, multi-body orbits being considered in this work, only two-body, Sun-centered orbital mechanics are employed. The acceleration due to the two propulsion systems is added to the acceleration vector of the spacecraft in the Sun-centered inertial frame using the directional unit vectors of the sail normal $\hat{\mathbf{n}}$ and tangential $\hat{\mathbf{t}}$. The sail normal is equivalent to the longitudinal axis of the spacecraft. Having fixed the SEP thruster to the same axis, its acceleration is also applied in the sail normal direction.

$$\ddot{\mathbf{r}}_{\mathrm{S,s/c}} = -\frac{\mu}{r_{\mathrm{S,s/c}}^3}\mathbf{r}_{\mathrm{S,s/c}} + \frac{1}{m}\left(F_{\mathrm{n}}\hat{\mathbf{n}} + F_{\mathrm{t}}\hat{\mathbf{t}}\right) + a_{\mathrm{SEP}}\hat{\mathbf{n}} \tag{2.52}$$

In Chapter 3, gravity assists will be utilized. Rather than completing the hand off from Sun-centered to planet-centered two-body mechanics, a zero sphere-of-influence model is used in which feasibility is ensured in the Sun-centered frame through the use of trajectory constraints. Having selected the desired gravity-assist sequence beforehand, a trajectory-phase interface is placed at the appropriate planet. This results in two control points being located at the planet which correspond to a half-length inbound and outbound shooting arc. This allows for the change in the trajectory between the inbound and outbound legs that results from the gravity assist may be constrained according to physics and desired safety margins.

As the result of gravity assist, while the direction of the velocity vector with respect to the planet $\mathbf{v}_{\infty,i}$ may change, the inbound and outbound velocity magnitudes $v_{\infty,1}$ and $v_{\infty,2}$ may not. This is the first requirement that must be enforced.

$$\mathbf{v}_{\infty,1} \neq \mathbf{v}_{\infty,2} \quad v_{\infty,1} = v_{\infty,2} \tag{2.53}$$

As it leaves the sphere of influence of the chosen planet, the spacecraft's outgoing heliocentric velocity $\mathbf{v}_2$ is defined as

$$\mathbf{v}_2 = \mathbf{v}_{\infty,2} + \mathbf{v}_p \tag{2.54}$$

where $\mathbf{v}_{\mathrm{p}}$ is the velocity of the planet.

The difference in magnitude of the heliocentric velocity before and after a gravity assist v_1 and v_2 is determined by the turning angle Φ, or the change in direction between the two vectors.

$$\Phi = \arccos\left(\frac{\mathbf{v}_{\infty,1}\cdot\mathbf{v}_{\infty,2}}{v_{\infty,1}v_{\infty,2}}\right) \tag{2.55}$$

The upper limit on this value is a function of the periapsis height r_π of the flyby (with respect to the planet), with lower flybys providing greater turning angles and larger changes in velocity. However, to ensure the safety of the spacecraft, this must be placed high enough to avoid the surface and/or atmosphere of a planet and any regions of high radiation exposure. The second constraint on the gravity assist is therefore that the turning angle must be less than the maximum angle which occurs at the minimum safe altitude h above the planet's radius r_{p}. The resulting feasibility constraint is

$$-\frac{\mu_p}{v_{\infty,1}^2}\left(\frac{1}{\sin\left(\Phi/2\right)}-1\right)+\left(r_{\mathrm{p}}+h\right)\leq 0 \tag{2.56}$$

A more complete discussion on this topic may be found in Schaub and Junkins [100], Vallado [101], or any other standard text.

Chapter 3

Heliophysics

In this chapter, HLTP is assessed for its ability to provide a net advantage in terms of delivered mass to a circular orbit with a radius of 1 au and an inclination of 90 deg. This is conducted using two representative spacecraft equipped with either a hall effect or gridded ion thruster, with each being tested at their basic and predicted mass. By sweeping over sail subsystem areal density, the breakeven performance at which a net mass advantage is achieved is determined for each case. Based on the current state of the art defined in the previous chapter, conclusions are then be made regarding the potential benefits of this technology and its suitability for this particular application.

3.1 Motivation

Polar orbits of the Sun have been a popular subject in the solar sailing literature for many years. One of the most well known is the Solar Power Imager (SPI) mission proposal, which first appeared in the mid-2000s [60, 102] and made a reappearance in 2020 [103]. The European Space Agency also had an equivalent concept, the Solar Polar Orbiter (SPO), in 2006 [104]. More recently, the team behind Solar Cruiser proposed the High-Inclination Solar Mission (HISM) in 2020 [99]. All of these share the same underlying strategy: to complete expensive maneuvers close to the Sun where solar radiation pressure is at its strongest. After departing from the Earth, these spacecraft would spiral in towards the Sun to distances as close a 0.22 au – the calculated melting point of a CP-1 solar sail – and then crank the orbit to the desired 90 deg inclination. At such a distance, the solar sail would have over 20 times the acceleration that it would have had at Earth. Upon reaching the desired inclination, the spacecraft would spiral back out to a circular orbit to conduct long-term observation of the Sun's polar regions.

The issue with these concepts is one of technological readiness. With the largest successful solar sail only 400 m^2 [22] and later attempts at more ambitious sails having either failed on orbit [27] or been canceled during development [34, 29], large, high-performance solar sails have remained elusive. Unfortunately, to enable the proposed mission concepts, solar sails one or two orders of magnitude larger than those successfully demonstrated would need to be designed. See Table 3.1 for context. Based on the historical rate of development, the creation of these solar sails may be expected to require a significant period of time for design

Table 3.1: A Limited Comparison of Previous and Proposed Solar Sails

Mission	Sail Size (m^2)	Vehicle Mass (kg)	Outcome	Ref.
IKAROS	200	307	Successful	[32, 22]
NanoSail-D2	10	4	Successful	[31]
Sunjammer	1200	45	Canceled	[33, 34]
LightSail 1 & 2	32	5	Successful	[30, 26, 35]
NEA Scout	85	14 ‘	Unknown Failure	[36]
Solar Cruiser	1653	100	Canceled	[28]
Solar Polar Imager	25600	450	Proposed (2006)	[102]
Solar Polar Orbiter	23409	532	Proposed (2006)	[104]
HISM	7000	293	Proposed (2020)	[99]

and construction. Meanwhile, as shall be shown in this chapter, a traditionally constructed SEP spacecraft could achieve the desired orbit using a gravity assist sequence. Therefore, to maintain buy in from the solar sailing community while also avoiding the development of the largest proposed sails, this chapter considers an HLTP alternative by adding an auxiliary solar sail to a SEP-spacecraft flying a gravity assist trajectory.

3.2 Application Methodology

In this section, the methodology specific to this chapter will be explained. First, the four different spacecraft configurations to be used will be defined. Next, the baseline SEP-only trajectories against which HLTP will be compared are optimized. Finally, the trade study workflow used to assess performance of this hybrid spacecraft will be explained.

3.2.1 Spacecraft Master Equipment Lists

Before conducting a trade study on solar sail subsystem performance, four baseline SEP spacecraft are defined. First, the propulsion requirements must be set, for these will partially determine the sizing of numerous other systems. As a representative hall thruster option, an Aerojet Rocketdyne XR-5 thruster is selected [105]. A commercialized version of the NASA Evolutionary Xenon Thruster (NEXT-C), also constructed by Aeroject Rocketdyne, is similarly chosen as a gridded ion alternative [106]. Each spacecraft is equipped with two identical thrusters and power processing units (PPUs), the masses of which may be found in published documentation [107, 105].

The masses of the command and data handling, communications, thermal control, and attitude control system are all set based on mission studies that feature the requirements of (1) a small sat spacecraft and (2) a trajectory that brings the spacecraft to the outer planets. For this purpose, the MELs for the Jupiter Magnetospheric Boundary Explorer (JUMPER) mission proposal [108] and a Discovery-class reference study to Saturn by Sunada et al. [109] are used. Instrumentation is set to a lightweight value of 25 kg, which rises to 35 kg with growth allowance.

While neither a link budget nor a full power budget are considered to be within the scope of this work, a bus power requirement that is reasonable for meeting communications, thermal, and general operation requirements must be defined. Based on input from a knowledgeable collaborator, this is set to 500 W [110]. This results in a minimum solar array sizing of 13.52 kW to ensure full bus power during the Jupiter flyby. With no significant eclipse periods expected, the spacecraft is equipped with 1200 W h of batteries to provide 10 h of full-power operations or longer periods on reduced power.

Due to the mission-specific design of most spacecraft, it is difficult to define a specific value for the harness, structure, and tank masses. Tank mass, for example, is determined by the propellant requirements of a particular trajectory; two otherwise identical spacecraft flying different trajectories to the same target orbit may have entirely different tank masses. The harness, structure, and tank masses are therefore set not based on previously published MELs but instead using proportional values calculated using guidelines in SMAD [111]. Structural mass is set to 15% of the basic dry mass, harness mass is 17% of the total of all power-related systems, and the tank mass is equal to 7.5% of the propellant mass contained within it.

To determine the propellant and solar array masses, a coarse trade study of solar array size is conducted while leaving propellant mass free. By optimizing for propellant mass, the optimal solar array size and subsystem mass is determined. This results in both spacecraft being equipped with 13.52 kW solar arrays – the minimum possible – which indicates that minimizing vehicle mass is more beneficial than maximizing the region in which full SEP thrust is available. With the baseline propellant mass set, the resulting tank mass is found. This process is repeated for the basic mass configurations as well. In these cases, the mass of these proportional systems (structure, harness, and tank) and the propellant are all updated, while the other fixed-mass systems are not. The MELs for the four defined spacecraft are provided as Tables 3.2-3.5.

3.2.2 Baseline Trajectories

The trajectories flown by these SEP-only spacecraft define the baseline performance that could be flown with current technology. Four such trajectories are optimized to correspond with the four configurations and the eventual four trade studies to be conducted: XR-5 at predicted mass, XR-5 at basic mass, NEXT-C at predicted mass, and NEXT-C at basic mass. Recall that the basic and predicted masses are the minimum and maximum possible spacecraft masses, respectively. The timeline and overall flight time of each trajectory is outlined in Table 3.6. Due to the geometry of the problem being fixed by the pre-selected Jupiter-Earth-Earth gravity assist sequence, the dates of major mission events are quite similar across all four cases.

The four baseline trajectories are shown in Fig. 3.1. By the nature of their shared geometry, common features are shared among all four. In each, the spacecraft flies a largely ballistic trajectory from the Earth to Jupiter before undergoing a large gravity assist maneuver to increase its inclination. It then flies another mostly ballistic arc back to Earth before completing another gravity assist to further increase its inclination. A three-year Earth-resonance orbit is then flown to enable a final inclination change gravity assist. The SEP system is primarily used to circularize the orbit, with it firing principally at and around

Table 3.2: XR-5 Hall Effect MEL (13.52 kW array, 500 W bus) at Predicted Mass

Subsystem	Basic Mass (kg)	Growth Allowance	Predicted Mass (kg)	Notes and References
Structural	66	20%	79.2	Set to 15% of Basic Dry Mass [111]
Solar Arrays	135	25%	168.8	Assume $100\,\mathrm{W\,kg^{-1}} = 10\,\mathrm{kg\,kW^{-1}}$. Full bus power to Jupiter.
Batteries	10	20%	12.0	1200 W h total of primary and backup batteries at $120\,\mathrm{W\,h\,kg^{-1}}$
Command and Data Handling	5	20%	6.0	Based on JUMPER [108]
Telecom	33	20%	39.6	Sunada [109] ∼33 kg
Thermal	10	30%	13.0	Based on Sunada [109]
ADCS	25	30%	32.5	Based on Sunada [109]. Assumes no Reflectivity Control Devices (RCDs).
Harness and Electronics	30	60%	48.0	17% of Power System Total [111]
PPU	37	20%	44.4	2 PPUs: 1 primary and 1 backup. 18.6 kg per PPU [107]
Thrusters and Tank	66	20%	79.2	2 thrusters: 1 primary and 1 backup. 12.3 kg per thruster [105]. Tank set to 7.5% of Prop. Mass
Instrumentation	25	40%	35.0	
Dry Mass	442		557.7	
Margin		30%	132.6	Per AIAA S-120A-2015 [112]
Allocated Dry Mass			690.3	
Propellant Mass			546.0	Includes 5% Margin requirement. Actual propellant mass is an optimized variable.
RCS Mass			19.0	1.5% of wet mass, includes 20% margin
Wet Total Mass			1255.3	

Table 3.3: NEXT-C Gridded Ion MEL (13.52 kW array, 500 W bus) at Predicted Mass

Subsystem	Basic Mass (kg)	Growth Allowance	Predicted Mass (kg)	Notes and References
Structural	68	20%	81.6	Set to 15% of Basic Dry Mass [111]
Solar Arrays	135	25%	168.8	Assume $100\,\mathrm{W\,kg^{-1}} = 10\,\mathrm{kg\,kW^{-1}}$. Full bus power to Jupiter.
Batteries	10	20%	12.0	1200 W h total of primary and backup batteries at $120\,\mathrm{W\,h\,kg^{-1}}$
Command and Data Handling	5	20%	6.0	Based on JUMPER [108]
Telecom	33	20%	39.6	Sunada [109] ∼33 kg
Thermal	10	30%	13.0	Based on Sunada [109]
ADCS	25	30%	32.5	Based on Sunada [109]. Assumes no Reflectivity Control Devices (RCDs).
Harness and Electronics	30	60%	48.0	17% of Power System Total [111]
PPU	69	20%	82.8	2 PPUs: 1 primary and 1 backup. 34.5 kg per PPU [107]
Thrusters and Tank	42	20%	50.4	2 thrusters: 1 primary and 1 backup. 14.0 kg per thruster [105]. Tank set to 7.5% of Prop. Mass
Instrumentation	25	40%	35.0	
Dry Mass	452		569.7	
Margin		30%	135.6	Per AIAA S-120A-2015 [112]
Allocated Dry Mass			705.3	
Propellant Mass			178.5	Includes 5% Margin requirement. Actual propellant mass is an optimized variable.
RCS Mass			13.0	1.5% of wet mass, includes 20% margin
Wet Total Mass			896.8	

Table 3.4: XR-5 Hall Effect MEL (13.52 kW array, 500 W bus) at Basic Mass

Subsystem	Basic Mass (kg)	Growth Allowance	Predicted Mass (kg)	Notes and References
Structural	62	0%	62	Set to 15% of Basic Dry Mass [111]
Thrusters and Tank	42	0%	42	2 thrusters: 1 primary and 1 backup. 12.3 kg per thruster [105]. Tank set to 7.5% of Prop. Mass
All Other Systems	310	0%	310	Unchanged from Table 3.3
Dry Mass	414		414	
Margin		0%	0	
Allocated Dry Mass			414	
Propellant Mass			215	No Margin requirement. Actual propellant mass is an optimized variable.
RCS Mass			10	1.5% of wet mass
Wet Total Mass			639	

Table 3.5: NEXT-C Gridded Ion MEL (13.52 kW array, 500 W bus) at Basic Mass

Subsystem	Basic Mass (kg)	Growth Allowance	Predicted Mass (kg)	Notes and References
Structural	67	0%	67	Set to 15% of Basic Dry Mass [111]
Thrusters and Tank	36	0%	36	2 thrusters: 1 primary and 1 backup. 14.0 kg per thruster [105]. Tank set to 7.5% of Prop. Mass
All Other Systems	342	0%	342	Unchanged from Table 3.3
Dry Mass	445		445	
Margin		0%	0	
Allocated Dry Mass			445	
Propellant Mass			91	No Margin requirement. Actual propellant mass is an optimized variable.
RCS Mass			8	1.5% of wet mass
Wet Total Mass			544	

Table 3.6: Major Event Dates for Baseline Trajectories

Event	XR-5 Baselines		NEXT-C Baselines	
	Predicted Mass	Basic Mass	Predicted Mass	Basic Mass
Launch	March 9, 2032	February 29, 2032	March 4, 2032	February 28, 2032
Jupiter GA	July 7, 2033	June 28, 2033	July 2, 2033	June 27, 2033
Earth GA 1	February 18, 2036	February 17, 2036	February 18, 2036	February 16, 2036
Earth GA 2	February 18, 2039	February 16, 2039	February 17, 2039	February 15, 2039
Final Orbit	September 10, 2040	August 29, 2040	August 11, 2040	September 16, 2040
Total Flight Time	3106.8 d	3103.7 d	3082.1 d	3122.6 d

the various perihelia. This is also the point in the mission at which the available power is highest and full thrust may be used. The various red SEP vectors represent the acceleration produced by that system at each control point. In later figures, black sail acceleration vector will also be included. Importantly, there is no requirement for the SEP vectors of these baseline trajectories to point away from the Sun. The impact of the addition of that constrain will be considered in the results.

Differences also exist between the various baseline trajectories. The XR-5 predicted mass case has a thrust arc at the aphelion of its Earth-to-Earth leg, as shown in green in Fig. 3.1a. While the equivalent NEXT-C Predicted Mass configuration also shares this feature, it is shorter. This is likely due to the higher power requirements of the NEXT-C thruster limiting performance at this solar distance. Differences also exist between the predicted and basic mass cases. Both predicted mass trajectories of Figs. 3.1a and 3.1b feature substantial thrust arcs at aphelion of the final, orange leg, while the basic mass cases of Figs. 3.1c and 3.1d do not. This is to be expected, since the performance of the launch vehicle and the acceleration produced by the SEP system are degraded by the higher spacecraft masses. In general, however, the trajectories are all more similar than they are different. This proves beneficial when creating a strategy for the trade study, as outlined in the following subsection.

3.2.3 Trade Study Design

To determine the sail subsystem performance necessary to achieve a net advantage in terms of delivered mass, trajectories are generated while sweeping over sail area and sail subsystem mass. Four trade studies are completed in this manner to match the four baseline trajectories: XR-5 predicted mass, XR-5 basic mass, NEXT-C predicted mass, and NEXT-C basic mass. The upper bounds for each trade study are set to a maximum sail size of $8000\,\mathrm{m}^2$ and a mass of $100\,\mathrm{kg}$. The former is chosen to encompass the smallest of the next-generation proposed sails (the HISM), while the latter is an experimentally determined value deemed to be a reasonable maximum based on the region of positive results in the design space. The trajectory result at each point in the mesh is compared against the appropriate baseline trajectory to determine the change in vehicle mass.

For each trade study, the associated spacecraft MEL is included in the optimization process to dynamically constrain the dry mass of the spacecraft. As the more advantageous regions of the sail design space are explored, larger portions of the mission's ΔV requirements are offloaded from the propellant-consuming SEP system to the propellantless sail. This in turn reduces the propellant mass, tank mass, and structural mass requirements of the spacecraft, which improves the acceleration generated by the sail and further reduces the propellant needed for the SEP system. This positive feedback loop allows for the advantages of a hybrid low-thrust propulsion system to be maximized. It should be noted, however, that in the less advantageous portions of the design space, a negative feedback loop will result.

To ensure a reasonable run time, each trade study is conducted using the Worker-Leader parallelization scheme outlined in Subsection 2.1.5. For each experiment, 1 leader node and 7 worker nodes are requested from the MIT Supercloud, with each worker node using 20 of the 48 available cores. The remaining CPUs cannot be utilized due to the startup memory requirements of MATLAB's *parpool* parallelization command exceeding the memory available on each node. A mesh with $20\,\mathrm{kg}$ and $200\,\mathrm{m}^2$ increments is defined to ensure that

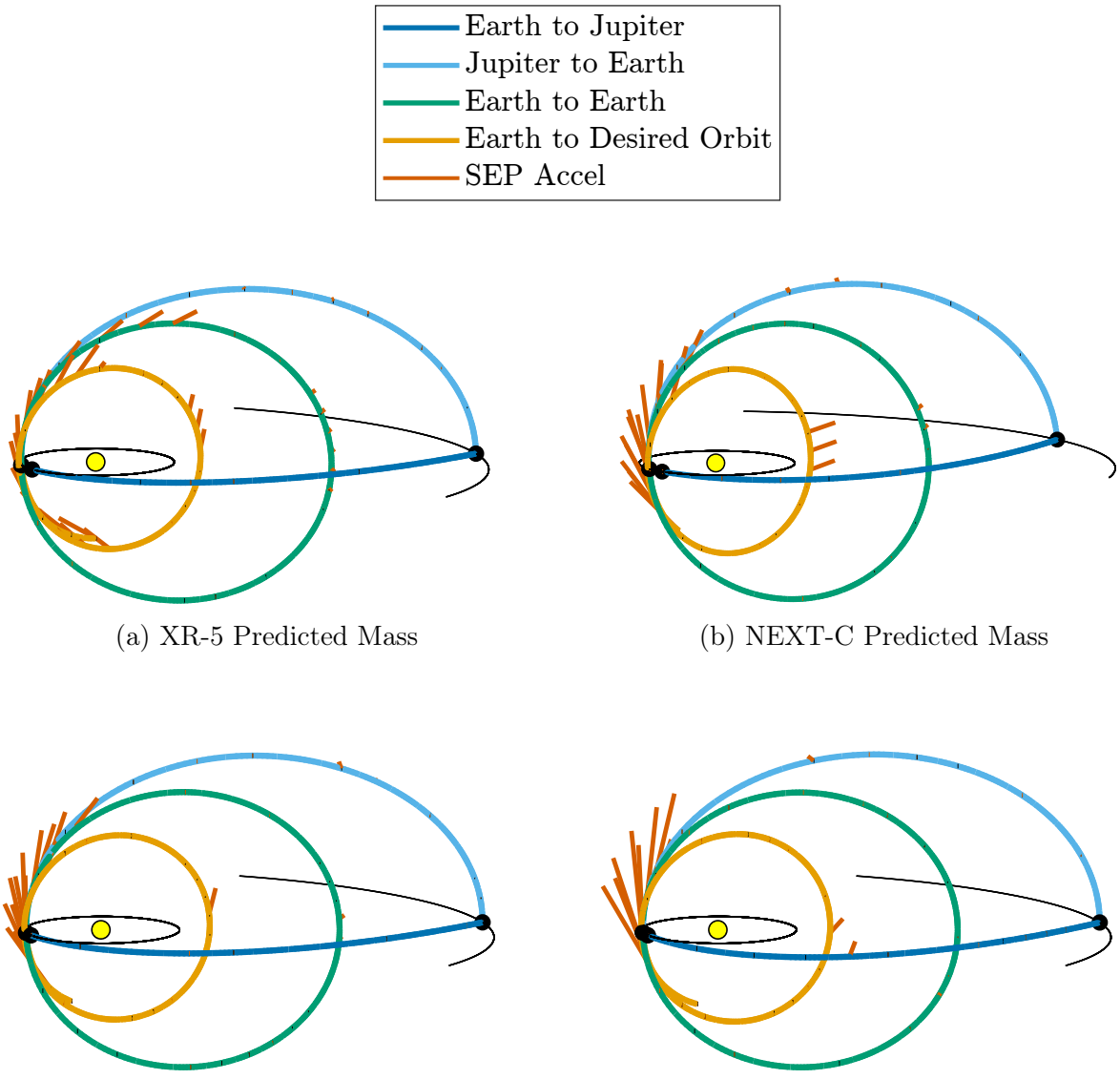

(a) XR-5 Predicted Mass

(b) NEXT-C Predicted Mass

(c) XR-5 Basic Mass

(d) NEXT-C Basic Mass

Figure 3.1: SEP-only Baseline Trajectories

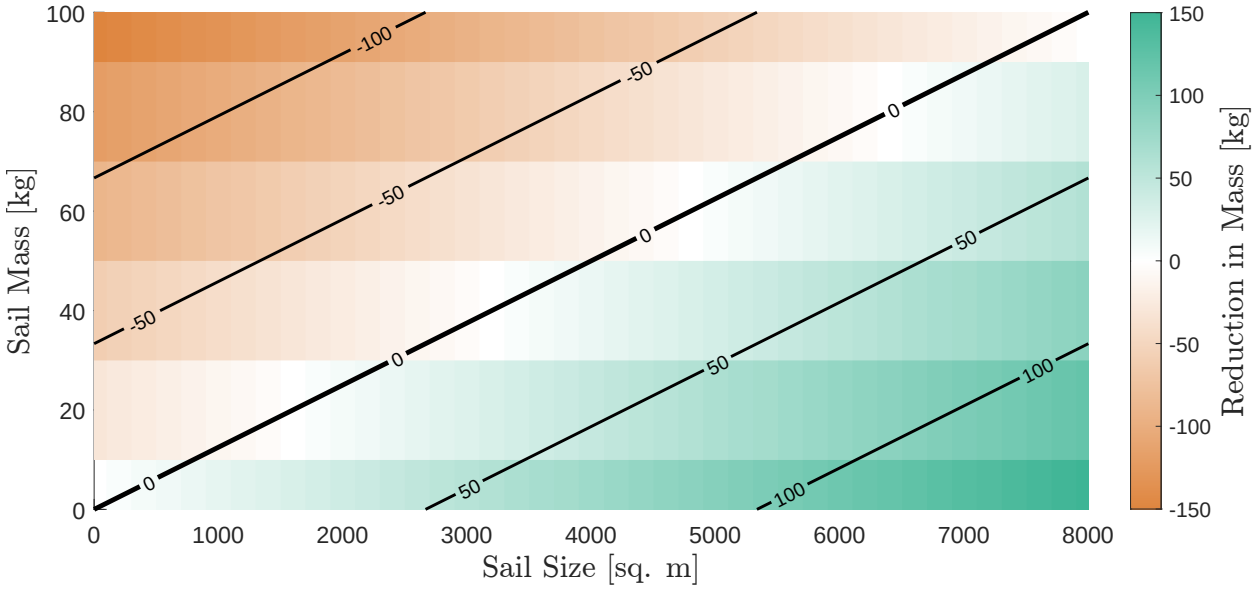

Figure 3.2: Idealized Trade Study Contour Plot

each experiment is completed in less than the maximum run-time limit of four days on the supercomputer. After the automated trade study is completed, a human-in-the-loop cleanup is conducted in which outliers and failed points are eliminated by manually selecting initial guesses and reoptimizing specific mesh points.

An idealized set of example results are used to produce the contour plot shown in Fig. 3.2. Along the x-axis, sail size, and thus the reduction in spacecraft mass, increases. Sail subsystem mass increases on the y-axis, with the spacecraft mass following as a result. In the limit, the mesh entries closest to the x-axis represent the boundary case of a massless solar sail, while those along the y-axis are for a solar sail of zero area. These are the best and worst results of the trade study.

Contour lines are calculated and overlayed to help indicate the positive and negative regions of the design space. It is plainly apparent that the design space is separated into two regions by a diagonal breakeven line. The upper triangular portion contains the region in which spacecraft mass increases as a result of adding an auxiliary sail, while the lower triangular section contains those trajectories with a net decrease in spacecraft mass. Bolded in black, the breakeven contour that separates them indicates the minimum sail subsystem performance needed for HLTP to provide the desired net mass benefit. If the contour line is linear and approximately intersects the origin, than its slope measures the mass per unit area, or areal density σ_{sail}, that is required. Steeper contour lines are considered more desirable, for they indicate higher, more achievable areal densities.

3.3 Results

The four resulting contour plots are provided as Figs. 3.3-3.6. Starting with the XR-5 predicted mass trade study of Fig. 3.3, the breakeven contour may be seen to approximately intersect the origin. This indicates that, for this trajectory, there is no inherent inefficiency

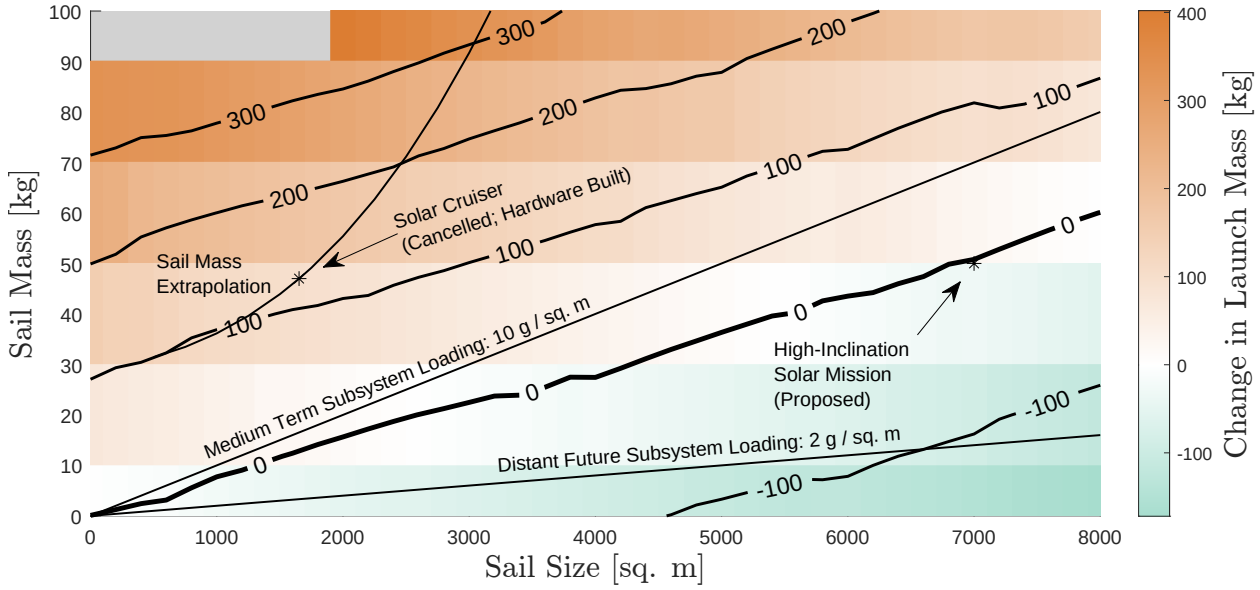

Figure 3.3: XR-5 Predicted Mass Trade Study Contour

created by the pointing constraint to keep the reflective side of the sail facing the Sun. Since the trajectory solution at the origin uses a sail of zero mass and zero size, the only difference between the SEP baseline and the sail solution at the origin is this requirement. If the optimal SEP trajectory had included thrust towards the Sun, a small mass penalty would have been expected and the breakeven contour would not have intersected the origin.

In the lower right portion of the design space, where sail performance is at its highest, a substantial reduction ($>$ 170 kg) of launch mass is discovered. However, in the more achievable upper left region, Solar Cruiser and sails based on it all lead to a net increase in overall spacecraft mass. In contrast, the sail of the High-Inclination Solar Mission is almost exactly on the breakeven contour. In the most extreme portion of the design space, where sail performance is worse than the current state of the art, the negative feedback loop of increasing propellant and structural mass eventually causes the optimizer to not converge. These solutions are grayed out and carry mass penalties of approximately 400 kg – an increase of over 30%. The contours may also be seen to tighten as the mass increases from the bottom right to the top left. It is easier to add mass to this spacecraft than it is to remove it.

The effect of this feedback loop is less prominent in the XR-5 basic mass contour plot shown in Fig. 3.4. Both the maximum improvement and deterioration in launch mass is reduced in absolute terms (i.e. in kilograms). However, as will be discussed further in the following subsection, the proportional benefits in terms of mass fractions are greater at this lower overall mass. The colors of this contour plot and all subsequent plots are less saturated than those in Fig. 3.3. This is because a consistent colorbar scale is used throughout and, being the heaviest configuration of the least efficient thruster, the potential change in mass is greatest in that first figure. Interestingly, while the breakeven contour is almost identical to the predicted mass case – notice the position of the HISM sail on both Figs. 3.3 and 3.4 – the contours in the basic mass trade study are more equally spaced. The feedback loop may be weaker or simply more linear at this lower dry mass.

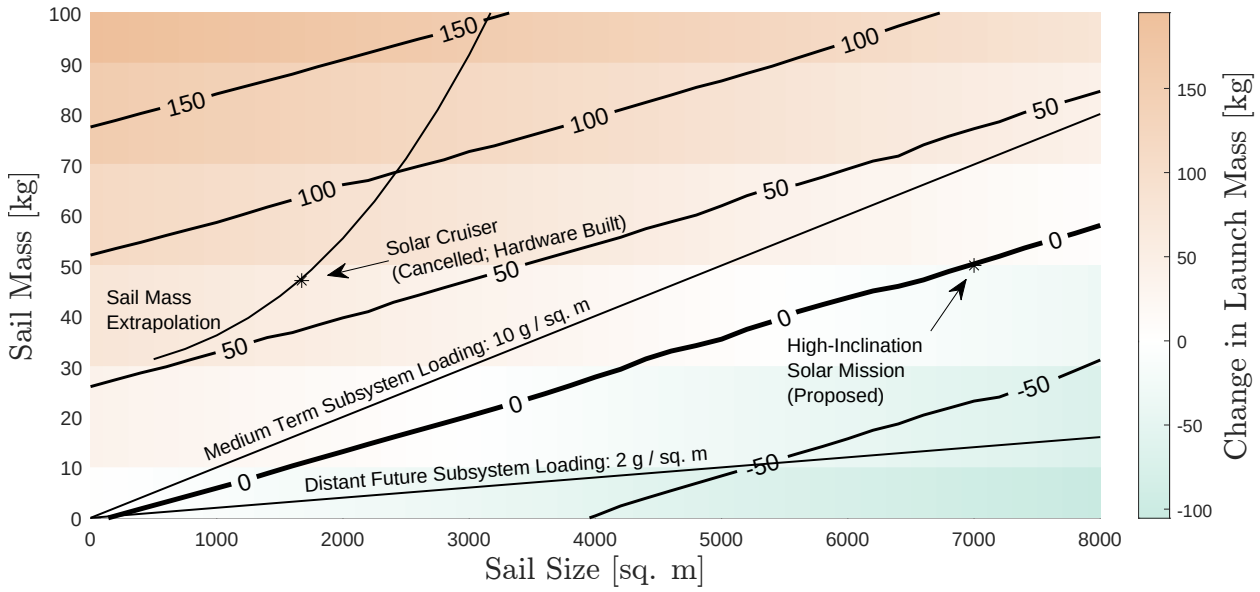

Figure 3.4: XR-5 Basic Mass Trade Study Contour

The predicted and basic mass NEXT-C cases are shown in Figs. 3.5 and 3.6, respectively. Compared to the two equivalent XR-5 cases, the change in mass is greatly reduced, with a maximum improvement of 54 kg and 47 kg, compared with the XR-5's 172 kg and 105 kg. The difference between the NEXT-C predicted and basic mass cases is also much smaller than between the XR-5 cases. While both NEXT-C trade studies show only a small inherent penalty – the zero-mass contour nearly goes through the origin – the contours are very shallow, which indicates lower sail areal densities and higher performance requirements. As a result, neither the current nor the next generation sails are able to breakeven.

3.4 Discussion

To estimate the minimum subsystem areal density needed to achieve a new mass benefit, the approximately linear slope is extracted from each contour plot's breakeven line using a linear fit. Calculated using MATLAB's Curve Fitting Toolbox, the R^2 value of each of these models is above 0.99. However, as stated previously, for this breakeven areal density to be universally true at all sail sizes, it would be need to intersect the origin. In actuality, all of the fits intercept the x-axis at some offset. These areal densities and the x-intercepts are summarized in Table 3.7.

For those contours with a positive x-intercept, the breakeven contour intersects the x-axis at a positive sail size. In theory, this indicates that a non-zero sized solar sail is required to match the SEP baseline and that HLTP has some inherent inefficiency on this trajectory. Those with a negative intercept benefited from the addition of this constraint, which implies that the SEP solution was sub-optimal because a SEP spacecraft can fly a trajectory that satisfies the sail pointing constraint. In reality, all of the intercepts are very close to zero ($\leq 200\,\mathrm{m}^2$) and could simply be numerical noise. These small displacements from the origin may therefore be safely neglected.

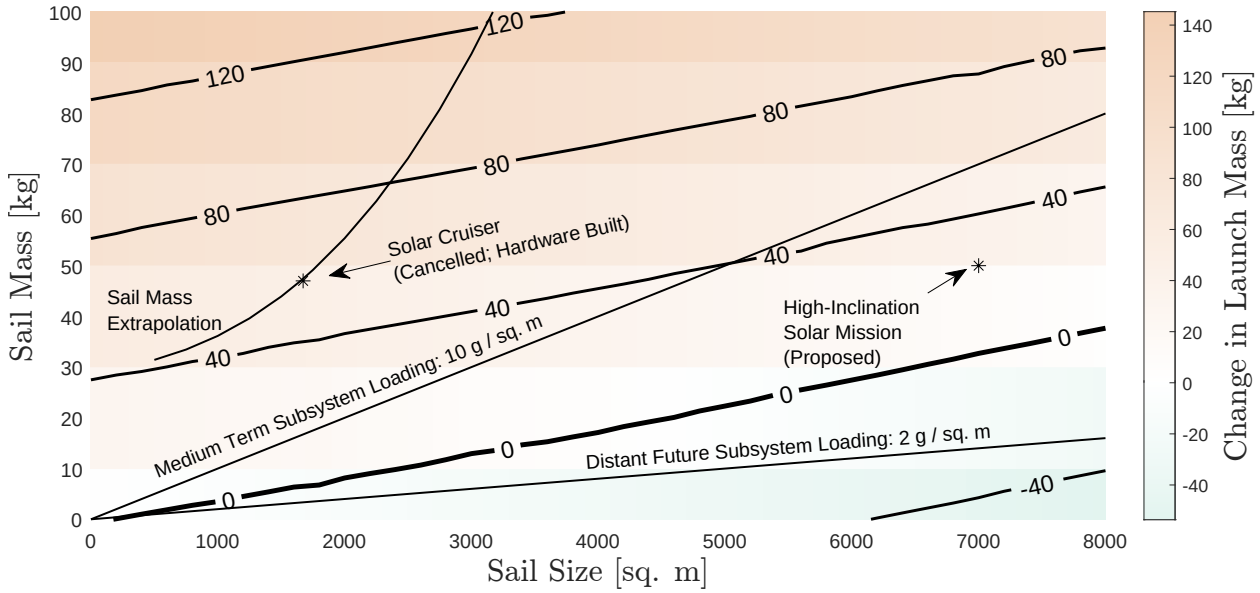

Figure 3.5: NEXT-C Predicted Mass Trade Study Contour

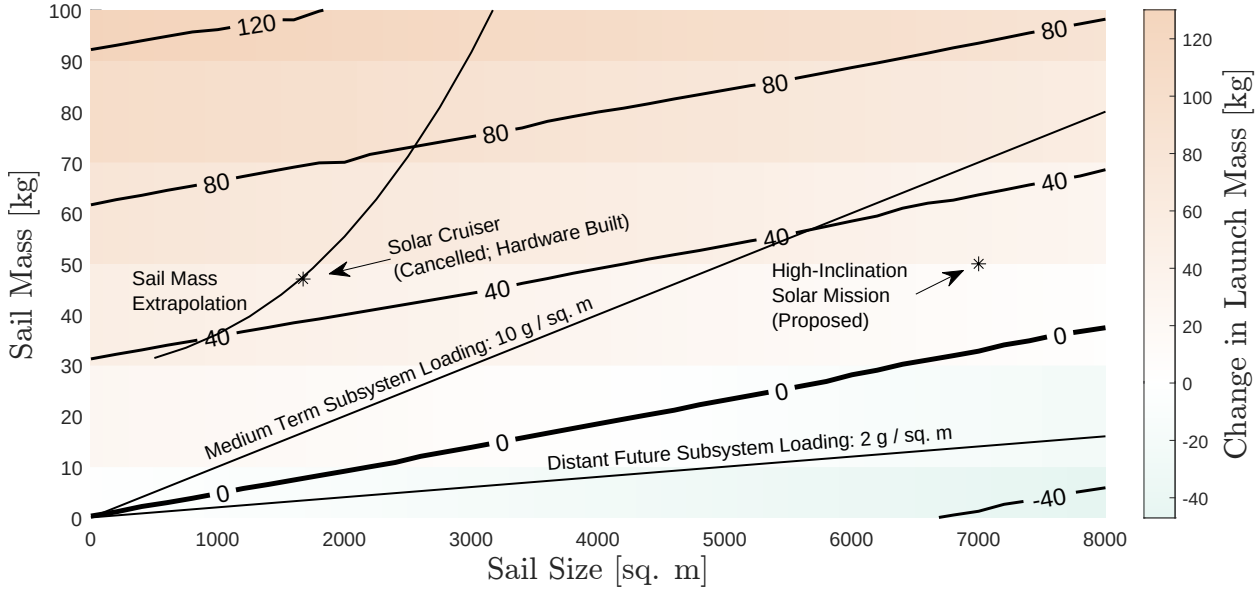

Figure 3.6: NEXT-C Basic Mass Trade Study Contour

Table 3.7: Breakeven Areal Densities and Sail Areas

	XR-5		NEXT-C	
	Predicted Mass	Basic Mass	Predicted Mass	Basic Mass
Areal Density	$7.3\,\mathrm{g\,m^{-2}}$	$7.4\,\mathrm{g\,m^{-2}}$	$4.8\,\mathrm{g\,m^{-2}}$	$4.7\,\mathrm{g\,m^{-2}}$
x-intercept	$0.5\,\mathrm{m^2}$	$102.1\,\mathrm{m^2}$	$-198.5\,\mathrm{m^2}$	$-146.0\,\mathrm{m^2}$

Table 3.8: Change in Mass Fractions

Change in Mass Fraction	XR-5		NEXT-C	
	Predicted Mass	Basic Mass	Predicted Mass	Basic Mass
Propellant $\Delta\frac{m_{\text{prop}}}{m}$	−0.0714	−0.1147	−0.0441	−0.0697
Payload $\Delta\frac{m_{\text{payload}}}{m}$	0.0045	0.0079	0.0027	0.0044

Based on the minimal variation between the breakeven areal density of each thruster's predicted and basic mass cases, the thruster appears to be the driving factor in the required sail performance, rather than the mass of the spacecraft. For the XR-5 configurations to achieve a net mass advantage, an areal density between $7.3\,\mathrm{g\,m^{-2}}$ and $7.4\,\mathrm{g\,m^{-2}}$ was required, while the NEXT-C configurations required $4.7\,\mathrm{g\,m^{-2}}$ to $4.8\,\mathrm{g\,m^{-2}}$. Without a clear pattern of the predicted or basic mass cases having a higher or lower value, the small range in values between them may plausibly be considered noise.

The lack of differentiation between the predicted and basic mass areal densities was an unexpected result. Since the performance of a solar sail is directly proportional to vehicle mass, its fraction of the overall ΔV requirements should be greatest in the lighter, basic mass configurations. To better study the effect of overall vehicle mass, the reduction in propellant mass and increase in payload mass with respect to the overall launch mass is considered. The change in the propellant and payload mass fractions are therefore calculated and compared against the equivalent SEP-only baselines. The values for a massless, $8000\,\mathrm{m^2}$ solar sail, are given in Table 3.8 as the improvement provided by the highest performing sail subsystem contained within the trade study. Two patterns are apparent. First, the proportional benefits of adding a solar sail are, as predicted, greater for the basic mass configurations than for the predicted mass configurations. Second, the benefit to the NEXT-C configurations were approximately half that of the XR-5. With its higher specific impulse and lower propellant requirements, the NEXT-C suffers with respect to the XR-5 in proportional terms in addition to the previously discussed areal density and absolute change in mass.

3.5 Conclusions

In this test of the addition of an auxiliary solar sail to a baseline SEP spacecraft, it was demonstrated that a net mass advantage could be achieved in terms of both launch mass and mass fractions. Based on the bounding case of a massless, $8000\,\mathrm{m^2}$ solar sail, a maximum reduction in launch mass of 172 kg was found for an XR-5-equipped SEP spacecraft. A maximum reduction in propellant mass fraction of 0.1147 and an increase of the payload mass fraction of 0.0079 was also possible. A net mass advantage was found to be possible using a next-generation solar sail, as represented by the HISM proposal.

Due to its lower specific impulse (i.e. propellant mass efficiency), the XR-5 configurations were consistently found to benefit more from the addition of an auxiliary sail than the NEXT-C alternatives. This held true for all three of the considered metrics: change in launch mass, breakeven areal densities, and change in mass fractions. This is due to a combination of interrelated factors. First, the lower specific impulse of the XR-5 resulted in a higher initial

propellant mass that may be reduced. Second, the positive feedback loop caused by offsetting ΔV to the solar sail was stronger due to the combined effect of the lower mass efficiency of the thruster, the tank mass being proportional to the propellant mass, and the structural mass being proportional to the overall vehicle mass. There was simply less to be gained by adding a solar sail to a spacecraft being propelled by an already efficient gridded ion thruster.

Using a linear curve fit to the zero-mass contours of the four conducted trade studies, the sail subsystem areal densities required to breakeven were determined. Areal densities as high as $7.4\,\mathrm{g\,m^{-2}}$ would be able to provide a net mass advantage. However, for a significant benefit to be gained, a higher performance solar sail would be necessary. When considered in the context of the challenges faced by previous attempts to create high-performance solar sails – Solar Cruiser's subsystem would have been $28\,\mathrm{g\,m^{-2}}$ – it is clear that HLTP is unlikely to provide a mass advantage large enough to justify the additional development cost and systems risk in the near-to-medium term future for this mission. It would be more logical to fly the mission as a traditional, SEP-only spacecraft.

Chapter 4

Interstellar Object Flybys

Extrasolar comets and asteroids, otherwise known as interstellar objects (ISOs), rapidly travel through the Solar System at great speed due to their hyperbolic orbits. In this chapter, HLTP is compared against five other propulsion alternatives to gauge its ability to solve this difficult, thrust-limited trajectory problem. With only two ISOs having been discovered thus far, a statistical approach is used based on the expected population of objects. Two datasets of synthetic ISOs are sampled to produce a large dataset of targets against which to evaluate the spacecraft. By optimizing for arrival velocity, the performance of a near-to-medium-term HLTP spacecraft is measured and any advantage it may offer is determined.

4.1 Motivation

Interstellar objects have been the subject of extensive scientific discussion and a growing body of literature since the discovery of the first two objects — asteroid 1I/'Oumuamua [61] and the comet 2I/Borisov [62] — in the late 2010s. From this initial excitement, statistical models [113, 114, 115] have been created that predict many future ISO detections, especially after the introduction of the Vera C. Rubin Observatory [62, 63] later this decade.

In response to the interest expressed by the scientific community, numerous potential mission concepts for studying these objects using both rendezvous and ballistic trajectories have since been published. Rendezvous trajectories tend to require nuclear-based propulsion systems or high-performance solar sails combined with heavy-lift launch vehicles [116, 117, 92]. Instead of matching the high heliocentric velocity of these objects, a ballistic (or near-ballistic) flyby could be achieved with current propulsion and launch vehicle technologies [66, 114, 65, 118, 119, 67]. A further challenge is presented by the limited window of opportunity afforded by current detection infrastructure and the transient nature of ISOs. One way of addressing this problem would be to create a rapid response capability for future detected ISOs [120, 121, 122] either by storing prebuilt spacecraft on the ground or by staging them on orbit. This latter approach will be demonstrated later this decade by ESA's Comet Interceptor, which stages at the Earth-Moon L2 in wait of a scientifically interesting long-period comet or, potentially, an ISO [123].

A key difficulty with ballistic (non-propulsive) flyby missions is how to mitigate the high speed of interstellar objects. Indeed, with terminal velocities often in the tens of kilometers

Table 4.1: Summary of Trade Study Parameters

Propulsion System	Launch Vehicle	Dataset
None (Ballistic)	Falcon Heavy (Recovered)	Engelhardt/Jedicke [113]
XR-5 Hall Effect SEP	Falcon Heavy (Recovered) w/. STAR 48	Hoover [114]
NEXT-C Gridded Ion SEP	Falcon Heavy (Expended)	
Bipropellant	Falcon Heavy (Expended) w/. STAR 48	
Solar Sail		
XR-5 HLTP		

per second, these trajectories present significant challenges to collecting meaningful data. Onboard propulsion is therefore desirable. By combining two propulsion systems on a single spacecraft, HLTP is able to provide greater thrust than either a SEP thruster or solar sail alone. However, it comes at the cost of a higher vehicle mass – which reduces acceleration – and systems complexity. It is therefore desirable to determine whether HLTP can provide a meaningful net advantage over either of its constituent propulsion systems alone or produce a superior result over other common options.

To address the challenge of needing to quickly fly a trajectory to a fast-moving object with minimal warning, this investigation will make use of a fast-flyby concept with a plausible launch delay. This assumes that, upon detecting an ISO, a 90-day preparation period begins during which a trajectory is planned, a pre-built spacecraft is mated to a launch vehicle, and the mission is given final approval. It is also assumed that sufficient observations will be collected during these 90 days to adequately characterize the ISO's hyperbolic orbit. To help constrain power generation, thermal control, and communications system requirements, the flyby is also required to occur with 3 au of the Sun.

Ideally, the assessment made in this investigation would be based on the known population of ISOs. Unfortunately, with only two such objects having been detected, such a study may not capture the performance with respect to the entire, still undiscovered, population. To address this concern, a statistical evaluation is instead conducted using two probabilistic models of the ISO population. Based on the superior performance of the XR-5 configurations in the prior chapter, an XR-5 HLTP spacecraft is defined and compared against more conventional propulsion options. Trajectories are then optimized with respect to arrival velocity to the entire set of reachable objects. To assess the relative importance of the onboard propulsion, this is then repeated with a range of launch vehicle options with varying performance. In total, the completed trade study consists of 6 different propulsion options, 4 launch vehicles, and 2 target object datasets. These are summarized in Table 4.1. From these results, the ability of HLTP to provide a net advantage in terms of reduced relative flyby velocity to interstellar objects is determined.

4.2 Application Methodology

In this section, the methodology of this ISO mission trade study is described. First, the MELs for the spacecraft used in this chapter are defined. Next, a brief description is provided of the process by which the two statistical models are filtered to find the reachable set of objects.

The initial guess workflow that follows this process is then outlined. Finally, the trade study parallelization routine and any remaining details of the trade study process are given.

4.2.1 Spacecraft Master Equipment Lists

With 6 propulsion options, 4 launch vehicles, and 2 target object datasets, a total of 48 scenarios are considered in this chapter. It would not be practical, however, to define an optimized spacecraft for every combination due to the time required to conduct the multi-iteration, human-in-the-loop optimization process for the remaining scenarios. 12 spacecraft are instead defined to cover the 6 propulsion systems and the 2 target datasets, with each spacecraft being optimized for an expended Falcon Heavy. As an intermediate option in terms of characteristic energy among the four considered launch vehicles, this choice avoids biasing the defined spacecraft towards either overly low or high launch characteristic energies.

The process of defining these spacecraft largely follows the same process described previously in Section 2.3 and Subsection 3.2.1. Spacecraft mass is calculated as the sum of the masses of the individual subsystems. For each subsystem, a basic mass is first determined based on either previous studies, expected requirements, or best practices. As per ANSI/AIAA S-120-2015 [3], a conservative growth allowance is then applied, which reflects the low maturity of these spacecraft specifications. This results in a predicted mass for each subsystem, the sum of which is the predicted dry mass. Finally, the addition of an overall margin of 30% produces an allocated dry mass. For spacecraft that require propellant, the propellant tank and structural masses are set according to the anticipated propellant requirements. However, the launch mass is an optimization variable and less propellant may be loaded if that is optimal. For cases that also require an RCS system, the RCS propellant is set to 1% of the total wet mass. The mass of each spacecraft configuration is summarized in Tables 4.2a and 4.2b for the Engelhardt and Hoover datasets, respectively, while the complete breakdowns by subsystem may be found in Appendix C.

The three dominant drivers of spacecraft mass are power, propulsion, and structure. Starting with power, a 350 W bus requirement is defined. This is based on the 500 W JUMPER Jupiter small-sat concept [108] and the expectation that the power requirements would be somewhat less due to the maximum 3 au limit on the intercept assumed in this work. A large battery is not required for this mission because eclipses are not expected to occur. Therefore, a battery capacity of 1000 W h is specified at 120 W kg^{-1}, which is well within the density offered by current technology [111]. A minimum power generation requirement of 3.15 kW is set to provide full bus power at 3 au, with larger solar arrays specified for the EP configurations. A power to weight ratio of 100 W kg^{-1} [124] is assumed for these arrays and is consistent with available hardware. Finally, the wiring harness is set to 17% of the total power system mass [111], defined here as the sum of the solar arrays, batteries, and harness masses.

For spacecraft with an electric propulsion system, two identical sets of PPUs and thrusters are included on the spacecraft for redundancy, with only one operating at any given time. These values are 18.6 kg [107] and 12.3 kg [105] for an XR-5 and 34.5 kg [125] and 14 kg [106] for a NEXT-C. Tank mass is set to 7.5% of the mass of the propellant within [111]. Per Wertz, Everett, and Puschell [111], the basic structural mass of the overall spacecraft is set to 25% of the total basic dry mass. It is therefore a function of the mass of all other

subsystems. In an effort to produce a lighter spacecraft that would maximize performance over the short anticipated flight times, a 20 kg payload is specified.

For the three configurations that feature electric propulsion, an iterative process is used to size the solar arrays and maximum propellant load. First, array area is optimized using a trade study with an increasingly fine mesh until the mean arrival velocity of the entire target set is minimized. The maximum propellant load is then set to match the top 95% of the target set. Note that the remaining 5% of objects are still accessible, but at a sub-optimal propellant load. This process produces a common spacecraft for all targets that reduces the mean arrival velocity, while avoiding overly large tank and structural masses to support a handful of outliers.

The remaining propulsion options are modelled differently. Instead of specifying a particular bipropellant thruster; a generic thruster is used with a representative specific impulse of 320 sec and an inert mass fraction set to 15% of its propellant mass. The maximum propellant load is set such that the recovered Falcon Heavy is still able to reach the entire set of targets. For the solar sail option, the 52 kg, 7000 m^2 sail from the High-inclination Solar Mission (HISM) concept [99] is used. While this area-to-mass ratio is significantly better than the current state-of-the-art, its inclusion is intended as a possible near-to-medium term enabling technology. Finally, the hybrid low-thrust is modeled as a hall effect-propelled spacecraft with the HISM solar sail attached as an auxiliary system. With its lower dry and overall masses and greater propellant mass, the hall effect option is anticipated to be more promising for the hybrid configuration than the gridded ion alternative due to the mass-sensitive nature of the auxiliary sail.

4.2.2 Synthetic Object datasets and Initial Guess Generation

As a result of the small number of confirmed ISOs, the population of objects has not yet been definitively characterized and, unsurprisingly, significant differences exist in the distributions of objects predicted by different models. In response to such uncertainty, this investigation makes use of two different datasets: Engelhardt et al. [113] (referred to as "Engelhardt/Jedicke") and Hoover et al. [114] (referred to as "Hoover"). The methods and assumptions used to create each of these datasets is outside of the scope of this dissertation and the curious reader is directed to the original published works by these authors.

Engelhardt/Jedicke Dataset

The Engelhardt/Jedicke dataset propagated the paths of 165 378 unique, synthetic objects and simulated sky surveys conducted by ground-based telescopes to produce artificial observational data. In order to use this data, the detectable and reachable subset of ISOs must first be determined from this collection of individual observations known as tracklets. Synthetic target ISOs are identified from the data by first calculating the probability of detection of each unique object and then filtering out those objects with less than a 50% chance of detection. This is a function of the object's visibility at the time of observation and of how "interesting" the observation would appear. To measure the former, a tracklet efficiency score between 0 and 1 is assigned to each observation based on factors such as the distance of the object, whether the object is active (an outgassing comet) or inert (a non-outgassing

Table 4.2: Summary of Spacecraft Masses. Allocated wet mass is the sum of the allocated dry mass, maximum propellant mass, and RCS propellant. The average optimized launch mass corresponds to the expended Falcon Heavy without kick stage launch configuration.

(a) Engelhardt dataset

Configuration	Allocated Dry Mass	Maximum Propellant Mass	Allocated Wet Mass	Average Optimized Launch Mass
Ballistic	238.2 kg	-	238.2 kg	238.2 kg
Hall Effect EP	476.3 kg	307.1 kg	791.4 kg	668.0 kg
Gridded Ion EP	663.0 kg	145.3 kg	816.3 kg	803.8 kg
Bipropellant	392.5 kg	583.0 kg	985.5 kg	624.9 kg
Solar Sail	329.9 kg	-	329.9 kg	329.9 kg
Hall Effect HLTP	597.6 kg	341.0 kg	947.6 kg	813.3 kg

(b) Hoover dataset

Configuration	Allocated Dry Mass	Maximum Propellant Mass	Allocated Wet Mass	Average Optimized Launch Mass
Ballistic	238.2 kg	-	238.2 kg	238.2 kg
Hall Effect EP	406.6 kg	121.9 kg	533.5 kg	491.2 kg
Gridded Ion EP	603.8 kg	56.1 kg	666.9 kg	649.8 kg
Bipropellant	375.6 kg	519.0 kg	903.6 kg	679.4 kg
Solar Sail	329.9 kg	-	329.9 kg	329.9 kg
Hall Effect HLTP	545.1 kg	137.4 kg	689.5 kg	649.8 kg

Table 4.3: An overview of the effect of different filters on the Engelhardt/Jedicke dataset

Applied Filters	No. of Detected ISOs	No. of Detected ISOs $r_p \leq 3$	No. of Ballistic Feasible ISOs (No Delay)	No. of Ballistic Feasible ISOs (90 Day Delay)
All Unique Objects	165 378	1962	359	333
Digest Score > 90	98 572	1338	211	174
All Visible Objects	7806	1224	260	194
50% Probability, 3rd Tracklet	5524	895	128	89
50% Probability, 1st Tracklet	5524	895	148	104
1% Probability, 3rd Tracklet	5552	900	130	90
1% Probability, 1st Tracklet	5582	900	150	105

comet or an asteroid), and the filters being used by the simulated telescope. To represent the latter characteristic, a digest score between 0 and 100 is used. The original data provided by Engelhardt contained both of these values; the calculation of tracklet efficiency and digest score is not an original contribution of this dissertation. Using these two values, the probability Pr_j of the j^{th} object being detected is calculated for a set of observations using telescope filter F with digest scores d_j and tracklet efficiencies ϵ_{jF}:

$$Pr_j = 1 - \prod_F \left[1 - \epsilon_{jF} H\left(d_j - 0.9\right)\right] \tag{4.1}$$

A breakdown of the effect that various filtering decisions has on processing the tracklet data is summarized in Table 4.3. Starting with 165 378 unique objects, only 98 572 meet the required digest score criteria and a mere 7806 are visible to the simulated telescopes. When combined, 5524 are found to have a greater than 50% probability of detection. This is then filtered down to 895 potential target ISOs with a perihelion r_p of less than 3 au. Using a Lambert solver [126], 104 feasible ballistic target objects are found (~2% of detections) that may be reached with a ballistic trajectory that satisfies the required 90 day launch delay after detection, a flight time between 30 days and 3 years, and a $C_3 \leq 60\,\text{km}^2\,\text{s}^{-2}$. Note that the 90 day requirement is calculated from the date of an object's first detectable tracklet and that characteristic energy constraint corresponds to the capability of the lowest performing launch vehicle when paired with the ballistic spacecraft configuration. A larger population of objects would be available using a more powerful launch vehicle, but a consistent population of objects was desired for this study. For context, a C_3 of $150\,\text{km}^2\,\text{s}^{-2}$ – approximately equivalent to the most powerful launch vehicle in this investigation launching the heaviest spacecraft considered – would be able to reach 241 objects from the Engelhardt dataset.

Hoover Dataset

The Hoover dataset similarly simulates a population of interstellar objects and measures detectability based on the performance of real-world telescopes: the Vera C. Rubin Observatory, NEO Surveyor, and PAN-STARRS. However, unlike the Engelhardt/Jedicke dataset, the Hoover dataset was provided in its final, processed form as a catalog of detected objects. No calculations were required to prepare the data for this study. Out of 5 000 000 simulated ISOs, 0.7% are detectable by the Rubin Observatory, 2% are detectable by NEO Surveyor, and 0.03% are detectable by PAN-STARRS. A total of 458 interstellar objects met both the detectability requirements of the Hoover dataset and the reachability requirements of this study.

Initial Guess Generation

Initial guesses for trajectories are found by solving Lambert's problem on the objects provided by the Engelhardt/Jedicke and Hoover datasets. As discussed in Section 4.2.2, these ballistic trajectories are constrained to launch no earlier than 90 days after the detection date of the target ISO, to flight times between 30 days and 3 years, and to a launch characteristic energy $C_3 \leq 60\,\mathrm{km^2\,s^{-2}}$.

4.3 Results

The statistical results for the Engelhardt/Jedicke and Hoover datasets are provided as Figures 4.1 and 4.2. The mean values of arrival velocity in $\mathrm{km\,s^{-1}}$ and an error bar of one standard deviation are displayed for each. In general, the arrival velocities in the Hoover dataset are consistently $5\,\mathrm{km\,s^{-1}}$ to $10\,\mathrm{km\,s^{-1}}$ less than those in the Engelhardt dataset, with the highest performing configurations consistently close to $30\,\mathrm{km\,s^{-1}}$. The lowest mean arrival velocity across both datasets and all configurations is $29.51\,\mathrm{km\,s^{-1}}$. A clear, monotonic improvement exists with increasing launch vehicle performance; the two expendable Falcon Heavy options are always superior to the two recovered alternatives and both configurations with a kick stage are superior to the equivalent without. However, the impact of the launch vehicle is more pronounced in the Hoover dataset, with an average improvement of $7.37\,\mathrm{km\,s^{-1}}$ between the expended Falcon Heavy with kick stage and the recovered Falcon Heavy without. The comparable value in the Engelhardt/Jedicke dataset is only $4.78\,\mathrm{km\,s^{-1}}$.

In the Engelhardt/Jedicke dataset, the best option for onboard propulsion is the hybrid low-thrust combination of an XR-5 hall effect thruster and a $7000\,\mathrm{m^2}$ solar sail. However, the addition of the sail results in an average improvement of only $106\,\mathrm{m\,s^{-1}}$ over the less complex SEP-only option, with a maximum improvement of $288\,\mathrm{m\,s^{-1}}$ when paired with an expended Falcon Heavy and a STAR 48. The average improvement over the ballistic baseline is $4.039\,\mathrm{km\,s^{-1}}$. The NEXT-C configuration came in third. The one exception to this ordering of HLTP, XR-5, and NEXT-C are those results that use a recovered Falcon Heavy without a kick stage. With this lowest-performance option, The XR-5 was superior, followed by the NEXT-C and HLTP.

In the Hoover dataset, the XR-5 configuration has the lowest mean arrival velocity across all four launch vehicles and an average improvement of $1.544\,\mathrm{km\,s^{-1}}$ compared to the ballistic

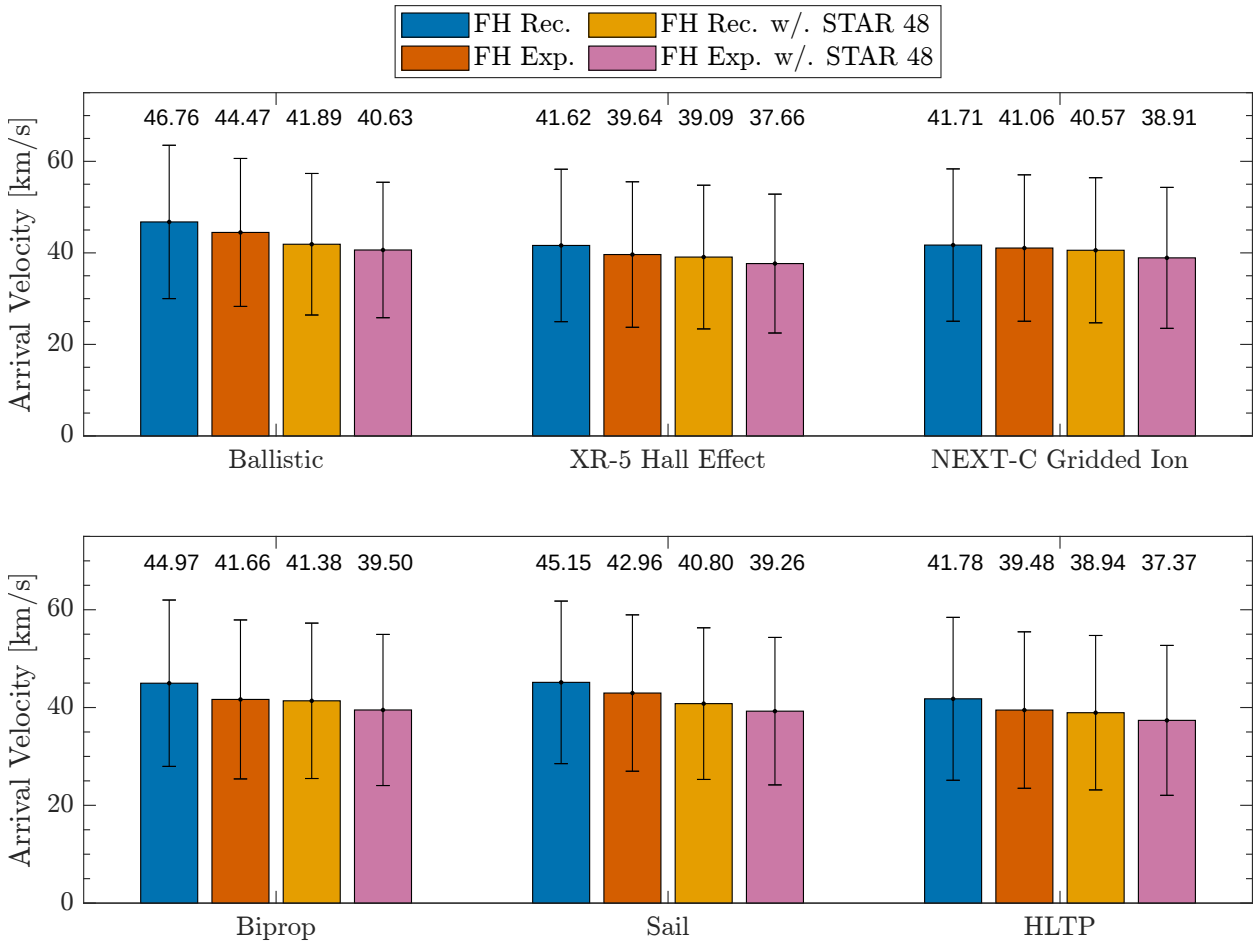

Figure 4.1: Engelhardt/Jedicke dataset statistical results. The mean value and a 1σ errorbar is provided for each bar.

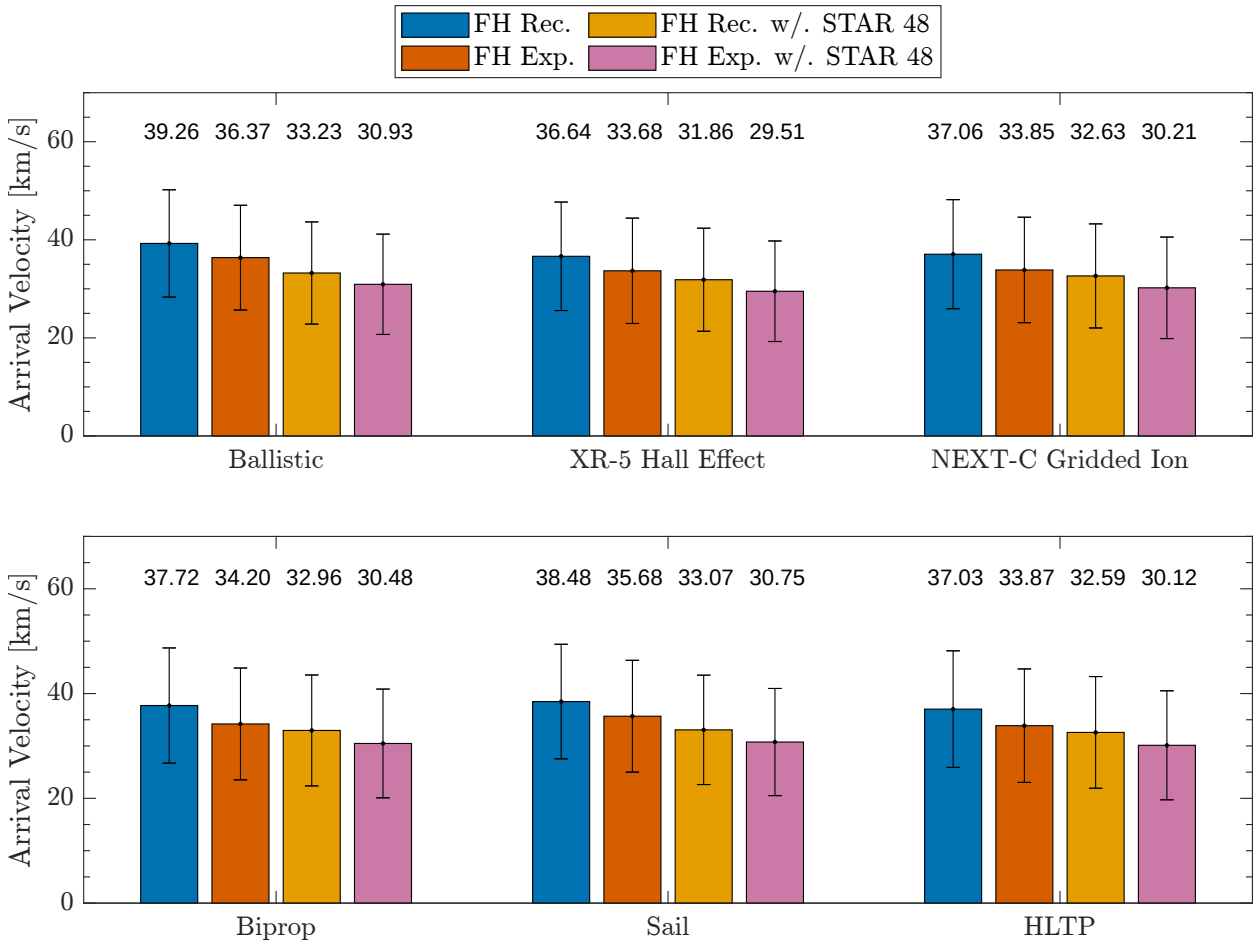

Figure 4.2: Hoover dataset statistical results. The mean value and a 1σ errorbar is provided for each bar.

baselines. The HLTP variant provides slightly worse performance, comparable with that of the gridded ion NEXT-C spacecraft. The gap between the XR-5 and HLTP is, on average, $482\,\mathrm{m\,s^{-1}}$ in favor of the XR-5.

While superior to the ballistic baselines, the bipropellant and solar sail options are consistently the least successful in both datasets. In the Hoover dataset, the bipropellant spacecraft consistently outperforms the solar sail by an average of $655\,\mathrm{m\,s^{-1}}$. In contrast, an interesting pattern emerges in the Endelhardt/Jedicke results. At lower launch energies with the non-kick stage launch vehicles, the bipropellant system is superior to the solar sail. When launched with a kick stage, the solar sail has lower mean arrival velocities.

4.4 Discussion

In the previous section, it was established that the use of onboard propulsion decreases the average ISO encounter velocity. However, the degree to which it does so varies between datasets, with the relative improvement with respect to the optimized ballistic baseline being consistently greater in the Engelhardt/Jedicke dataset. For example, in that dataset, the use of onboard propulsion reduces the mean value by a maximum of 11.2%, while in the Hoover dataset, the improvement to the same configuration is only 6.9%. In both datasets, the propellant-consuming configurations of the hall effect SEP, gridded ion SEP, and hall effect HLTP experience the greatest improvements relative to the baseline, while the solar sail sees more modest benefits. A summary of the performance of each system relative to the appropriate ballistic baseline may be found in Table 4.4. Note that these comparisons are always made in a like-for-like manner in which the performance of a given propulsion option is compared against the ballistic solution with the same launch vehicle.

Launch vehicle performance is a driving factor in both datasets. As previously established, a clear improvement in encounter velocity is observed with increasing launch vehicle performance in all cases. However, the benefit that a given onboard propulsion system provides over the ballistic alternative using the same launch vehicle varies. In general, the relative effectiveness of onboard propulsion is reduced in the kick stage configurations, both as a proportion of the overall arrival speed and in terms of actual velocity. This may have consequences for the selection of a mission architecture. Should continuous-thrust configurations prove problematic, such as for the 90 day limit on the mission planning period or budgetary constraints, the penalty stemming from the selection of a ballistic spacecraft may be minimized by using a kick stage.

With the general impact of launch vehicle performance understood, it is helpful to now isolate and remove it from consideration. Consider the plot of characteristic energy shown in Fig. 4.3. The two characteristic energy curves of the Falcon Heavy on its own are relatively flat, while the kick stage curves increase rapidly as mass decreases. Most importantly, the curve for the expended Falcon Heavy is almost perfectly flat, with nearly all spacecraft being constrained by an identical upper limit on characteristic energy of approximately $C_3 \leq 100\,\mathrm{km^2\,s^{-2}}$. The only meaningful exception to this is the Engelhardt/Jedicke HLTP configuration, which is constrained to $C_3 \leq 97\,\mathrm{km^2\,s^{-2}}$ due to its additional mass. This flat curve allows for a like-for-like comparison between spacecraft configurations.

The expended Falcon Heavy case and its flat characteristic energy curve allows for an

Table 4.4: Change in arrival velocity with respect to the ballistic baseline for the same launch vehicle.

(a) Engelhardt/Jedicke Dataset Results

Configuration	F.H. Recovered	F.H. Expended	F.H. Recovered w/. STAR 48	F.H. Expended w/. STAR 48
Hall effect EP	−11.0%	−10.9%	−6.7%	−7.3%
Gridded ion EP	−10.8%	−7.7%	−3.1%	−4.2%
Bipropellant	−3.8%	−6.3%	−1.2%	−2.8%
Solar Sail	−3.4%	−3.4%	−2.6%	−3.4%
Hall effect HLTP	−10.6%	−11.2%	−7.0%	−8.0%
Hall effect EP	$-5.1\ \mathrm{km\,s^{-1}}$	$-4.8\ \mathrm{km\,s^{-1}}$	$-2.8\ \mathrm{km\,s^{-1}}$	$-3.0\ \mathrm{km\,s^{-1}}$
Gridded ion EP	$-5.1\ \mathrm{km\,s^{-1}}$	$-3.4\ \mathrm{km\,s^{-1}}$	$-1.3\ \mathrm{km\,s^{-1}}$	$-1.7\ \mathrm{km\,s^{-1}}$
Bipropellant	$-1.8\ \mathrm{km\,s^{-1}}$	$-2.8\ \mathrm{km\,s^{-1}}$	$-0.5\ \mathrm{km\,s^{-1}}$	$-1.1\ \mathrm{km\,s^{-1}}$
Solar Sail	$-1.6\ \mathrm{km\,s^{-1}}$	$-1.5\ \mathrm{km\,s^{-1}}$	$-1.1\ \mathrm{km\,s^{-1}}$	$-1.4\ \mathrm{km\,s^{-1}}$
Hall effect HLTP	$-5.0\ \mathrm{km\,s^{-1}}$	$-5.0\ \mathrm{km\,s^{-1}}$	$-2.9\ \mathrm{km\,s^{-1}}$	$-3.3\ \mathrm{km\,s^{-1}}$

(b) Hoover Dataset Results

Configuration	F.H. Recovered	F.H. Expended	F.H. Recovered w/. STAR 48	F.H. Expended w/. STAR 48
Hall effect EP	−6.7%	−7.4%	−4.1%	−4.6%
Gridded ion EP	−5.6%	−6.9%	−1.8%	−2.3%
Bipropellant	−3.9%	−6.0%	−0.8%	−1.5%
Solar Sail	−2.0%	−1.9%	−0.5%	−0.6%
Hall effect HLTP	−5.7%	−6.9%	−1.9%	−2.6%
Hall effect EP	$-2.6\ \mathrm{km\,s^{-1}}$	$-2.7\ \mathrm{km\,s^{-1}}$	$-1.4\ \mathrm{km\,s^{-1}}$	$-1.4\ \mathrm{km\,s^{-1}}$
Gridded ion EP	$-2.2\ \mathrm{km\,s^{-1}}$	$-2.5\ \mathrm{km\,s^{-1}}$	$-0.6\ \mathrm{km\,s^{-1}}$	$-0.7\ \mathrm{km\,s^{-1}}$
Bipropellant	$-1.5\ \mathrm{km\,s^{-1}}$	$-2.2\ \mathrm{km\,s^{-1}}$	$-0.3\ \mathrm{km\,s^{-1}}$	$-0.4\ \mathrm{km\,s^{-1}}$
Solar Sail	$-0.8\ \mathrm{km\,s^{-1}}$	$-0.7\ \mathrm{km\,s^{-1}}$	$-0.2\ \mathrm{km\,s^{-1}}$	$-0.2\ \mathrm{km\,s^{-1}}$
Hall effect HLTP	$-2.2\ \mathrm{km\,s^{-1}}$	$-2.5\ \mathrm{km\,s^{-1}}$	$-0.6\ \mathrm{km\,s^{-1}}$	$-0.8\ \mathrm{km\,s^{-1}}$

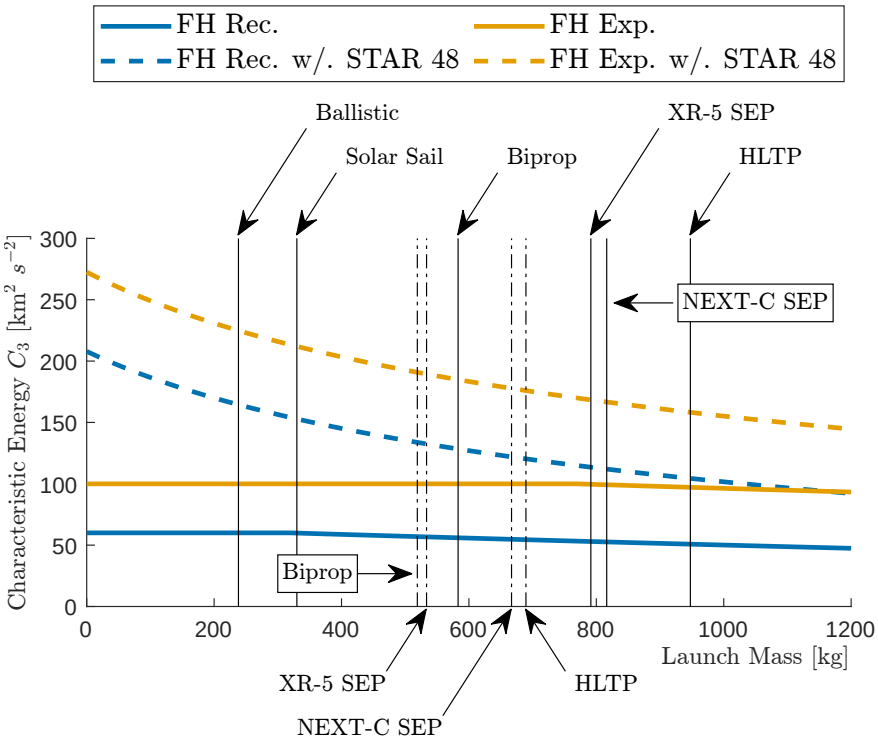

Figure 4.3: Characteristic energy C_3 available for each vehicle configuration at their maximum propellant limit. Annotations on the top half of the image that point to solid vertical lines are for configurations optimized for either the Engelhardt/Jedicke dataset or those that are common to both datasets. Annotations below the figure that point to dashed vertical lines are for the Hoover dataset.

estimate to be made of the additional performance gained solely by the addition of a solar sail to create a hybrid low-thrust spacecraft. In the Engelhardt/Jedicke and Hoover dataset, the arrival velocity of the solar sail spacecraft is, on average, $2.8\,\mathrm{km\,s^{-1}}$ and $0.7\,\mathrm{km\,s^{-1}}$ lower than that of the ballistic baseline. However, the HLTP spacecraft only improves upon the hall effect spacecraft by $0.2\,\mathrm{km\,s^{-1}}$ in the Engelhardt/Jedicke dataset and is inferior by $0.2\,\mathrm{km\,s^{-1}}$ in the Hoover dataset. While a pure solar sail spacecraft is able to make a measurable and meaningful improvement in terms of arrival velocity, the addition of a next-generation solar sail subsystem to a far heavier SEP spacecraft that is already equipped with a powerful thruster only has a small benefit at best.

One potential hypothesis for the failure of HLTP to significantly improve mean flyby velocities is that, while its total thrust may be the highest, its acceleration may actually be lower. As per Newton's second law, if the increase in mass due to the addition of the sail is greater than resulting increase in thrust, the acceleration will decrease. This could be a serious issue. While it was referred to previously in this chapter as a thrust-limited mission, it would be more accurate to describe the ISO flyby problem as one that is acceleration-limited; if a spacecraft had infinite acceleration, it could instantaneously match the velocity of any object. To check such a possibility, the maximum acceleration of all four continuous-thrust spacecraft are given in Table 4.5. In both datasets, HLTP is found to possess the greatest

Table 4.5: Maximum thrust and acceleration for continuous thrust spacecraft. For SEP spacecraft, the maximum thrust values are those produced by the thruster and power models defined by the coefficients provided in Tables A.3 and A.2 at a given thruster's maximum input power. For solar sail spacecraft, maximum thrust is measured at 1 au with the sail normal and the Sun-spacecraft line aligned for maximum force in the sail normal direction. Acceleration is measured at the average optimized launch mass stated in Table 4.2.

Configurations	Maximum Thrust	Maximum Acceleration	
		Engelhardt/Jedicke	Hoover
Hall effect EP	0.1592N	$2.3828 \times 10^{-4} \mathrm{m\,s^{-1}}$	$3.2430 \times 10^{-4} \mathrm{m\,s^{-1}}$
Gridded ion EP	0.2113N	$2.6282 \times 10^{-4} \mathrm{m\,s^{-1}}$	$3.2511 \times 10^{-4} \mathrm{m\,s^{-1}}$
Solar Sail	0.0587N	$1.7793 \times 10^{-4} \mathrm{m\,s^{-1}}$	$1.7793 \times 10^{-4} \mathrm{m\,s^{-1}}$
Hall effect HLTP	0.2179N	$2.6792 \times 10^{-4} \mathrm{m\,s^{-1}}$	$3.3533 \times 10^{-4} \mathrm{m\,s^{-1}}$

peak acceleration. This comes with an important caveat, however: maximum thrust is only available in the outward radial direction from the Sun.

This directional issue may be expected to become significant whenever a trajectory requires large, out-of-plane maneuvers. Consider the two trajectories shown in Fig. 4.4. As shown by the black acceleration vectors, the mostly in-plane trajectory of Subfig. 4.4a is able to make good use of a solar sail. In contrast, the control solution of the largely out-of-plane trajectory of Subfig. 4.4b is almost entirely provided by the SEP system. Due to the dominant cosine squared term of the sail model in Eq. 2.24, the peak acceleration of the HLTP spacecraft falls below that of the gridded ion thruster alternatives at 15 deg and 20 deg of off-normal pointing for the Engelhardt/Jedkicke and Hoover configurations, respectively. With the inclination of objects in both datasets spanning from 0 deg to 180 deg, the greater performance of an HLTP spacecraft may simply be unavailable when flying many of the required trajectories.

While outside of the primary scope of this dissertation, it is valuable to consider these results within the broader context of the motivation for this work. Encounter velocity is a significant issue for any ISO mission and, in particular, for any that wish to collect samples of extrasolar volatiles. Summarized in Table 4.6, encounter velocities for previous successful small-body flyby missions were between $6.1\,\mathrm{km\,s^{-1}}$ and $15.0\,\mathrm{km\,s^{-1}}$. During the development of the Stardust mission, laboratory testing demonstrated that the collection of cometary particles in an aerogel could be conducted at velocities of up to $7\,\mathrm{km\,s^{-1}}$, while the collection of interstellar dust was potentially possible at velocities of up to $15\,\mathrm{km\,s^{-1}}$ [127]. Using the fast-flyby mission framework defined in this work, significant technological development may be necessary to enable a scientifically meaningful flyby mission to an average interstellar object.

However, this issue was not unforeseen and significant progress has been made towards addressing it. Launching in 2029, ESA's Comet Interceptor mission expects to encounter a presently unknown long-period comet at a relative velocity of up to $70\,\mathrm{km\,s^{-1}}$. As such, the instrumentation, which includes imaging equipment, a mass spectrometer, and dust detectors [128], is being designed to meet this requirement [129] and may be leveraged for a future ISO mission. Other lessons, such as the effect of high-velocity dust particle impacts [130, 131],

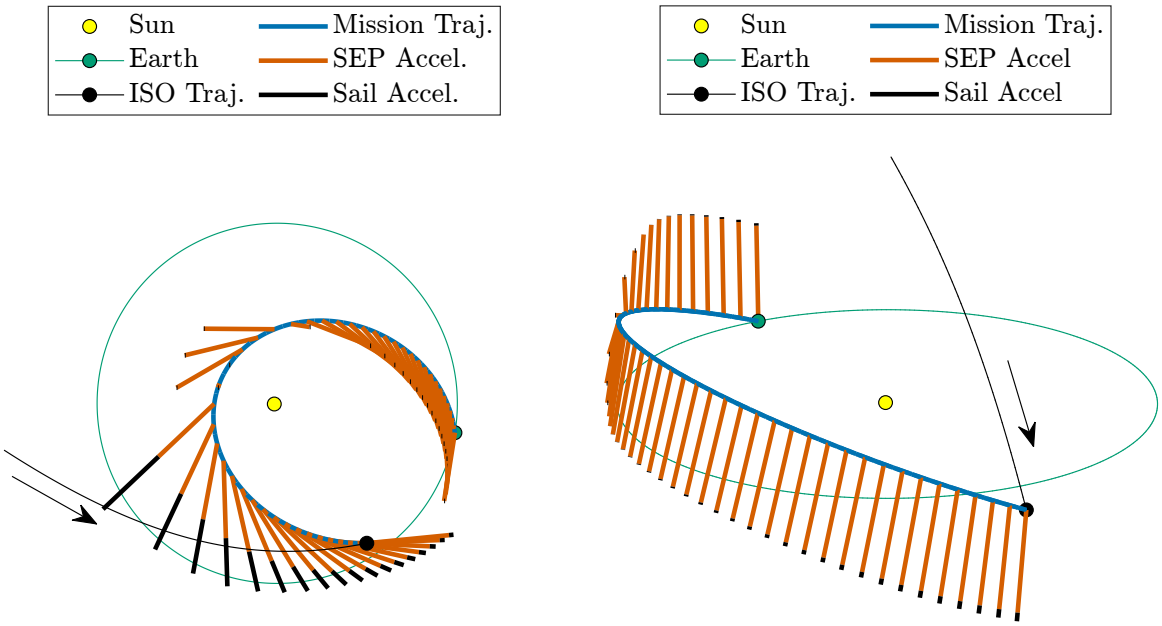

(a) A flyby of a low-inclination ISO

(b) A flyby of a high-inclination ISO

Figure 4.4: A comparison of two Engelhardt/Jedicke object flybys. In Fig. 4.4a, the trajectory is largely planar, passes close to the Sun, and permits thrust directions that allow the sail to be highly effective. In Fig. 4.4b, the target object is highly inclined, resulting in out-of-plane thrust arcs that make minimal use of the solar sail.

will undoubtedly prove equally useful.

4.5 Conclusions

Interstellar objects are scientifically valuable targets that pose a significant challenge to both mission planning and operations due to the difficulty of detecting them and the extreme velocities at which they pass through the solar system. This chapter considered a "fast-flyby" mission architecture using a dedicated, post-detection launch onto a direct trajectory in order to minimize post-detection preparation, eliminate gravity assist availability constraints, and maximize the performance of the available launch vehicle. To address the challenging onboard propulsion demands required to achieve an acceptable flyby velocity, a hybrid low-thrust spacecraft was presented as a promising solution due to the high combined thrust of a SEP thruster and a solar sail. Using synthetic target objects from two different datasets, trajectories were optimized for arrival velocity and compared against the five alternative, more conventional spacecraft options as part of a larger mission trade study.

This evaluation demonstrated that the higher total thrust may allow such an HLTP spacecraft to reduce the flyby velocity of an interstellar object mission more than a spacecraft equipped with either of its constituent propulsion systems alone. In the Engelhardt/Jedicke dataset, HLTP was the most effective form of onboard propulsion, with a mean arrival velocity of $37.37\,\mathrm{km\,s^{-1}}$ when paired with an expended Falcon Heavy and a STAR 48 kickstage.

Table 4.6: A summary of previous successful flyby missions of small bodies and their relative velocities at intercept [4, 5, 6, 7, 8, 9, 10, 11, 12, 13]. Note that year in the first column refers to the launch year.

Year	Mission	Object	Object Size	Flyby Velocity	Sample Collection
1996	NEAR Shoemaker	253 Mathilde	66 x 48 x 44 km	9.9 $\mathrm{km\,s^{-1}}$	No
1999	Stardust	5535 Annefrank	6.6 x 5.0 x 3.4 km	7.4 $\mathrm{km\,s^{-1}}$	No
		81P/Wild 2	1.65 x 2.00 x 2.75 km	6.1 $\mathrm{km\,s^{-1}}$	Yes
2004	Rosetta	2867 Šteins	6.8 x 5.7 x 4.4 km	8.6 $\mathrm{km\,s^{-1}}$	No
		21 Lutetia	121 x 101 x 75 km	15.0 $\mathrm{km\,s^{-1}}$	No
2006	New Horizons	486958 Arrokoth	35.95 x 19.90 x 9.75 km	14.0 $\mathrm{km\,s^{-1}}$	No
2010	Chang'e-2	4179 Toutatis	1.92 x 2.29 x 4.60 km	10.7 $\mathrm{km\,s^{-1}}$	No

In the results of the Hoover dataset, HLTP came in a close second, with a mean arrival velocity of $30.12\,\mathrm{km\,s^{-1}}$, compared to $29.51\,\mathrm{km\,s^{-1}}$ for the hall effect SEP alternative. The ability to conduct operations at high velocities is therefore likely to remain necessary for any mission that uses the framework considered here. However, all of these values are quite high compared to the flyby velocities of previous successful missions. With its similar goal of targeting a high-speed object selected after launch, the lessons learned from ESA's upcoming Comet Interceptor are likely to aid in enabling a future ISO mission.

Across all propulsion options and both datasets, launch vehicle performance dominated the results. A clear, monotonic improvement in arrival velocity with increasing characteristic energy was discovered that outweighed the improvements offered by the onboard propulsion systems. After controlling for the impact of the launch vehicle, it was found that the addition of a solar sail to a SEP baseline spacecraft fails to provide a clear and meaningful improvement to mean flyby velocity. While the additional thrust of a solar sail does permit an HLTP spacecraft to produce the highest peak acceleration of any of the considered spacecraft, this is only true in the outward radial direction. When flying trajectories that require a large difference between the Sun-spacecraft and spacecraft attitude vector, the additional thrust produced by the solar sail is largely eliminated. A common situation in which this would occur is an out-of-plane maneuver, such as an inclination change. The actual potential advantages of HLTP will therefore be determined by the characteristics of the real-world population of interstellar objects, which will be refined as additional observations are collected over the coming decade.

Chapter 5

Conclusions

The use of hybrid low-thrust propulsion on small-body and heliophysics missions was investigated in this dissertation using realistic constraints and higher-fidelity modeling. This was done with the goal of determining whether it would provide superior performance to traditional methods of propulsion and, if so, what performance would be required for it to do so. Two applications were considered: a flight to a circular, 1 au, 90 deg inclined orbit of the Sun and missions to interstellar comets and asteroids.

To accomplish these objectives, a new propulsion model was assembled from pre-existing, non-idealized sail, power, and propulsion models. Detailed mass estimates were then defined for each simulated spacecraft following best practices relating to margin and growth allowances. To provide context for the results, a new mass estimate for a solar sail subsystem based on the current state-of-the-art was calculated. Finally, to address the primary questions posed by this investigation, trade studies were conducted by generating optimal trajectories using a custom implementation of direct forward-backward multiple shooting.

5.1 Summary of Contributions

Three contributions to the literature were defined in Chapt. 1. The conclusions of each are summarized in this section.

5.1.1 An Assessment of Hybrid Low-Thrust Propulsion

In Chapter 3, HLTP was evaluated on a Jupiter-Earth-Earth gravity assist trajectory with the goal of decreasing the launch mass of the spacecraft. By doing so, the propellant mass fraction would be reduced and the payload mass fraction increased. Two SEP systems were considered – an XR-5 hall effect thruster and a NEXT-C gridded ion thruster – and spacecraft were defined for both. After optimizing baseline trajectories using these spacecraft, trade studies were conducted by adding an auxiliary solar sail and sweeping over sail subsystem area and mass. This was conducted both at the predicted and basic mass estimates for the spacecraft, thus covering the most conservative and optimistic cases, respectively. Each trajectory within these trade studies was compared against the appropriate SEP baseline and, by doing so, the overall change in mass was determined.

When applied to this particular scenario, hybrid low-thrust propulsion was found to be a sound concept, with significant mass reductions being achieved. The greatest possible benefit of adding an auxiliary solar sail was found in the minimum mass, maximum area corner of the design space: 0 kg, 8000 m^2. In this bounding case, the HLTP spacecraft had a net reduction in mass of 172 kg, a propellant mass fraction decrease of 0.1147, and a payload mass fraction increase of 0.0079. A small net mass advantage was also found to be possible with the next-generation of solar sails, as represented by the 52 kg, 7000 m^2 sail of the High Inclination Solar Mission. The addition of a solar sail was more beneficial to the hall effect spacecraft due to the lower specific impulse of the thruster and the subsequent effects that this had. This XR-5 baseline had a higher propellant mass, which resulted in greater structure and tank subsystem masses to support it. The impact of reducing the propellant requirements for this spacecraft was therefore greater than in the already efficient NEXT-C spacecraft.

In Chapter 4, HLTP was used to minimize the relative flyby velocity of missions to interstellar comets and asteroids as part of a fast flyby concept. A response to the dual challenges of reacting to a late ISO detection and of achieving a rendezvous without extreme trajectories or technologies, this study specified a minimum 90 d launch delay after detection and limited the intercept to flybys within 3 au of the Sun. Using two databases of synthetic target ISOs, a statistical comparison was made against five alternative propulsion options across four launch vehicles. This allowed for HLTP to be assessed not only against other alternative spacecraft configurations, but for conclusions to also be drawn regarding the effectiveness of any form of onboard propulsion on this difficult, thrust-limited problem.

In this use case, HLTP did not demonstrate a clear and meaningful advantage over the alternative forms of propulsion. In the first database, HLTP had the lowest mean arrival velocity, while in the second dataset, it came in second place to a SEP spacecraft with a hall effect thruster. In both cases, the propulsion system did not substantially differentiate itself in performance from either the hall effect or gridded ion SEP spacecraft. Across all propulsion options, launch vehicle performance was the single most important factor in driving down arrival velocities. However, no combination of propulsion or launch vehicle could reduce the mean arrival velocity towards historically feasible values. The successful demonstration of operations at high relative velocities by ESA's Comet Interceptor will therefore be critical to enabling any ISO flyby mission.

This chapter also included an analysis of the cause of HLTP's failure to differentiate itself from SEP-alone. While the hybrid low-thrust spacecraft had both the highest peak thrust and acceleration, this was only true at sail incidence angles close to 0 deg. At a crossover point between 15 deg and 20 deg, the sail's thrust drops sufficiently that the overall spacecraft acceleration falls below that of the highest-performing SEP configurations. Unfortunately, the predicted ISO population is highly inclined, and out-of-plane inclination changes are frequently required. Therefore, while the peak acceleration of HLTP may be greater than SEP-alone, the usable acceleration is often roughly equivalent or lower. HLTP is therefore unlikely to be worth the additional systems complexity for this particular application.

5.1.2 An Estimate of Required Sail Performance

For HLTP to be broadly superior to SEP, a net mass advantage must be achieved. In order to estimate the performance necessary to satisfy this condition, the areal density indicated by the trade study breakeven contours of Chapter 3 were used. It was found that these contours are almost entirely linear, which indicates that this performance requirement remains proportionally constant as the sail subsystem varies in size. For the XR-5 equipped spacecraft, a sail subsystem areal density of $7.3\,\mathrm{g\,m^{-2}}$ to $7.4\,\mathrm{g\,m^{-2}}$ was required, while $4.7\,\mathrm{g\,m^{-2}}$ to $4.8\,\mathrm{g\,m^{-2}}$ was required for the NEXT-C spacecraft. These small ranges result from minor variations between the predicted and basic mass trade studies. Attributed to numerical noise, their consistency suggests that thruster performance is likely driving these values, rather than spacecraft mass. Due to its thruster's lower specific impulse, the XR-5 spacecraft benefited more from the addition of an auxiliary sail than the already efficient NEXT-C spacecraft.

For a significant improvement in mass to be obtained, a subsystem areal density lower than $7.4\,\mathrm{g\,m^{-2}}$ must be achieved. While the stated performance goal for the next generation solar sail would meet this requirement, the current state-of-the-art is only $28\,\mathrm{g\,m^{-2}}$ and lacks flight heritage. While $15\,\mathrm{g\,m^{-2}}$ has been demonstrated on orbit, controllability and long-term functionality remain to be proven [57]. In general, significant progress must still be made in solar sail development for the beneficial portion of the design space to be accessed.

5.1.3 A Complete Propulsion Model

In response to a perceived over-reliance on idealized propulsion models in the literature, this assessment of HLTP featured a new propulsion model composed of nonideal sail, power, and SEP thruster models. In addition to accounting for small efficiency losses and margins in the various subsystems, this now captures two important performance and engineering constraints: distance-varying power and plausible thrust directions. By doing so, it prevents the potential benefits of HLTP from being under- or over-estimated.

In previous idealized power and thruster models, solar array power was assumed to be constant or not included at all. In reality, SEP performance is constrained by physics in a way similar to that of the solar sail; both solar power and solar radiation pressure vary as distance squared to the Sun. By including a nonideal solar power model, SEP thrust is now appropriately limited by the spacecraft's distance to the Sun. This prevents unrealistic thrust availability in the outer solar system. It also has a significant impact on the mass model due to the need to specify additional solar arrays to meet bus power requirements at large solar distances.

In the existing literature, the SEP and sail normal thrust unit vectors were independent of each other, with only the sail vector being required to point away from the Sun. While real-world SEP systems are capable of some gimballing, it would be impossible to build a spacecraft with $\pm 360\,\mathrm{deg}$ of altitude and azimuth pointing without impinging on the solar sail or the use of multiple independent thrusters at a significant weight penalty. This latter solution, depending on the implementation, may also require thrust vectors that fail to pass through the center of mass, thus creating a challenging attitude control problem. To address this, a colinear requirement was placed on the two unit vectors. While this degrades some

of the purported advantages of HLTP – thrust in this model remains impossible towards the Sun – it is more plausible and avoids any potential attitude control problems.

5.2 Future Work

While this dissertation explored two applications of HLTP, many more will need to be evaluated to fully characterize the mission types that would most benefit from this technology. In Chapt. 3, the JEEGA trajectory included extended periods in the outer solar system where the auxiliary sail had neglibible performance. In Chapt. 4, the thrust directions were frequently unsuitable for a solar sail and all forms of onboard propulsion were, broadly speaking, unable to create a feasible mission. These therefore may not have been the best missions for demonstrating hybrid low-thrust propulsion.

In the future, applications within Earth's orbit and close to the ecliptic should be considered in order to maximize the performance of the auxiliary solar sail. The trajectories to fly such a mission would take advantage of the increased thrust granted by the inverse squared scaling of solar radiation pressure and avoid extreme out-of-plane maneuvers with large Sun incidence angles. These could include planetary missions to Mercury and Venus. Alternatively, multi-revolution trajectories with low perihelia could be considered as a way of reaching bodies in the outer solar system, but this would require a different trajectory optimization method; direct shooting struggles with extremely large problems composed of many thousands of variables.

One specific mission type from the literature that should be revisited is that of the pole-sitter. Using continuous thrust, a pole-sitter uses a non-Keplerian orbit in order to remain over a pole of a planet. In contrast to traditional observational options such as a Molniya orbit, this provides a continuous observational capability with a single spacecraft at a fairly constant altitude. While primarily considered by Ceriotti, McInnes, and Heiligers in the context of Earth observation [47, 45, 48], Heiligers et al. also studied this concept for missions at Venus and Mars [49]. It was frequently found that a hybrid propulsion option would offer lower launch masses and longer missions than SEP-alone, while sail-alone was frequently unable to provide the necessary performance. It may therefore be one of the best applications of HLTP and should be revisited in the future as new and better characterized solar sail designs become available.

To correct the unrealistic, unconstrained SEP thrust vector seen in the literature, this investigation fixed the SEP thrust direction to the sail normal unit vector. However, modern SEP systems offer non-negligible gimballing capabilities, such as the 12 deg seen on the Dawn spacecraft [69]. The impact of this on overall performance should therefore be studied in the future. It may also useful to combine this with improved attitude control modelling, since it would be likely to impose greater demands on that system.

Due to its impact on acceleration, reducing the overall mass of an HLTP spacecraft would be beneficial. One possible way to accomplish this would be to replace traditional solar panels with thin-film solar arrays embedded within the solar sail. This is not a new concept, with a non-propulsive solar power sail – a sail structure to support thin-film solar arrays and not for propulsion – being included in JAXA's OKEANOS proposal [91]. In the HLTP literature, Li et al. [42] and Heiligers et al. [50] both assumed the use of thin-film solar arrays that

would be embedded in their large, propulsive solar sails. However, due to their lack of power modeling, certain important consequences of this system have yet to be evaluated. In this investigation, solar arrays were assumed to always face the Sun through the use of rotating mounts. Even if the spacecraft's attitude resulted in minimal sail thrust, this arrangement ensured that the SEP system would always be provided with the maximum available power. However, if a solar power sail were to be used instead, the performance of both the SEP thruster and auxiliary sail would become dependent on spacecraft's attitude. A comparison between a heavy, attitude-independent solar array and a lightweight, attitude-dependent solar power sail should be produced.

5.3 Final Thoughts

Hybrid propulsion is not a new idea. The galleys of the ancient Greeks were predominantly driven by oars, yet also had sails for additional propulsion. Such an arrangement remained common for millennia, as later vessels such as the Viking longships of the Middle Ages and even the galleys of the Battle of Lepanto in 1571[1] demonstrate. Only in the early modern period did sail power come to entirely dominate military ship design [132]. However, other forms of hybrid propulsion have proven to be far less long-lasting.

Since the start of the Industrial Revolution, hybrid forms of propulsion have frequently been transitional technologies. In the 19th century, steam-driven propulsion revolutionized transportation. Unreliable and inefficient, early steam engines were incapable of supporting long voyages and vessels that used them operated primarily as sailing ships. However, as the technology improved over the following decades, designs shifted towards purely steam-driven vessels [133]. An equivalent, but brief, transitional period existed in the mid-20th century between piston-driven propeller aircraft and jets, with aircraft such as the Convair B-36 Peacemaker featuring a mixed arrangement remembered by the phrase "six turning and four burning" [134]. Today, hybrid propulsion has become common once more in the form of hybrid gasoline-electric vehicles. The question therefore is: if hybrid low-thrust propulsion becomes a viable technology, will it be a long-term technology or simply a temporary one on the way to pure sailcraft?

Based on the results of this dissertation, I would argue that the latter is more likely. Hybrid forms of propulsion are frequently stop-gap technologies because they result in compromised vehicles that are only viable until the up-and-coming technology matures. Electric cars are widely believed to be the future, but are currently held back by the limitations of range, charging infrastructure, and price [135]. Hybrid vehicles are therefore popular, but this is in spite of the packaging challenges of adding electric drive train components to an internal combustion vehicle [136]. Such issues were not uncommon historically. Steam-sail hybrid vessels suffered from limited cargo capacity due to the need to reserve room for machinery spaces and coal [133]. In the case of hybrid low-thrust propulsion, packaging is not the main issue. The main concern is instead weight and its impact on usable acceleration.

[1]The Battle of Lepanto was fought between Holy League and the Ottoman Empire and featured over 400 vessels. While fully-rigged ships such as the caravels used by Columbus had appeared at this point, this battle was fought almost entirely by primarily oar-driven galleys, with support by the more sail-focused hybrid galeass [132].

In the coming decades, it is hoped that solar sailing technology will mature, thus enabling the creation of useful hybrid low-thrust propulsion systems. However, should this occur, it would also enable the creation of high-performance sailcraft, unburdened by the additional mass of multi-kilowatt solar arrays, power processing units, thrusters, propellant tanks, and other ancillary systems. Would any use cases then remain in which HLTP provides a sufficient advantage over SEP to justify its additional complexity while also not motivating a move to a pure sailcraft? This question should be considered in the future while also motivating the more exhaustive study of applications necessary to answer it.

Appendix A

Spacecraft Propulsion Parameters

Table A.1: Solar Array Coefficients

γ_0	γ_1	γ_2	γ_3	γ_4
1.1705	0.0289	-0.2197	-0.0202	-0.0001

Table A.2: Solar Sail Coefficients [14]

$\tilde{r}$	s	B_f	B_b	ϵ_f	ϵ_b
0.91	0.89	0.79	0.67	0.025	0.27

Table A.3: Electric Thruster Polynomial Coefficients

Coefficient	XR-5		NEXT-C	
	F_SEP	$\dot{m}$	F_SEP	$\dot{m}$
a	0	0	$6.916\,788 \times 10^{-5}$	$2.799\,614 \times 10^{-9}$
b	$-1.248\,49 \times 10^{-3}$	$-0.180\,455 \times 10^{-6}$	$-1.556\,858 \times 10^{-3}$	$-6.147\,473 \times 10^{-8}$
c	$9.740\,299 \times 10^{-3}$	$1.532\,521 \times 10^{-6}$	$1.281\,034 \times 10^{-2}$	$4.799\,391 \times 10^{-7}$
d	$-2.910\,923\,2 \times 10^{-2}$	$-4.905\,998 \times 10^{-6}$	$-4.584\,776 \times 10^{-2}$	$-1.515\,115 \times 10^{-6}$
e	$9.392\,472\,3 \times 10^{-2}$	$9.582\,856 \times 10^{-6}$	$9.426\,715 \times 10^{-2}$	$2.024\,782 \times 10^{-6}$
f	$-1.631\,876\,7 \times 10^{-2}$	$-0.702\,439 \times 10^{-6}$	$-2.166\,929 \times 10^{-2}$	$1.222\,353 \times 10^{-6}$

Appendix B

Solar Sail Performance

B.1 Solar Sail Performance Comparison

Using the ideal and nonideal sail models introduced as Equations 2.23, 2.24, and 2.25 and the parameters provided in Table A.1, a comparison of peak sail performance can be made. By setting the incidence angle θ to zero, the force per unit area is found using $P_{\mathrm{SRP}} = 4.56\,\mu\mathrm{N\,m^{-2}}$ and $A_{\mathrm{sail}} = 1\,\mathrm{m}^2$.

$$F_{\mathrm{ideal,max}} = 2\left(4.56\,\mu\mathrm{N\,m^{-2}}\right)\left(1\,\mathrm{m}^2\right)\cos^2\left(0\,\mathrm{deg}\right) = 9.12\,\mu\mathrm{N} \tag{B.1}$$

$$\begin{aligned} F_{\mathrm{n,max}} = {} & \left(4.56\,\mu\mathrm{N\,m^{-2}}\right)\left(1\,\mathrm{m}^2\right)\{\left(1+(0.91)\,(0.89)\right)\cos^2\left(0\,\mathrm{deg}\right)+ \\ & (0.79)\,(1-0.89)\,(0.91)\cos\left(0\,\mathrm{deg}\right)+ \\ & (1-0.91)\,\frac{(0.025)\,(0.79)-(0.27)\,(0.67)}{0.025+0.27}\cos\left(0\,\mathrm{deg}\right)\} \\ F_{\mathrm{n,max}} = {} & 8.39\,\mu\mathrm{N} \end{aligned} \tag{B.2}$$

$$F_{\mathrm{t}} = \left(4.56\,\mu\mathrm{N\,m^{-2}}\right)\left(1\,\mathrm{m}^2\right)\left(1-(0.91)\,(0.89)\right)\cos\left(0\,\mathrm{deg}\right)\sin\left(0\,\mathrm{deg}\right) = 0\,\mu\mathrm{N} \tag{B.3}$$

The ideal sail is thus found to overestimate peak performance by 8.7%.

B.2 Solar Sail Mass Estimate

Before calculating the second moments of inertia, it is necessary to calculate the location of the centroid. This is normally done as an integral based on the mass of the cross-section. To simplify this, two assumptions are made. First, the cross section is assumed to be made of a material of constant density, which simplifies the calculation from one based on mass to one based on area. Second, a thin-walled assumption is made that allows for the area to be replaced by the linear length. To calculate the overall centroid y_{cm}, the centroids of the web $y_{\mathrm{cm,W}}$ and the flange $y_{\mathrm{cm,F}}$ are calculated separately and then combined. The necessary basic dimensions are provided as Table B.1 and correspond to the cross section of Fig. B.1.

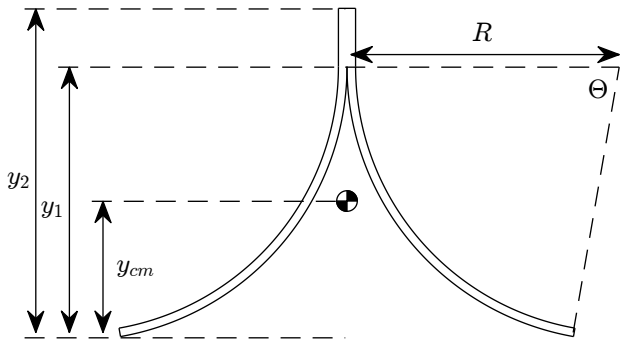

Figure B.1: TRAC Boom Cross Section

Table B.1: Required Cross Section Dimensions

Dimension	Value	Notes
y_1	0.0775 m	
y_2	0.0945 m	
Θ	80 deg	Approximate value provided in personal correspondence
R	0.0787 m	Measured to the center of the flange. Add or subtract $\frac{t}{2}$ for inner or outer radius.
t	0.0025 m	

$$
\begin{aligned}
y_{\mathrm{cm,W}} &= \frac{1}{M}\int_0^M y dm \\
&= \frac{1}{A}\int_0^M y dA \\
&= \frac{1}{L_{\mathrm{Web}}}\int_{y_1}^{y_2} y dy \\
&= \frac{1}{y_2 - y_1}\left[\frac{1}{2}y^2\right]_{y_1}^{y_2} \\
&= \frac{1}{2\left(y_2 - y_1\right)}\left(y_2^2 - y_1^2\right) \\
&= 0.0860\,\mathrm{m}
\end{aligned}
\tag{B.4}
$$

$$
\begin{aligned}
y_{\mathrm{cm,F}} &= \frac{1}{M}\int_0^M y dm \\
&= \frac{1}{A}\int_0^M y dA \\
&= y_1 - \frac{1}{L_{\mathrm{Flange}}}\int_0^\Theta R\sin(\theta) R d\theta \\
&= y_1 - \frac{R^2}{2\pi R\frac{\Theta}{2\pi}}\int_0^\Theta \sin(\theta) d\theta \\
&= y_1 - \frac{R}{\Theta}\left[-\cos(\theta)\right]_0^\Theta \\
&= y_1 - \frac{R}{\Theta}\left[-\cos(\theta)\right]_0^\Theta \\
&= y_1 + \frac{R}{\Theta}\left(\cos(\theta) - 1\right) \\
&= 0.0309\,\mathrm{m}
\end{aligned}
\tag{B.5}
$$

To combine the values of Eq. B.4 and B.5, they must be weighted by the mass of their individual components. Since a constant density and thickness is assumed, this simplifies to just their lengths.

$$
L_{\mathrm{Web}} = y_2 - y_1 = 0.0170\,\mathrm{m} \tag{B.6}
$$

$$
L_{\mathrm{Flange}} = (2\pi R)\frac{\theta}{2\pi} = R\theta = 0.1099\,\mathrm{m} \tag{B.7}
$$

$$
\begin{aligned}
y_{\mathrm{cm}} &= \frac{L_{\mathrm{Web}}}{L_{\mathrm{Web}} + L_{\mathrm{Flange}}} y_{\mathrm{cm,W}} + \frac{L_{\mathrm{Flange}}}{L_{\mathrm{Web}} + L_{\mathrm{Flange}}} y_{\mathrm{cm,F}} \\
&= 0.0383\,\mathrm{m}
\end{aligned}
\tag{B.8}
$$

Before calculating the second moments of area, a number of derived quantities must be solved for. The first of these are the inner and outer radii of the flange: r_1 and r_2.

$$
r_1 = R - \frac{t}{2} = 0.0774\,\mathrm{m} \tag{B.9}
$$

$$
r_2 = R + \frac{t}{2} = 0.0799\,\mathrm{m} \tag{B.10}
$$

Next, the heights of the web and flange must be recalculated with respect to the centroid rather than the bottom of the cross section.

$$
h_1 = y_1 - y_{cm} = 0.0392\,\mathrm{m} \tag{B.11}
$$

$$h_2 = y_2 - y_{cm} = 0.0562\,\mathrm{m} \tag{B.12}$$

The final quantity is the length of the web L_{web}. This was previously solved for in Eq. B.4 and is 0.0170 m.

With the location of the centroid and these derived quantities now available, the second moments of area I_{xx} and I_{yy} are calculated. Starting with the second moments of area with respect to the x-axis for the web $I_{xx,W}$ and flange $I_{xx,F}$

$$\begin{aligned}
I_{xx,W} &= \int_0^A x^2 dA \\
&= \int_{h_1}^{h_2} \int_{-t}^{t} y^2 dl dy \\
&= \int_{h_1}^{h_2} \left[y^2 l\right]_{-t}^{t} dy \\
&= \int_{h_1}^{h_2} y^2 \left(t - (-t)\right) dy \\
&= \int_{h_1}^{h_2} 2y^2 t dy \\
&= \left[\frac{2}{3} r^3 t\right]_{h_1}^{h_2} \\
&= \frac{2}{3}\left(h_2^3 - h_1^3\right) t \\
&= 1.9543 \times 10^{-7}\,\mathrm{m}^4
\end{aligned} \tag{B.13}$$

$$
\begin{aligned}
I_{xx,F} &= \int_0^A x^2 dA \\
&= 2\int_0^{\Theta}\int_{r_1}^{r_2} \left(h_1 - r\sin\left(\theta\right)\right)^2 r dr d\theta \\
&= 2\int_0^{\Theta}\int_{r_1}^{r_2} \left(h_1^2 - 2h_1 r\sin\left(\theta\right) + r^2\sin^2\left(\theta\right)\right) r dr d\theta \\
&= 2\int_0^{\Theta}\int_{r_1}^{r_2} h_1^2 r - 2h_1 r^2\sin\left(\theta\right) + r^3\sin^2\left(\theta\right) dr d\theta \\
&= 2\int_0^{\Theta}\left[\frac{1}{2}h_1^2 r^2 - \frac{2}{3}h_1 r^3 + \frac{1}{4}r^4\sin^2\left(\theta\right)\right]_{r_1}^{r_2} d\theta \\
&= 2\int_0^{\Theta}\frac{1}{2}h_1^2\left(r_2^2 - r_1^2\right) - \frac{2}{3}h_1\left(r_2^3 - r_1^3\right)\sin\left(\theta\right) + \frac{1}{4}\left(r_2^4 - r_1^4\right)\sin^2\left(\theta\right) d\theta \\
&= 2\left[\frac{1}{2}h_1^2\theta\left(r_2^2 - r_1^2\right) + \frac{2}{3}h_1\left(r_2^3 - r_1^3\right)\cos\left(\theta\right) + \frac{1}{8}\left(r_2^4 - r_1^4\right)\left(\theta - \sin\left(\theta\right)\cos\left(\theta\right)\right)\right]_0^{\Theta} \\
&= 2\left(\frac{1}{2}h_1^2\Theta\left(r_2^2 - r_1^2\right) + \frac{2}{3}h_1\left(r_2^3 - r_1^3\right)\left(\cos\left(\Theta\right) - 1\right) + ... \right. \\
&\qquad\qquad \left. \frac{1}{8}\left(r_2^4 - r_1^4\right)\left(\Theta - \sin\left(\Theta\right)\cos\left(\Theta\right)\right)\right) \\
&= 3.3128 \times 10^{-7}\,\mathrm{m}^4
\end{aligned}
\tag{B.14}
$$

the overall value I_{xx} is found.

$$
I_{xx} = I_{xx,W} + I_{xx,F} = 5.2671 \times 10^{-8}\,\mathrm{m}^4 \tag{B.15}
$$

This is then repeated for $I_{yy,W}$ and $I_{yy,F}$

$$
\begin{aligned}
I_{yy,W} &= \int_0^A x^2 dA \\
&= \int_{-t}^{t} \int_0^{L_{\text{Web}}} x^2 dl dx \\
&= \int_{-t}^{t} \left[x^2 l\right]_0^{L_{\text{Web}}} dx \\
&= \int_{-t}^{t} x^2 L_{\text{Web}} dx \\
&= \left[\frac{1}{3} x^3 L_{\text{Web}}\right]_{-t}^{t} \\
&= \frac{1}{3}\left(t^3 - (-t)^3\right) L_{\text{Web}} \\
&= \frac{2}{3} t^3 L_{\text{Web}} \\
&= 1.7708 \times 10^{-10}\,\text{m}^4
\end{aligned}
\tag{B.16}
$$

$$
\begin{aligned}
I_{yy,F} &= \int_0^A x^2 dA \\
&= 2\int_0^{\Theta} \int_{r_1}^{r_2} \left(r_2 - r\cos(\theta)\right)^2 r dr d\theta \\
&= 2\int_0^{\Theta} \int_{r_1}^{r_2} r_2^2 r - 2 r_2 r^2 \cos(\theta) + r^3 \cos^2(\theta) dr d\theta \\
&= 2\int_0^{\Theta} \left[\frac{1}{2} r_2^2 r^2 - \frac{2}{3} r_2 r^3 \cos(\theta) + \frac{1}{4} r^4 \cos^2(\theta)\right]_{r_1}^{r_2} d\theta \\
&= 2\int_0^{\Theta} \frac{1}{2} r_2^2 \left(r_2^2 - r_1^2\right) - \frac{2}{3} r_2 \left(r_2^3 - r_1^3\right)\cos(\theta) + \frac{1}{4}\left(r_2^4 - r_1^4\right)\cos^2(\theta) d\theta \\
&= 2\left[\frac{1}{2} r_2^2 \theta \left(r_2^2 - r_1^2\right) - \frac{2}{3} r_2 \left(r_2^3 - r_1^3\right)\sin(\theta) + \frac{1}{8}\left(r_2^4 - r_1^4\right)\left(\theta + \sin(\theta)\cos(\theta)\right)\right]_0^{\theta} \\
&= 2\left(\frac{1}{2} r_2^2 \Theta \left(r_2^2 - r_1^2\right) - \frac{2}{3} r_2 \left(r_2^3 - r_1^3\right)\sin(\Theta) + \ldots \right. \\
&\qquad \left. \frac{1}{8}\left(r_2^4 - r_1^4\right)\left(\Theta + \sin(\Theta)\cos(\Theta)\right)\right) \\
&= 5.4529 \times 10^{-7}\,\text{m}^4
\end{aligned}
\tag{B.17}
$$

Which are added together to find I_{yy}.

$$
I_{yy} = I_{yy,W} + I_{yy,F} = 5.4547 \times 10^{-7}\,\text{m}^4 \tag{B.18}
$$

Appendix C

ISO Flyby Master Equipment Lists

Table C.1: MEL for a Ballistic Spacecraft - Engelhardt and Hoover

Subsystem	Basic Mass (kg)	Growth Allowance	Predicted Mass (kg)	Notes and References
Structural	23	20%	27.1	Set to 25% of CBE Dry Mass
Solar Arrays	32	25%	40.0	Rigid Arrays $\sim$60 W kg^{-1}, Flexible $\sim$150 W kg^{-1} at 1 au [124]. Assume 100 W kg^{-1} = 10 kg kW^{-1}. Full 350 W power at 3 au
Batteries	8	20%	9.6	1000 W h batteries at 120 W h kg^{-1}
Command and Data Handling	5	20%	6.0	Based on JUMPER [108]
Telecom	20	20%	24.0	JUMPER $\sim$6 kg [108], Sunada [109] $\sim$33 kg
Thermal	10	30%	13.0	Based on Sunada [109]
ADCS	25	30%	32.5	Based on Sunada [109].
Harness	8	60%	12.8	
Instrumentation	20	40%	28.0	JUMPER total instrumentation <13 kg [108]; Solar Orbiter Magnetometer Sensor Mass 0.5 kg, METIS Coronograph 24.55 kg [137]
Dry Mass	151		193.0	
Margin		30%	45.2	Per AIAA S-120A-2015 [112]
Allocated Dry Mass			238.2	
Total Mass			238.2	

Table C.2: MEL for an SEP Spacecraft using a Hall-effect Thruster (XR-5) - Engelhardt

Subsystem	Basic Mass (kg)	Growth Allowance	Predicted Mass (kg)	Notes and References
Structural	46	20%	55.1	Set to 25% of CBE Dry Mass
Solar Arrays	71	25%	88.8	Rigid Arrays $\sim$60 W kg^{-1}, Flexible $\sim$150 W kg^{-1} at 1 au [124]. Assume 100 W kg^{-1} = 10 kg kW^{-1}. Full power at 2 au
Batteries	8	20%	9.6	1000 W h batteries at 120 W h kg^{-1}
Command and Data Handling	5	20%	6.0	Based on JUMPER [108]
Telecom	20	20%	24.0	JUMPER $\sim$6 kg [108], Sunada [109] $\sim$33 kg
Thermal	10	30%	13.0	Based on Sunada [109]
ADCS	25	30%	32.5	Based on Sunada [109].
Harness	16	60%	25.6	
PPU, PDU, and Chassis	37	20%	44.4	1 extra PPU and thruster.
Thrusters and Tank.	48	20%	57.6	2 thrusters: 1 primary and 1 backup. 12.3 kg per thruster [105]. Tank set to 7.5% of Prop. Mass
Instrumentation	20	40%	28.0	JUMPER total instrumentation <13 kg [108]; Solar Orbiter Magnetometer Sensor Mass 0.5 kg, METIS Coronograph 24.55 kg [137]
Dry Mass	306		384.5	
Margin		30%	91.8	Per AIAA S-120A-2015 [112]
Allocated Dry Mass			476.3	
Xenon Propellant Mass			307.1	Expected 2σ Upper Bound on Prop Usage
RCS Propellant Mass			8.0	1% of total wet mass
Total Wet Mass			791.4	

Table C.3: MEL for an SEP Spacecraft using a Hall-effect Thruster (XR-5) - Hoover

Subsystem	Basic Mass (kg)	Growth Allowance	Predicted Mass (kg)	Notes and References
Structural	39	20%	47.0	Set to 25% of CBE Dry Mass
Solar Arrays	51	25%	63.8	Rigid Arrays $\sim$60 W kg^{-1}, Flexible $\sim$150 W kg^{-1} at 1 au [124]. Assume 100 W kg^{-1} = 10 kg kW^{-1}. Full power at 2 au
Harness	12	60%	19.2	
Thrusters and Tank.	34	20%	40.8	2 thrusters: 1 primary and 1 backup. 12.3 kg per thruster [105]. Tank set to 7.5% of Prop. Mass
Instrumentation	20	40%	28.0	JUMPER total instrumentation <13 kg [108]; Solar Orbiter Magnetometer Sensor Mass 0.5 kg, METIS Coronograph 24.55 kg [137]
All Other Systems	105	Varies	129.5	Other systems unchanged from Table C.2
Dry Mass	261		328.3	
Margin		30%	78.4	Per AIAA S-120A-2015 [112]
Allocated Dry Mass			406.6	
Xenon Propellant Mass			121.9	Expected 2σ Upper Bound on Prop Usage
RCS Propellant Mass			5.0	1% of total wet mass
Total Wet Mass			533.5	

Table C.4: MEL for an SEP Spacecraft using a Gridded Ion Thruster (NEXT-C) - Engelhardt

Subsystem	Basic Mass (kg)	Growth Allowance	Predicted Mass (kg)	Notes and References
Structural	64	20%	76.4	Set to 25% of CBE Dry Mass
Solar Arrays	136	25%	170.0	Rigid Arrays $\sim$60 W kg^{-1}, Flexible $\sim$150 W kg^{-1} at 1 au [124]. Assume 100 W kg^{-1} = 10 kg kW^{-1}. Full power at 2 au
Batteries	8	20%	9.6	1000 W h batteries at 120 W h kg^{-1}
Command and Data Handling	5	20%	6.0	Based on JUMPER [108]
Telecom	20	20%	24.0	JUMPER $\sim$6 kg [108], Sunada [109] $\sim$33 kg
Thermal	10	30%	13.0	Based on Sunada [109]
ADCS	25	30%	32.5	Based on Sunada [109].
Harness	29	60%	46.4	
PPU, PDU, and Chassis	69	20%	82.8	1 extra PPU and thruster.
Thrusters and Tank	39	20%	46.8	2 thrusters: 1 primary and 1 backup. 12.3 kg per thruster [105]. Tank set to 7.5% of Prop. Mass
Instrumentation	20	40%	28.0	JUMPER total instrumentation <13 kg [108]; Solar Orbiter Magnetometer Sensor Mass 0.5 kg, METIS Coronograph 24.55 kg [137]
Dry Mass	425		535.5	
Margin		30%	127.4	Per AIAA S-120A-2015 [112]
Allocated Dry Mass			663.0	
Xenon Propellant Mass			145.3	Expected 2σ Upper Bound on Prop Usage
RCS Propellant Mass			8.0	1% of total wet mass
Total Wet Mass			816.3	

Table C.5: MEL for an SEP Spacecraft using a Gridded Ion Thruster (NEXT-C) - Hoover

Subsystem	Basic Mass (kg)	Growth Allowance	Predicted Mass (kg)	Notes and References
Structural	58	20%	69.7	Set to 25% of CBE Dry Mass
Solar Arrays	114	25%	142.5	Rigid Arrays $\sim$60 W kg^{-1}, Flexible $\sim$150 W kg^{-1} at 1 au [124]. Assume 100 W kg^{-1} = 10 kg kW^{-1}. Full power at 2 au
Harness	25	60%	40.0	
Thrusters and Tank	33	20%	39.6	2 thrusters: 1 primary and 1 backup. 12.3 kg per thruster [105]. Tank set to 7.5% of Prop. Mass
All Other Systems	157	Varies	195.9	Other systems unchanged from Table C.4.
Dry Mass	387		487.7	
Margin		30%	116.1	Per AIAA S-120A-2015 [112]
Allocated Dry Mass			603.8	
Xenon Propellant Mass			56.1	Expected 2σ Upper Bound on Prop Usage
RCS Propellant Mass			7.0	1% of total wet mass
Total Wet Mass			666.9	

Table C.6: MEL for a Spacecraft using Bipropellant Propulsion - Engelhardt

Subsystem	Basic Mass (kg)	Growth Allowance	Predicted Mass (kg)	Notes and References
Structural	38	20%	45.6	Set to 25% of CBE Dry Mass
Solar Arrays	32	25%	40.0	Rigid Arrays $\sim$60 W kg^{-1}, Flexible $\sim$150 W kg^{-1} at 1 au [124]. Assume 100 W kg^{-1} = 10 kg kW^{-1}. Full power at 2 au
Batteries	8	20%	9.6	1000 W h batteries at 120 W h kg^{-1}
Command and Data Handling	5	20%	6.0	Based on JUMPER [108]
Telecom	20	20%	24.0	JUMPER $\sim$6 kg [108], Sunada [109] $\sim$33 kg
Thermal	10	30%	13.0	Based on Sunada [109]
ADCS	25	30%	32.5	Based on Sunada [109].
Harness	8	60%	12.8	
Bipropellant System	87.5	20%	104.9	15% of Propellant Mass
Instrumentation	20	40%	28.0	JUMPER total instrumentation <13 kg [108]; Solar Orbiter Magnetometer Sensor Mass 0.5 kg, METIS Coronograph 24.55 kg [137]
Dry Mass	253.5		316.5	
Margin		30%	76.0	Per AIAA S-120A-2015 [112]
Allocated Dry Mass			392.5	
Xenon Propellant Mass			583.0	Expected 2σ Upper Bound on Prop Usage
RCS Propellant Mass			10.0	1% of total wet mass
Total Wet Mass			985.5	

Table C.7: MEL for a Spacecraft using Bipropellant Propulsion - Hoover

Subsystem	Basic Mass (kg)	Growth Allowance	Predicted Mass (kg)	Notes and References
Structural	36	20%	43.8	Set to 25% of CBE Dry Mass
Bipropellant System	78	20%	93.4	15% of Propellant Mass
All Other Systems	128	40%	165.7	Other systems unchanged from Table C.6.
Dry Mass	242		302.9	
Margin		30%	72.7	Per AIAA S-120A-2015 [112]
Allocated Dry Mass			375.6	
Xenon Propellant Mass			519.0	Expected 2σ Upper Bound on Prop Usage
RCS Propellant Mass			9.0	1% of total wet mass
Total Wet Mass			903.6	

Table C.8: MEL for Solar Sail Spacecraft - Engelhardt and Hoover

Subsystem	Basic Mass (kg)	Growth Allowance	Predicted Mass (kg)	Notes and References
Structural	12	20%	38.1	Set to 25% of CBE Dry Mass
Solar Arrays	32	25%	40.0	Rigid Arrays $\sim$60 W kg^{-1}, Flexible $\sim$150 W kg^{-1} at 1 au [124]. Assume 100 W kg^{-1} = 10 kg kW^{-1}. Full power at 2 au
Batteries	8	20%	9.6	1000 W h batteries at 120 W h kg^{-1}
Command and Data Handling	5	20%	6.0	Based on JUMPER [108]
Telecom	20	20%	24.0	JUMPER $\sim$6 kg [108], Sunada [109] $\sim$33 kg
Thermal	10	30%	13.0	Based on Sunada [109]
ADCS	25	30%	32.5	Based on Sunada [109].
Harness	8	60%	12.8	
Solar Sail	52	20%	62.4	HISM 7000 m^2 Sail Concept [99]
Instrumentation	20	40%	28.0	JUMPER total instrumentation <13 kg [108]; Solar Orbiter Magnetometer Sensor Mass 0.5 kg, METIS Coronograph 24.55 kg [137]
Dry Mass	212		266.4	
Margin		30%	63.5	Per AIAA S-120A-2015 [112]
Allocated Dry Mass			329.9	
Total Mass			329.9	

Table C.9: MEL for Hybrid Low-Thrust Spacecraft - Engelhardt

Subsystem	Basic Mass (kg)	Growth Allowance	Predicted Mass (kg)	Notes and References
Structural	58	20%	69.5	Set to 25% of CBE Dry Mass
Solar Arrays	82	25%	102.5	Rigid Arrays $\sim$60 $\mathrm{W\,kg^{-1}}$, Flexible $\sim$150 $\mathrm{W\,kg^{-1}}$ at 1 au [124]. Assume 100 $\mathrm{W\,kg^{-1}}$ = 10 $\mathrm{kg\,kW^{-1}}$. Full power at 2 au
Batteries	8	20%	9.6	1000 W h batteries at 120 $\mathrm{W\,h\,kg^{-1}}$
Command and Data Handling	5	20%	6.0	Based on JUMPER [108]
Telecom	20	20%	24.0	JUMPER $\sim$6 kg [108], Sunada [109] $\sim$33 kg
Thermal	10	30%	13.0	Based on Sunada [109]
ADCS	25	30%	32.5	Based on Sunada [109].
Harness	18	60%	28.8	
PPU, PDU, and Chassis	37	20%	44.4	1 extra PPU and thruster.
Thrusters and Tank.	51	20%	61.2	2 thrusters: 1 primary and 1 backup. 12.3 kg per thruster [105]. Tank set to 7.5% of Prop. Mass
Solar Sail	52	20%	62.4	HISM 7000 $\mathrm{m^2}$ Sail Concept [99]
Instrumentation	20	40%	28.0	JUMPER total instrumentation <13 kg [108]; Solar Orbiter Magnetometer Sensor Mass 0.5 kg, METIS Coronograph 24.55 kg [137]
Dry Mass	386		481.9	
Margin		30%	115.8	Per AIAA S-120A-2015 [112]
Allocated Dry Mass			597.6	
Xenon Propellant Mass			341.0	Expected 2σ Upper Bound on Prop Usage
RCS Propellant Mass			9.0	1% of total wet mass
Total Mass			947.6	

Table C.10: MEL for Hybrid Low-Thrust Spacecraft - Hoover

Subsystem	Basic Mass (kg)	Growth Allowance	Predicted Mass (kg)	Notes and References
Structural	53	20%	63.3	Set to 25% of CBE Dry Mass
Solar Arrays	71	25%	88.8	Rigid Arrays $\sim$60 W kg^{-1}, Flexible $\sim$150 W kg^{-1} at 1 au [124]. Assume 100 W kg^{-1} = 10 kg kW^{-1}. Full power at 2 au
Harness	16	60%	25.6	
Thrusters and Tank	35	20%	42.0	2 thrusters: 1 primary and 1 backup. 12.3 kg per thruster [105]. Tank set to 7.5% of Prop. Mass
All Other Systems	177	Varies	219.9	
Dry Mass	352		439.6	
Margin		30%	105.5	Per AIAA S-120A-2015 [112]
Allocated Dry Mass			545.1	
Xenon Propellant Mass			137.4	Expected 2σ Upper Bound on Prop Usage
RCS Propellant Mass			7.0	1% of total wet mass
Total Mass			689.5	

Bibliography

[1] L. Johnson and F. Curran, "*Solar Cruiser* Technology Maturation Plans," techreport, National Aeronautics and Astronautics Administration (NASA), July 2020.

[2] G. D. Racca, A. Marini, L. Stagnaro, J. van Dooren, L. di Napoli, B. H. Foing, R. Lumb, J. Volp, J. Brinkmann, R. Grünagel, D. Estublier, E. Tremolizzo, M. McKay, O. Camino, J. Schoemaekers, M. Hechler, M. Khan, P. Rathsman, G. Andersson, K. Anflo, S. Berge, P. Bodin, A. Edfors, A. Hussain, J. Kugelberg, N. Larsson, B. Ljung, L. Meijer, A. Mörtsell, T. Nordebäck, S. Persson, and F. Sjöberg, "SMART-1 mission description and development status," *Planetary and Space Science*, vol. 50, pp. 1323–1337, dec 2002.

[3] *Standard: Mass Properties Control for Space Systems (ANSI/AIAA S-120A-2015)*. American Institute of Aeronautics and Astronautics, Inc., jan 2015.

[4] L. Prockter, S. Murchie, A. Cheng, S. Krimigis, R. Farquhar, A. Santo, and J. Trombka, "The NEAR shoemaker mission to asteroid 433 eros," *Acta Astronautica*, vol. 51, pp. 491–500, jul 2002.

[5] J. Veverka, P. Thomas, A. Harch, B. Clark, J. F. Bell, B. Carcich, J. Joseph, S. Murchie, N. Izenberg, C. Chapman, W. Merline, M. Malin, L. McFadden, and M. Robinson, "NEAR Encounter with Asteroid 253 Mathilde: Overview," *Icarus*, vol. 140, pp. 3–16, July 1999.

[6] T. C. Duxbury, R. L. Newburn, C. H. Acton, E. Carranza, T. P. McElrath, R. E. Ryan, S. P. Synnott, T. H. You, D. E. Brownlee, A. R. Cheuvront, W. R. Adams, S. L. Toro-Allen, S. Freund, K. V. Gilliland, K. J. Irish, C. R. Love, J. G. McAllister, S. J. Mumaw, T. H. Oliver, and D. E. Perkins, "Asteroid 5535 Annefrank size, shape, and orientation: Stardust first results," *Journal of Geophysical Research: Planets*, vol. 109, pp. n/a–n/a, feb 2004.

[7] T. C. Duxbury, R. L. Newburn, and D. E. Brownlee, "Comet 81P/Wild 2 size, shape, and orientation," *Journal of Geophysical Research: Planets*, vol. 109, Dec. 2004.

[8] D. E. Brownlee, "Stardust: Comet and interstellar dust sample return mission," *Journal of Geophysical Research*, vol. 108, no. E10, 2003.

[9] T. Morley, F. Budnik, M. Croon, and B. Godard, "Rosetta navigation for the fly-by of asteroid 21 Lutetia," in *Proceedings 23rd International Symposium on Space Flight Dynamics-23rd ISSFD, Pasadena, USA*, 2012.

[10] M. A. Barucci, M. Fulchignoni, J. Ji, S. Marchin, and N. Thomas, *The Flybys of Asteroids 2867 Steins, 21 Lutetia, and 4179 Toutatis*, ch. Part 3: Space Missions, pp. 433–450. University of Arizona Press, 2015.

[11] D. S. Nelson, F. J. Pelletier, M. W. Buie, J. A. Bauman, J. T. Fischetti, Y. Guo, S. D. J. Gwyn, M. E. Holdridge, J. J. Kavelaars, E. J. Lessac-Chenen, C. B. Olkin, J. Y. Pelgrift, S. B. Porter, G. D. Rogers, M. J. Salinas, J. R. Spencer, D. R. Stanbridge, S. A. Stern, H. A. Weaver, B. G. Williams, and K. E. Williams, "Navigation and Orbit Estimation for New Horizons' Arrokoth Flyby: Overview, Results and Lessons Learned," *Space Science Reviews*, vol. 218, mar 2022.

[12] J. Cao, Y. Liu, S. Hu, L. Liu, G. Tang, Y. Huang, and P. Li, "Navigation of Chang'E-2 asteroid exploration mission and the minimum distance estimation during its fly-by of Toutatis," *Advances in Space Research*, vol. 55, pp. 491–500, jan 2015.

[13] R. S. Hudson, S. J. Ostro, and D. J. Scheeres, "High-resolution model of Asteroid 4179 Toutatis," *Icarus*, vol. 161, pp. 346–355, Feb. 2003.

[14] A. Heaton, N. Ahmad, and K. Miller, "Near Earth Asteroid Scout Thrust and Torque Model," in *International Symposium on Solar Sailing (ISSS 2017)*, no. M17-5721, 2017.

[15] F. O'Donnell, "Mariner 2 and beyond-planetary exploration's first 25 years," *IEEE Aerospace Electronic Systems Magazine*, vol. 2, pp. 2–6, 1987.

[16] G. H. Born, E. H. Christensen, A. J. Ferrari, J. F. Jordan, and S. J. Reinbold, "The Determination of the Satellite Orbit of Mariner 9," *Celestial Mechanics*, vol. 9, pp. 395–414, May 1974.

[17] E. K. Davis, "Mariner 10 Mission Support," in *The Deep Space Network Progress Report 42-26*, pp. 5–7, National Aeronautics and Space Administration, 1975.

[18] D. Lev, R. M. Myers, K. M. Lemmer, J. Kolbeck, H. Koizumi, and K. Polzin, "The technological and commercial expansion of electric propulsion," *Acta Astronautica*, vol. 159, pp. 213 – 227, 2019.

[19] J. S. Snyder, V. H. Chaplin, D. M. Goebel, R. R. Hofer, A. Lopez Ortega, I. G. Mikellides, T. Kerl, G. Lenguito, F. Aghazadeh, and I. Johnson, "Electric Propulsion for the Psyche Mission: Development Activities and Status," in *AIAA Propulsion and Energy 2020 Forum*, p. 3607, 2020.

[20] J. Heiligers, J. M. Fernandez, O. R. Stohlman, and W. K. Wilkie, "Trajectory design for a solar-sail mission to asteroid 2016 HO3," *Astrodynamics*, vol. 3, pp. 231–246, Sept. 2019.

[21] C. R. McInnes, *Solar Sailing*. London: Springer London, 1999.

[22] Y. Tsuda, O. Mori, R. Funase, H. Sawada, T. Yamamoto, T. Saiki, T. Endo, K. Yonekura, H. Hoshino, and J. Kawaguchi, "Achievement of IKAROS — japanese deep space solar sail demonstration mission," *Acta Astronautica*, vol. 82, pp. 183–188, feb 2013.

[23] J. Dervan, "Solar & Electric Sailing Overview: KISS Technology Development Workshop (May 15-18, 2018)." May 2018.

[24] L. McNutt, L. Johnson, P. Kahn, J. Castillo-Rogez, and A. Frick, "Near-Earth Asteroid (NEA) Scout," in *AIAA SPACE 2014 Conference and Exposition*, American Institute of Aeronautics and Astronautics, Aug. 2014.

[25] K. Chang, "Small explorers hitched a ride to space with Artemis I," *The New York Times*, Nov. 2022. Published Electronically.

[26] L. Johnson and E. E. Montgomery, "Earth to Orbit Beamed Energy Experiment," in *Proceedings of the 68th International Astronautical Congress (IAC), Adelaide, Australia, 25-29 September 2017*, International Astronautical Federal (IAF), Sept. 2017.

[27] J. Foust, "Deep space smallsats face big challenges," *SpaceNews*, Feb. 2023.

[28] J. B. Pezent, R. Sood, A. Heaton, K. Miller, and L. Johnson, "Preliminary trajectory design for NASA's Solar Cruiser: A technology demonstration mission," *Acta Astronautica*, vol. 183, pp. 134–140, jun 2021.

[29] L. Johnson, C. Diaz, L. McNutt, D. Tyler, D. Wallace, and J. Wilson, "The NASA Solar Cruiser Solar Sail System – Ready for Heliophysics and Deep Space Missions," in *Proceedings of the 6th international Symposium on Space Sailing, June 5-9, 2023, New York, NY USA*, June 2023.

[30] C. Biddy and T. Svitek, "LightSail-1 Solar Sail Design and Qualification," in *Proceedings of the 41st Aerospace Mechanisms Symposium, Jet Propulsion Laboratory, May 16-18, 2012* (E. A. Boesiger, ed.), pp. 451–463, Jet Propulsion Laboratory, May 2012.

[31] G. Vulpetti, L. Johnson, and G. L. Matloff, "The NanoSAIL-d2 NASA mission," in *Solar Sails*, pp. 173–178, Springer New York, sep 2014.

[32] Y. Tsuda, O. Mori, R. Funase, H. Sawada, T. Yamamoto, T. Saiki, T. Endo, and J. Kawaguchi, "Flight status of IKAROS deep space solar sail demonstrator," *Acta Astronautica*, vol. 69, pp. 833–840, nov 2011.

[33] J. Heiligers, B. Diedrich, W. Derbes, and C. McInnes, "Sunjammer: Preliminary End-to-End Mission Design," in *AIAA/AAS Astrodynamics Specialist Conference*, American Institute of Aeronautics and Astronautics, aug 2014.

[34] D. Leone, "NASA Nixes Sunjammer Mission, Cites Integration, Schedule Risk." Electronically, Oct. 2014. SpaceNews.

[35] D. A. Spencer, B. Betts, J. M. Bellardo, A. Diaz, B. Plante, and J. R. Mansell, "The LightSail 2 solar sailing technology demonstration," *Advances in Space Research*, vol. 67, pp. 2878–2889, may 2021.

[36] L. Johnson, J. Castillo-Rogez, J. Dervan, and L. McNutt, "Near Earth Asteroid (NEA) Scout," in *Proccedings of the Fourth International Symposium on Solar Sailing (ISSS 2017)*, Jan. 2017.

[37] S. Gong, J. Li, and F. Jiang, "Interplanetary trajectory design for a hybrid propulsion system," *Aerospace Science and Technology*, vol. 45, pp. 104–113, sep 2015.

[38] M. Macdonald and C. McInnes, "Solar Sail Mission Applications and Future Advancement," in *Proceedings of the Second Symposium on Solar Sailing, July 2010*, July 2010.

[39] G. Mengali and A. A. Quarta, "Trajectory design with hybrid low-thrust propulsion system," *Journal of Guidance, Control, and Dynamics*, vol. 30, pp. 419–426, mar 2007.

[40] M. Leipold and M. Götz, "Hybrid photonic/electric propulsion," *Kayser-Threde GmbH, Technical Report SOL4-TR-KTH-0001, ESA contract*, no. 15334/01, 2002.

[41] G. Mengali and A. A. Quarta, "Tradeoff Performance of Hybrid Low-Thrust Propulsion System," *Journal of Spacecraft and Rockets*, vol. 44, pp. 1263–1270, nov 2007.

[42] T. Li, Z. Wang, and Y. Zhang, "Multi-objective trajectory optimization for a hybrid propulsion system," *Advances in Space Research*, vol. 62, pp. 1102–1113, sep 2018.

[43] D. Miller, J. Englander, and R. Linares, "Hybrid Solar Sailing and Electric Propulsion: A Mission Concept to Comet 45P," in *2021 AAS/AIAA Astrodynamics Specialist Conference, Big Sky, Virtual, August 9-11, 2021*, American Astronautical Association, Univelt, Aug. 2021.

[44] S. Baig and C. R. McInnes, "Artificial Three-Body Equilibria for Hybrid Low-Thrust Propulsion," *Journal of Guidance, Control, and Dynamics*, vol. 31, pp. 1644–1655, nov 2008.

[45] M. Ceriotti and C. R. McInnes, "Generation of Optimal Trajectories for Earth Hybrid Pole Sitters," *Journal of Guidance, Control, and Dynamics*, vol. 34, pp. 847–859, may 2011.

[46] M. Ceriotti and C. R. McInnes, "Systems design of a hybrid sail pole-sitter," *Advances in Space Research*, vol. 48, pp. 1754–1762, dec 2011.

[47] M. Ceriotti and C. R. McInnes, "Hybrid solar sail and solar electric propulsion for novel earth observation missions," *Acta Astronautica*, vol. 69, pp. 809–821, nov 2011.

[48] M. Ceriotti, J. Heiligers, and C. R. McInnes, "Trajectory and Spacecraft Design for a Pole-Sitter Mission," *Journal of Spacecraft and Rockets*, vol. 51, pp. 311–326, jan 2014.

[49] J. Heiligers, T. D. van den Oever, M. Ceriotti, P. Mulligan, and C. R. McInnes, "Continuous Planetary Polar Observation from Hybrid Pole-Sitters at Venus, Earth, and Mars," in *Fourth International Symposium on Solar Sailing (ISSS 2017), Kyoto, Japan, 17-20 Jan*, Jan. 2017.

[50] J. Heiligers, M. Ceriotti, C. R. McInnes, and J. D. Biggs, "Displaced Geostationary Orbit Design Using Hybrid Sail Propulsion," *Journal of Guidance, Control, and Dynamics*, vol. 34, pp. 1852–1866, nov 2011.

[51] J. Heiligers, C. R. McInnes, J. D. Biggs, and M. Ceriotti, "Displaced geostationary orbits using hybrid low-thrust propulsion," *Acta Astronautica*, vol. 71, pp. 51–67, feb 2012.

[52] Y. Liu, J. Heiligers, and M. Ceriotti, "Loosely-displaced geostationary orbits with hybrid sail propulsion," *Aerospace Science and Technology*, vol. 79, pp. 105–117, aug 2018.

[53] A. R. Davoyan, J. N. Munday, N. Tabiryan, G. A. Swartzlander, and L. Johnson, "Photonic materials for interstellar solar sailing," *Optica*, vol. 8, pp. 722–734, May 2021.

[54] T. W. Murphey and J. Banik, "TRIANGULAR ROLLABLE AND COLLAPSIBLE BOOM," Mar. 2011.

[55] B. C. Given, Emmett and J. Clifton, "NEAR EARTH ASTERIOD SCOUT SOLAR SAIL." Electronically, Jan. 2015. MSFC-1601343.

[56] E. Given, "Near Earth Asteroid Scout Solar Sail." Electronically, Dec. 2015. MSFC-1501505.

[57] D. A. Spencer, L. Johnson, and A. C. Long, "Solar sailing technology challenges," *Aerospace Science and Technology*, vol. 93, p. 105276, oct 2019.

[58] R. Sood and K. Howell, "Solar sail transfers and trajectory design to sun-earth l4, l5: Solar observations and potential earth trojan exploration," *The Journal of the Astronautical Sciences*, vol. 66, pp. 247–281, feb 2019.

[59] A. Farrés, J. Heiligers, and N. Miguel, "Road map to l4/l5 with a solar sail," *Aerospace Science and Technology*, vol. 95, p. 105458, dec 2019.

[60] D. Alexander, A. Sandman, P. Liewer, J. Ayon, B. Goldstein, N. Murphy, M. Velli, L. Floyd, D. Moses, D. Socker, *et al.*, "Solar Polar Imager: Observing Solar Activity from a New Perspective," in *Solar Wind 11/SOHO 16, Connecting Sun and Heliosphere*, vol. 592, p. 663, 2005.

[61] D. E. Trilling, M. Mommert, J. L. Hora, D. Farnocchia, P. Chodas, J. Giorgini, H. A. Smith, S. Carey, C. M. Lisse, M. Werner, A. McNeill, S. R. Chesley, J. P. Emery, G. Fazio, Y. R. Fernandez, A. Harris, M. Marengo, M. Mueller, A. Roegge, N. Smith, H. A. Weaver, K. Meech, and M. Micheli, "Spitzer Observations of Interstellar Object 1I/'Oumuamua," *The Astronomical Journal*, vol. 156, p. 261, nov 2018.

[62] T. Hallatt and P. Wiegert, "The Dynamics of Interstellar Asteroids and Comets within the Galaxy: An Assessment of Local Candidate Source Regions for 1I/'Oumuamua and 2I/Borisov," *The Astronomical Journal*, vol. 159, p. 147, mar 2020.

[63] NSF, "NSF-supported observatory renamed for astronomer Vera C. Rubin." Electronically, Jan. 2020.

[64] T. M. Eubanks, "Is Interstellar Object 2I/Borisov a Stardust Comet? Predictions for the Post Perihelion Period." Submitted to Astrophysical Journal Letters, 2019.

[65] D. Seligman and G. Laughlin, "The Feasibility and Benefits of In Situ Exploration of 'Oumuamua-like Objects," *The Astronomical Journal*, vol. 155, pp. 155–217, apr 2018.

[66] D. Mages, D. Landau, B. Donitz, and S. Bhaskaran, "Navigation evaluation for fast interstellar object flybys," *Acta Astronautica*, vol. 191, pp. 359–373, feb 2022.

[67] A. Hibberd, A. M. Hein, and T. M. Eubanks, "Project Lyra: Catching 1I/'Oumuamua – Mission Opportunities after 2024," *Acta Astronautica*, vol. 170, pp. 136–144, may 2020.

[68] A. Kural, N. Leveque, C. Welch, and P. Wolanski, "Design of an ion thruster movable grid thrust vectoring system," *Acta Astronautica*, vol. 55, pp. 421–432, Aug. 2004.

[69] J. Brophy, "The Dawn Ion Propulsion System," *Space Science Reviews*, vol. 163, pp. 251–261, Nov. 2011.

[70] D. A. Herman, T. Gray, I. Johnson, S. Hussein, and T. Winkelmann, "Development and Qualification Status of the Electric Propulsion Systems for the NASA PPE Mission and Gateway Program," in *Proceedings of the 37th International Electric Propulsion Conference, Boston, MA, United States June 19-23, 2022*, no. IEPC-2022-465, 2022.

[71] "Trajectory," Jan. 2024. https://www.merriam-webster.com/dictionary/trajectory.

[72] Anvil V. Rao, "A Survey of Numerical Methods for Optimal Control," in *Proceedings of the 19th AAS/AIAA Space Flight Mechanics Meeting, Savannah, Georgia*, Feb. 2009.

[73] D. H. Ellison, *Robust Preliminary Design for Multiple Gravity Assist Spacecraft Trajectories*. PhD thesis, University of Illinois at Urbana-Champaign, 2018.

[74] M. Kelly, "An introduction to trajectory optimization: How to do your own direct collocation," *SIAM Review*, vol. 59, pp. 849–904, jan 2017.

[75] M. A. Vavrina, J. A. Englander, and D. H. Ellison, "Global Optimization of N-Maneuver, High-Thrust Trajectories Using Direct Multiple Shooting," in *AAS/AIAA Spaceflight Mechanics Meeting, Napa, CA, February 14-18, 2016*, Feb. 2016.

[76] P. E. Gill, W. Murray, and M. A. Saunders, "SNOPT: An SQP Algorithm for Large-Scale Constrained Optimization," *SIAM Review*, vol. 47, pp. 99–131, jan 2005.

[77] J. T. Betts, *Practical Methods for Optimal Control and Estimation Using Nonlinear Programming*. Society for Industrial and Applied Mathematics, third ed., 2020.

[78] J. Nocedal and S. Wright, *Numerical Optimization*. New York, NY: Springer New York, second ed., 2006.

[79] S. Boyd and L. Vandenberghe, *Convex Optimization*. Cambridge: Cambridge University Press, 2009.

[80] W. Squire and G. Trapp, "Using Complex Variables to Estimate Derivatives of Real Functions," *SIAM Review*, vol. 40, pp. 110–112, Jan. 1998.

[81] R. H. Leary, "Global Optimization on Funneling Landscapes," *Journal of Global Optimization*, vol. 18, no. 4, pp. 367–383, 2000.

[82] B. Addis, A. Cassioli, M. Locatelli, and F. Schoen, "A global optimization method for the design of space trajectories," *Computational Optimization and Applications*, vol. 48, pp. 635–652, June 2009.

[83] M. Vasile, E. Minisci, and M. Locatelli, "Analysis of some global optimization algorithms for space trajectory design," *Journal of Spacecraft and Rockets*, vol. 47, pp. 334–344, Mar. 2010.

[84] C. H. Yam, D. D. Lorenzo, and D. Izzo, "Low-thrust trajectory design as a constrained global optimization problem," *Proceedings of the Institution of Mechanical Engineers, Part G: Journal of Aerospace Engineering*, vol. 225, pp. 1243–1251, Aug. 2011.

[85] J. Englander, *AUTOMATED TRAJECTORY PLANNING FOR MULTIPLE-FLYBY INTERPLANETARY MISSIONS*. phdthesis, University of Illinois at Urbana-Champaign, 2013.

[86] J. A. Englander, M. A. Vavrina, and A. R. Ghosh, "Multi-objective hybrid optimal control for multiple-flyby low-thrust mission design," in *AAS/AIAA Space Flight Mechanics Meeting, Williamsburg, VA, January 11-15, 2015*, Jan. 2015.

[87] M. Berry and L. Healy, "The generalized sundman transformation for propagation of high-eccentricity elliptical orbits," tech. rep., NAVAL RESEARCH LAB WASHINGTON DC, 2002.

[88] A. Reuther, J. Kepner, C. Byun, S. Samsi, W. Arcand, D. Bestor, B. Bergeron, V. Gadepally, M. Houle, M. Hubbell, M. Jones, A. Klein, L. Milechin, J. Mullen, A. Prout, A. Rosa, C. Yee, and P. Michaleas, "Interactive Supercomputing on 40,000 Cores for Machine Learning and Data Analysis," in *2018 IEEE High Performance extreme Computing Conference (HPEC)*, pp. 1–6, IEEE, IEEE, sep 2018.

[89] E. Taheri, "Low-Thrust Trajectory Design Using Multi-Mode Propulsion Systems: A Grid-Based Thruster Model," in *AIAA Scitech 2020 Forum*, American Institute of Aeronautics and Astronautics, jan 2020.

[90] R. Gershman and C. Seybold, "Propulsion trades for space science missions," *Acta Astronautica*, vol. 45, pp. 541–548, aug 1999.

[91] O. Mori, J. Matsumoto, T. Chujo, M. Matsushita, H. Kato, T. Saiki, Y. Tsuda, J. Kawaguchi, F. Terui, Y. Mimasu, G. Ono, N. Ogawa, Y. Takao, Y. Kubo, K. Ohashi, A. K. Sugihara, T. Okada, T. Iwata, and H. Yano, "Solar power sail mission of OKEANOS," *Astrodynamics*, vol. 4, pp. 233–248, oct 2019.

[92] D. Landau, B. Donitz, and R. Karimi, "Near-term strategies to rendezvous with an interstellar object," *Acta Astronautica*, vol. 206, pp. 133–143, may 2023.

[93] Z. McConnel, B. Sanders, A. Takroori, C. Hazelton, J. Pearson, C. Diaz, and A. Benson, "Test of a Full-Scale Quadrant for the $1,653m^2$ Solar Cruiser Sail," in *Proceedings of the 6th International Symposium on Space Sailing (ISSS-2023), New York, USA, 5-9 June 2023*, June 2023.

[94] NeXolve, "Aerospace Products: Solar Sails." Electronically, 2024.

[95] NeXolve, "CP1™Polymide." Electronically, Oct. 2021.

[96] L. Nguyen, K. Medina, Z. McConnel, and M. S. Lake, "Solar Cruiser TRAC boom development," in *AIAA SCITECH 2023 Forum*, American Institute of Aeronautics and Astronautics, Jan. 2023.

[97] F. P. Beer, E. R. Johnston, Jr., J. T. DeWolf, and D. F. Mazurek, *Mechanics of Materials*. New York, NY: McGraw-Hill, sixth ed., 2012.

[98] L. Johnson, "Personal Correspondence: RE: NEA Scout mass breakdown." Personal Corresponence, Aug. 2023.

[99] K. Kobayashi, L. Johnson, H. Thomas, S. McIntosh, D. McKenzie, J. Newmark, A. Heaton, J. Carr, M. Baysinger, Q. Bean, L. Fabisinski, P. Capizzo, K. Clements, S. Sutherlin, J. Garcia, K. Medina, and D. Turse, "The high inclination solar mission," 2020.

[100] H. Schaub and J. L. Junkins, *Analytical Mechanics of Space Systems*. AIAA Education Series, American Institute of Aeronautics and Astronautics, Inc., 3rd ed., 2014.

[101] D. A. Vallado, *Fundamentals of Astrodynamics and Applications*. Microcosm, 2007.

[102] B. Dachwald, A. Ohndorf, and B. Wie, "Solar Sail Trajectory Optimization for the Solar Polar Imager (SPI) Mission," in *AIAA/AAS Astrodynamics Specialist Conference and Exhibit*, American Institute of Aeronautics and Astronautics, jun 2006.

[103] D. Thomas, K. Kobayashi, B. Mike, Q. Bean, P. Capizzo, K. Clements, L. Fabisinski, J. Garcia, and S. Steve, "Solar Polar Imager Concept," in *ASCEND 2020*, American Institute of Aeronautics and Astronautics, nov 2020.

[104] M. Macdonald, G. W. Hughes, C. R. McInnes, A. Lyngvi, P. Falkner, and A. Atzei, "Solar Polar Orbiter: A Solar Sail Technology Reference Study," *Journal of Spacecraft and Rockets*, vol. 43, pp. 960–972, sep 2006.

[105] Aerojet Rocketdyne, "In-Space Propulsion Data Sheets." Electronically, Apr. 2020.

[106] Aerojet Rocketdyne, "NEXT-C: NASA Evolutionary Xenon Thruster-Commercial." Electronically, Jan. 2022.

[107] E. Bourguignon and S. Fraselle, "PPU MK3 for 5 KW Hall Effect Thrusters 11th European Space Power Conference," *E3S Web of Conferences*, vol. 16, p. 15001, 2017.

[108] R. W. Ebert, F. Allegrini, F. Bagenal, C. R. Beebe, M. A. Dayeh, M. I. Desai, D. E. George, J. Hanley, P. Mokashi, N. Murphy, P. W. Valek, A. A. Wolf, and C. wan L. Yen, "JUpiter magnetospheric boundary ExploreR (JUMPER)," in *2018 IEEE Aerospace Conference*, IEEE, mar 2018.

[109] E. Sunada, P. Bhandari, B. Carroll, T. Hendricks, B. Furst, J. Kempenaar, G. Birur, H. Nagai, T. Daimaru, K. Sakamoto, *et al.*, "A two-phase mechanically pumped fluid loop for thermal control of deep space science missions," in *Proceedings of the 46th International Conference on Environmental Systems, 10-14 July 2016, Vienna, Austria*, 46th International Conference on Environmental Systems, 2016.

[110] J. A. Englander, "RE: Finalizing SmallSat-class MEL." Email, June 2023.

[111] J. R. Wertz, D. F. Everett, and J. J. Puschell, *Space Mission Engineering: The New SMAD*. Microcosm Press, 2011.

[112] "Standard: Mass properties control for space systems (ANSI/AIAA s-120a-2015)," in *Standard: Mass Properties Control for Space Systems (ANSI/AIAA S-120A-2015)*, American Institute of Aeronautics and Astronautics, Inc., jan 2015.

[113] T. Engelhardt, R. Jedicke, P. Vereš, A. Fitzsimmons, L. Denneau, E. Beshore, and B. Meinke, "An Observational Upper Limit on the Interstellar Number Density of Asteroids and Comets," *The Astronomical Journal*, vol. 153, p. 133, feb 2017.

[114] D. J. Hoover, D. Z. Seligman, and M. J. Payne, "The Population of Interstellar Objects Detectable with the LSST and Accessible for In Situ Rendezvous with Various Mission Designs," *The Planetary Science Journal*, vol. 3, p. 71, Mar. 2022.

[115] D. Marčeta, "Synthetic population of interstellar objects in the Solar System," *Astronomy and Computing*, vol. 42, p. 100690, Jan. 2023.

[116] A. M. Hein, T. M. Eubanks, M. Lingam, A. Hibberd, D. Fries, J. Schneider, P. Kervella, R. Kennedy, N. Perakis, and B. Dachwald, "Interstellar Now! Missions to Explore Nearby Interstellar Objects," *Advances in Space Research*, vol. 69, pp. 402–414, jan 2022.

[117] D. Miller, F. Duvigneaud, W. Menken, D. Landau, and R. Linares, "High-performance solar sails for interstellar object rendezvous," *Acta Astronautica*, vol. 200, pp. 242–252, nov 2022.

[118] J. C. Castillo-Rogez, K. Meech, S.-J. Chung, and D. Landau, "Approach to exploring interstellar objects and long-period comets," in *SPACEFLIGHT MECHANICS 2019*, vol. 168 of *Advances in the Astronautical Sciences*, pp. 2115–2128, American Astronautical Society, Univelt, Inc., Jan. 2019.

[119] G. P. Vivan and J. Hudson, "Exploring Long-Period Comets from Multiple Staging Orbits," *The Journal of the Astronautical Sciences*, vol. 68, pp. 608–641, jul 2021.

[120] B. P. Donitz, J. C. Castillo-Rogez, and S. E. Matousek, "Rapid response to long period comets and interstellar objects using SmallSat architecture," in *2021 IEEE Aerospace Conference (50100)*, IEEE, mar 2021.

[121] B. P. S. Donitz, D. Mages, D. Landau, J. V. Maydan, J. Castillo-Rogez, and D. Farnocchia, "Interstellar Object Encounter Trade Space Exploration," in *2022 IEEE Aerospace Conference (AERO)*, IEEE, mar 2022.

[122] K. Moore, S. Courville, S. Ferguson, A. Schoenfeld, K. Llera, R. Agrawal, D. Brack, P. Buhler, K. Connour, E. Czaplinski, M. DeLuca, A. Deutsch, N. Hammond, D. Kuettel, A. Marusiak, S. Nerozzi, J. Stuart, J. Tarnas, A. Thelen, J. Castillo-Rogez, W. Smythe, D. Landau, K. Mitchell, and C. Budney, "Bridge to the stars: A mission concept to an interstellar object," *Planetary and Space Science*, vol. 197, p. 105137, mar 2021.

[123] C. Snodgrass and G. H. Jones, "The european space agency's comet interceptor lies in wait," *Nature Communications*, vol. 10, nov 2019.

[124] A. Boca, R. Warwick, B. White, and R. Ewell, "A data-driven evaluation of the viability of solar arrays at saturn," *IEEE Journal of Photovoltaics*, vol. 7, pp. 1159–1164, jul 2017.

[125] J. J. Bontempo, A. N. Brigeman, H. B. Fain, M. C. Gonzalez, L. R. Pinero, A. G. Birchenough, M. V. Aulisio, J. Fisher, and B. Ferraiuolo, "The NEXT-C Power Processing Unit: Lessons Learned from the Design, Build, and Test of the NEXT-C PPU for APL's DART Mission," in *AIAA Propulsion and Energy 2020 Forum*, p. 3641, 2020.

[126] R. H. Gooding, "A procedure for the solution of Lambert's orbital boundary-value problem," *Celestial Mechanics and Dynamical Astronomy*, vol. 48, no. 2, pp. 145–165, 1990.

[127] P. Tsou, D. E. Brownlee, S. A. Sandford, F. Hörz, and M. E. Zolensky, "Wild 2 and interstellar sample collection and Earth return," *Journal of Geophysical Research: Planets*, vol. 108, Oct. 2003.

[128] A. Stankov, F. Ratti, N. Rando, M. Kueppers, C. Corral Van Damme, A. Wielders, K. Wirth, V. Agnolon, and J. Asquier, "The ESA Comet Interceptor mission and its payload complement," in *Proceedings of the 16th Europlanet Science Congress 2022, 18-23 September 2022, Palacio de Congresos de Granada, Spain*, Copernicus GmbH, Sept. 2022.

[129] Mihkel Pajusalu, Joosep Kivastik, Iaroslav Iakubivkyi, and Andris Slavinskis, "Developing autonomous image capturing systems for maximum science yield for high

fly-by velocity small solar system body exploration," in *71st International Astronautical Congress (IAC) - The CyberSpace Edition, 12-14 October 2020*, International Astronautical Federation, International Astronautical Federation, Oct. 2020.

[130] N. Haslebacher, S.-B. Gerig, N. Thomas, R. Marschall, V. Zakharov, and C. Tubiana, "A numerical model of dust particle impacts during a cometary encounter with application to ESA's Comet Interceptor mission," *Acta Astronautica*, vol. 195, pp. 243–250, June 2022.

[131] P. Machuca, N. Ozaki, J. P. Sánchez, and L. Felicetti, "Dust impact and attitude analysis for JAXA's probe on the Comet Interceptor mission," *Advances in Space Research*, vol. 70, pp. 1189–1208, Sept. 2022.

[132] R. Anderson and R. C. Anderson, *The Sailing-ship: Six Thousand Years of History*. New York, NY: Robert M. McBride & Company, 1926.

[133] J. Armstrong and D. M. Williams, *The Impact of Technological Change: The Early Steamship in Britain*. Liverpool University Press, Oct. 2017.

[134] D. Ford, "B-36: Bomber at the Crossroads," *Air & Space Magazine*, Apr. 1996.

[135] M.-K. Tran, A. Bhatti, R. Vrolyk, D. Wong, S. Panchal, M. Fowler, and R. Fraser, "A Review of Range Extenders in Battery Electric Vehicles: Current Progress and Future Perspectives," *World Electric Vehicle Journal*, vol. 12, p. 54, Apr. 2021.

[136] J. Walters, H. Husted, and K. Rajashekara, "Comparative Study of Hybrid Powertrain Strategies," *SAE Transactions*, vol. 110, no. 3, 2001.

[137] E. Antonucci, M. Romoli, V. Andretta, S. Fineschi, P. Heinzel, J. D. Moses, G. Naletto, G. Nicolini, D. Spadaro, L. Teriaca, A. Berlicki, G. Capobianco, G. Crescenzio, V. D. Deppo, M. Focardi, F. Frassetto, K. Heerlein, F. Landini, E. Magli, A. M. Malvezzi, G. Massone, R. Melich, P. Nicolosi, G. Noci, M. Pancrazzi, M. G. Pelizzo, L. Poletto, C. Sasso, U. Schühle, S. K. Solanki, L. Strachan, R. Susino, G. Tondello, M. Uslenghi, J. Woch, L. Abbo, A. Bemporad, M. Casti, S. Dolei, C. Grimani, M. Messerotti, M. Ricci, T. Straus, D. Telloni, P. Zuppella, F. Auchère, R. Bruno, A. Ciaravella, A. J. Corso, M. A. Copano, R. A. Cuadrado, R. D'Amicis, R. Enge, A. Gravina, S. Jejčič, P. Lamy, A. Lanzafame, T. Meierdierks, I. Papagiannaki, H. Peter, G. F. Rico, M. G. Sertsu, J. Staub, K. Tsinganos, M. Velli, R. Ventura, E. Verroi, J.-C. Vial, S. Vives, A. Volpicelli, S. Werner, A. Zerr, B. Negri, M. Castronuovo, A. Gabrielli, R. Bertacin, R. Carpentiero, S. Natalucci, F. Marliani, M. Cesa, P. Laget, D. Morea, S. Pieraccini, P. Radaelli, P. Sandri, P. Sarra, S. Cesare, F. D. Forno, E. Massa, M. Montabone, S. Mottini, D. Quattropani, T. Schillaci, R. Boccardo, R. Brando, A. Pandi, C. Baietto, R. Bertone, A. Alvarez-Herrero, P. G. Parejo, M. Cebollero, M. Amoruso, and V. Centonze, "Metis: the Solar Orbiter visible light and ultraviolet coronal imager," *Astronomy & Astrophysics*, vol. 642, p. A10, sep 2020.